Microscopic simulation of the mechanically modulated electrical conductivity of piezoelectric semiconductors

Zur Erlangung des akademischen Grades Doktor-Ingenieur (Dr.-Ing.)
genehmigte Dissertation von Ziqi Zhou aus Xianyang, China
Tag der Einreichung: July 03. 2020, Tag der Prüfung: September 18. 2020

1. Gutachten: Prof. Dr. Bai-Xiang Xu
2. Gutachten: Dr. rer. nat. Erion Gjonaj
Darmstadt

TECHNISCHE
UNIVERSITÄT
DARMSTADT

MECHANICS of
FUNCTIONAL
MATERIALS

Microscopic simulation of the mechanically modulated electrical conductivity of piezoelectric semiconductors

Doctoral thesis by Ziqi Zhou

1. Review: Prof. Dr. Bai-Xiang Xu
2. Review: Dr. rer. nat. Erion Gjonaj

Date of submission: July 03. 2020
Date of thesis defense: September 18. 2020

Darmstadt

Erklärungen laut Promotionsordnung

§8 Abs. 1 lit. c PromO

Ich versichere hiermit, dass die elektronische Version meiner Dissertation mit der schriftlichen Version übereinstimmt.

§8 Abs. 1 lit. d PromO

Ich versichere hiermit, dass zu einem vorherigen Zeitpunkt noch keine Promotion versucht wurde. In diesem Fall sind nähere Angaben über Zeitpunkt, Hochschule, Dissertationsthema und Ergebnis dieses Versuchs mitzuteilen.

§9 Abs. 1 PromO

Ich versichere hiermit, dass die vorliegende Dissertation selbstständig und nur unter Verwendung der angegebenen Quellen verfasst wurde.

§9 Abs. 2 PromO

Die Arbeit hat bisher noch nicht zu Prüfungszwecken gedient.

Darmstadt, July 03. 2020

Ziqi Zhou

Acknowledgment

First of all, I would like to express my sincere gratitude to my advisor, Prof. Dr. Bai-Xiang Xu, for her trust and the admission to join the MFM family. In my three years research period, she devoted many efforts in giving me suggestions in my Ph.D. study and related research, provided my great freedom in the research field and enlight me with new research directions. I have benefited and learned a lot from her, especially from her immense knowledge and strict logic. Her guidance helped me in all the time of research and writing of this thesis.

Besides my advisor, I would also like to thank Prof. Andreas Klein, who gave me many times kind and constructive discussions. His insightful knowledge regarding the physics of semiconductors impressed me. With his help, constructing the model became much smoother. My sincere thanks also go to Dr. Till Fröming for his insightful comments and encouragement during the paper writing. I wish to acknowledge Dr. Erion Gjonaj for the careful reading and commenting on the paper we published as well as this dissertation. I would also thank Prof. Dr. Karsten Albe for the kind suggestions during the discussions and agreement to join the defence commission board.

I am grateful to Dr. Min Yi, who guides me into the simulation field and held countless helpful discussions. Without him, I would not be in this field. I would like to thank Yangbai, who gave me many supports with the software MOOSE. I would also like to thank Dr. Yangbin Ma, Dr. Peter Stein, Dr. Zhen Liu, Dr. Xiandong Zhou, Dr. Ying Zhao, Yao Liu, Yangyiwei Yang, Binbin Lin, Peter Kyle, Kyle Taylor and the other colleagues for their professional discussions and help from all the aspects. I appreciate Mrs. Maren Arnold's help for the assistant in writing and handling documentation whenever I had a german language problem.

Finally, I would like to express my very great appreciation to my parents, for their care and supports in my life. I wish to give my special thanks to my girlfriend Liwei Chen, who sacrificed many opportunities back in China and accompanying me writing the dissertation here. Being with her was the happiest time in my life.

Parameters

κ_0	Initial configuration
κ_t	Current configuration
t	Time (s)
X_i	Coordinate in initial configuration (m)
x_i	Coordinate in current configuration (m)
δ_{ij}	Kronekcer delta
F_{ij}	Deformation gradient
S_{ij}	Infinitesimal strain
$\mathscr{B}$	Study target body
$\mathscr{H}$	The arbitrary volume of a study target body
C_{ijkl}	Stiffness tensor (Nm^{-2})
n_i	surface normal vector
t_i	surface traction force vector (Nm^{-2})
dL	Line element in initial configuration (m)
dl	Line element in current configuration (m)
$\mathscr{E}_{ij}$	Green strain tensor
r	Distance between two electric charges (m)
$\mathscr{E}_i$	Electric field (Vm^{-1})
q	Unit electric charge (C)
ϵ_0	Vacuum permittivity (Fm^{-1})
ϵ_r	Relative permittivity (1)
ϵ_s	Permittivity of the material, multiplication of ϵ_0 and ϵ_r (Fm^{-1})
ϕ	Electric potential (V)
D_i	Electric displacement (Cm^{-2})
ρ	Charge density (Cm^{-3})
f_i	Volume force (Nm^{-3})
v_i	velocity (ms^{-1})
σ_{ij}	Cauchy stress (Nm^{-2})
σ_{ij}^m	Maxwell stress (Nm^{-2})

T	Temperature (K)
$\delta_{(\cdot)}(\cdot)$	Variational symbol
N_C	Effective density of states in the conduction band (m^{-3})
N_V	Effective density of states in the valence band (m^{-3})
$\mathscr{E}_F$	Fermi level (eV)
$\mathscr{E}_C$	Conduction band edge (eV)
$\mathscr{E}_V$	Valence band edge (eV)
$F_{\frac{1}{2}}$	Fermi integral
D	Diffusion coefficient $(m^2 s^{-1})$
P_s	Spontaneous polarization (Cm^{-2})
N^I	Shape function
R_k^I	Residual vector
K_{kl}^{IJ}	Stiffness matrix
P_i	Total polarization Cm^{-2}
N	Total number of particles
K_{ij}	Coefficients s^{-1}
V_0	Unit cell volume m^3
U	Net recombination/generation rate, U=R-G $(\mathrm{m}^{-3} - \mathrm{s}^{-1})$
n_i	Intrinsic carrier concentration (m^{-3})
g_A	Ground degeneracy level of acceptors (1)
g_D	Ground degeneracy level of donors (1)
$\boldsymbol{k}$	wave vector (m^{-1})
J_n	electron flux (A/m^2)
μ_n	electron drift mobility $(m^2/V \cdot s)$
J_p	hole flux (A/m^2)
μ_p	hole drift mobility $(m^2/V \cdot s)$
σ_0	applied external stress (Pa)
V_a	applied voltage (V)
$\mathscr{E}_{f0}$	the Fermi level which calculated from charge neutrality rule (eV)
$\mathscr{E}_C$	bottom of the conduction band (eV)
$\mathscr{E}_V$	top of the valance band (eV)
$\mathscr{E}_{Fn}$	quasi-Fermi energy for electrons (eV)
$\mathscr{E}_{Fp}$	quasi-Fermi energy for holes (eV)
Q_I	trap charge density $(1/m^3)$
Φ_B	barrier height at grain boundary (eV)
Q_P	polarization charge at interface densities $(1/m^3)$
e	piezoelectric constant (C/m^2)

Y	Young's modulus (Pa)
$\tilde{Q}_I$	interface polarization charge plus trap charge densities $(1/m^3)$
$\tilde{N}_0$	volume polarization charge plus ionized donor densities $(1/m^3)$
ρ_p	volume polarization charge densities $(1/m^3)$
Σ	the degree of fit for coincidence lattice site (1)
x_l	left boundary of the assumed space charge area in phenomenological model
x_r	right boundary of the assumed space charge area in phenomenological model
V_c	critical voltage
ξ_I^n	fictitious Fermi level describing neutral interface (eV)
$\mathscr{D}(\mathscr{E})$	defect density of states in the GB $(1/m^2$for 0 width GB or$1/m^3$for GB with volume$)$
k	Boltzmann constant (eV/K)
$\xi_I(V)$	quasi-Fermi level (eV)
N_t	effective trap density of states in GB $(1/m^2$for 0 width GB or$1/m^3$for GB with volume$)$
$\mathscr{E}_I$	centre of the DOS distribution (eV)
$\Delta\mathscr{E}$	span of the DOS distribution (eV)
n_i	intrinsic carrier concentration $(1/m^3)$
$\mathscr{E}_i$	intrinsic Fermi level (eV)
$\dot{\mathrm{n}}$	time derivative of electrons $(1/m^3 s)$
$\dot{\mathrm{p}}$	time derivative of holes $(1/m^3 s)$

Abbreviations

FE	finite element
FEM	finite element method
FEAP	Finite Element Analysis Program
MOOSE	Multiphysics Object-Oriented Simulation Environment
TEM	transmission electron microscope
GB	grain boundary
PM	phenomenological model
MPM	modified phenomenological model
DOS	density of states
DOF	degrees of freedom
MSE	mean square error
MAE	mean absolute error

Abstract

Piezoelectric semiconductors have drawn significant attention in recent decades due to their unique physical properties. The coupling of piezoelectric and semiconductive effects allow possibilities to tune the electric potential in the material. Evidently, by mechanical loading, the charge flow of the circuit is adjustable. This effect is named as piezotronics effect and brings possibilities in producing new devices, such as light-emitting diode and new mechanically tuned field-effect transistors. Among all the piezotronic materials, ZnO is regarded as the most prominent one, due to its highest piezoelectric coefficient, high abundance of Zn, and a mature production of nanostructures.

However, the understanding of grain boundary potential barriers of ZnO is insufficient because the physical mechanism for barrier development and its modification by external influence factors are complex. It has been shown that the barrier height can be significantly modulated by mechanically induced piezoelectric charge. Consequently, this makes ZnO-ZnO interfaces advanced piezotronic systems because the conductivity can be controlled by mechanical stress. Using this effect in applications, however, needs the possibility of tailoring the interfaces and an accurate physical description of the piezoelectric impact. For this purpose, reliable models are strongly desired. In order to understand the physical principles of the coupling effect specifically at the double Schottky barrier and making better use of it, a classical phenomenological model has been improved, and a finite element (FE) model has been developed.

An extended phenomenological model is proposed to rationalize the potential barriers of the varistor like boundaries for piezoelectric semiconductors. Comparing to other phenomenological models, the model developed in this work self-consistently takes the internal electric field effect near the grain boundary into account. The effect is originated from the double Schottky barrier at a grain boundary, which gives rise to a strong internal electric field in the depletion layer. Due to the inverse piezoelectric effect, this electric field leads to mechanical strain and, consequently, piezoelectric charge at a grain boundary, and more importantly, an additional space charge associated with the polarization inhomogeneity. The piezoelectric charges, in return, impacts the barrier height. Results show that the piezoelectric charge induced by the internal field tends to adjust the grain boundary charge and lowers the barrier height. Moreover, the barrier height becomes less sensitive to mechanical stress and applied voltage if the influence of the internal field

is taken into account. The extended model with the inverse piezoelectric effect of the internal field allows elucidating their piezotronic response further. The work improves the barrier height theory of piezoelectric ceramics and enriches the study of the piezoelectrics and other junction devices.

Furthermore, an electromechanically coupled finite element model is developed in this work. Due to the full coupling effect, the model requires few prior assumptions on the charge distribution, enables multi-dimensional simulations of multigrain, and allows access to quantities such as the charge, energy, and electric field distributions. Moreover, the FE model inherently includes inverse piezoelectric and anisotropy effect, which are shown to have a significant impact on barrier height. Additionally, it is illustrated that this model can be used for advanced 3D microstructure simulations taking the complexity of the interface properties into account.

Fully coupled electromechanical finite element simulations have also been carried out to study the varistor behaviour under bias voltage and mechanical loading. Thereby the quasi-Fermi energies are taken into account, bringing more physical foundations into the model. Comparing to the phenomenological model, the FE model demonstrates that the breakdown is highly related to the gradient of the band structure and the strong shrink of the barrier height. Hence, the finite element model conveys a more insightful understanding of how the piezoelectric varistor works.

Both the modified phenomenological and finite element models proposed in this work demonstrate that considering the internal electric field reduces the barrier height and increases the current. It implies that if the internal electric field induced GB polarization charge and the polarization charge density in the screening layer is regarded, the determined grain boundary trap charge densities are expected to be higher than those obtained by the previous models.

With the proposed models, systematic parameter studies have been carried out in the end to study the influence of mechanical loading on the grain boundary barrier height and varistor features. The obtained data were used to train a Neural Networks model to make the parameter-property relation accessible to a broad community. The knowledge achieved in the thesis is not limited to the grain boundaries of ZnO but has practical consequences on the study of general junction devices.

Contents

1 Introduction

Piezoelectric semiconductive materials have recently drawn considerable research attention. Due to the piezoelectric effect, the charge status at the interface of the piezotronics can be tuned. Thus the band structures at the interfaces have the possibility to be modified, and the charge flux can be controlled. The devices which use this mechanism is termed as piezotronics. The research group of Zhong Lin Wang[1] firstly defined the term piezotronics in 2007. From then on new application concepts prospered in the research field such as piezotronics nanogenerators, piezoelectric FETs and strain sensors.[2, 3, 4, 5, 6]

The wurtzite structure materials possess piezoelectric property since they have a non-central symmetry. Many III-V binary compounds are of this type of structures and, at the same time, have semiconductivity, which makes them naturally the candidates for piezotronic materials. These materials include, for example, ZnO, GaN, and InN[7].

Of all the piezotronic materials, most of the research concentrates on ZnO due to its high piezoelectric coefficient, high electron mobility, and easy fabrication of the nanostructures. The configurations of the ZnO nanostructures are in a broad range such as ZnO film, bridge, nanowire, nanorod, and nanobelt.[8] The study of ZnO can be date back almost 90 years ago. In 1935, Bunn initiated the ZnO study by measuring the lattice parameter [9]. In 1966 the vibrational properties were studied by Damen et al. with Raman scattering technique [10]. In 1970, a ZnO thin film was firstly produced by Ohnishi et al. with chemical vapour deposition (CVD) [11].

The metal-semiconductor contact (single Schottky contact) aroused the research interest due to the critical role it plays in the devices such as transparent thin-film transistors, lasers, and high electron mobility transistors.[12] In 1965, the pioneering work of the single Schottky contact was conducted by Mead. The band bending, charge transfer, and the formation of the barrier are demonstrated in his study [13]. The research focus of the semiconductor-metal contact has been transferred from the GaN to ZnO in the last three decades since the abundance of Zn is much higher than Ga, and the nanostructure of Zn is easy to produce. Besides that, the ZnO crystal growth, doping, and device design have been considerably developed in the past decades. Large research intention on ZnO was however, initiated in 2006 by the group of Zhong-Lin Wang. By using the mechanism of metal-semiconductor contact, they proposed the concept of two devices: nanogenerator[14] and piezoelectric field effect transistor[15], which opened up new ways of

producing energy gathering devices and force/pressure sensors.

The energy barrier does not only exist at the single but also the double Schottky contact (semiconductor-semiconductor contact). It is expected that understanding the energy barrier at the grain boundary is essential in the various applications of multigrain ZnO crystal. In 1976, J. Wong and F.P. Bundy studied the influence of pressure on the varistor behaviour of the multigrain ZnO[16]. In their research, it is demonstrated that the conductivity can be significantly increased when increasing the external loading. Since ZnO is a piezoelectric material, this naturally aroused the question: how does the grain boundary play a role in the I-V curve. Emtage[17] declared that the electrons trapped inside the intergranular material create a barrier height, which hinders the electron transportation. He further claimed that the breakdown is caused by the completion of the trap states, and the piezoelectric charge in the ZnO grain can alter the barrier height. Due to the existence and the capability of modifying the barrier height at grain boundaries, the bulk ZnO material has the potential to be used in the pressure sensor devices [18, 19, 20, 21]. It is reported that the gauge factor can reach 800 which is much higher than conventional sensors.[22, 23].

The double Schottky barrier devices possess superior physical performance since the energy barrier at the grain boundary can be almost entirely eliminated at ZnO-ZnO interfaces [24, 25] (86% reported so far), which is far exceeding regular Schottky barriers in modifiability (usually decreased by only a few meV). [26, 27, 28]. This capability of large barrier height modification allows a much higher ON/OFF ratio than the single Schottky contact device in the field-effect transistor applications [29].

In a polycrystal varistor, the energy barriers are connected in series and parallel. Thus, such materials demand higher operating voltages. The bicrystal structure is a special case of the double Schottky barrier system. The solo energy barrier at the grain boundary can reach the operating voltage down to 0.1 V while achieving the ON/OFF of 27 [25]. Hence, as a basic element of the polycrystalline piezotronic devices and the high potential new type of applications, understanding the working mechanism of bicrystal is necessary.

Due to the defects or intentionally doping with elements such as Bi or Pr in the GBs [30, 31, 32, 33], the defect energy states can capture electrons. Because of the electro-neutrality condition, an electron-depleted space charge layer evolves, thus generating a potential barrier. In order to describe the influence of the trap states on the barrier height, Blatter and Greuter [34, 35, 30] developed a self-consistent model system for calculating the barrier height depending on the externally applied voltage. In this model, the calculations for the barrier height and the GB trap charge are mutually coupled to one another.

Specifically, when the barrier height is lowered, the trap charge density grows, as more defect states fall below the Fermi-Level. However, the extra charges at the GB lead to the inhibition of further barrier height reduction until the GB trap states are fully filled, which leads to a fast breakdown of the potential barrier. If the applied voltage is further increased, then hot electrons

and holes are generated. [36] These holes then diffuse back to the GB and compensate for the negative charges at the GB, thus accelerating the breakdown.

The self-consistent system and hot electron theory result in an accurate description of varistor behavior. Due to the thermal expansion of the constituents and the thermal expansion mismatch between phases, Verghese and Clarke [37] introduced stress loading to the barrier height calculations, which provides extra piezoelectric charges at the GB. Baraki et al. [20] showed a phenomenological model that takes both self-consistent calculation and external loading into consideration.

Due to the large barrier height and narrowness of the depletion region, a high internal electric field generates in this region. This field induces its mechanical stress due to the inverse piezoelectric effect, consequently, generates additional polarization and alter charge distributions. This inverse electric field thus has an impact on barrier height, which hasn't been considered in the classical phenomenological works.

Besides the advantages of the phenomenological model, such as saving computational resources, this model relies on several approximations. Consequently, the results from the phenomenological model are distorted in certain aspects comparing to realistic situations. Since it is too complex to have an analytical solution without using approximations, it is necessary to consider a numerical solution. Of all the possible options, the FE method has significant advantages, for instance, extending the simulation into 3D to account for real microstructures becomes feasible.

The main objective of this thesis is to provide a comprehensive phenomenological and finite element (FE) model. For the phenomenological model, we discussed the internal electric field in the depletion region, which changes both the surface charge at the grain boundary and the space charge in the depletion region. Consequently, its impact on the grain boundary barrier height cannot be ignored. Therefore based on the research done by Baraki [20], in this work, the inverse piezoelectric effect was included self-consistently in the phenomenological model. The proposed FE model covers drift and diffusion of the charge carriers, generation, recombination process, and mechanics. In this way, the advantages of the FE method can be carried out. For example, in 3D calculations, the piezoelectric anisotropy is perfectly considered; the transportation details on the nanoscale can be illustrated, and a more accurate varistor I-V behaviour can be produced. Hence the FE model plays a significant role in more comprehensively understanding the mechanisms of transport behaviour.

The structure of the thesis is outlined in the following.

In chapter 2, the physical nature of why ZnO is typically used as an n-type semiconductor is demonstrated. It then followed the introduction of the possible ZnO crystal structures.

Chapter 3 introduces the theories which are needed to build the model. These theories include electrostatics, mechanics, piezoelectric, semiconductor physics, and the structure of grain boundaries.

Chapter 4 introduces the method to calculate the band energy profile and barrier height with the phenomenological equations. Comparing to other classical phenomenological models, in this chapter, the importance of the internal electric field in the depletion region is demonstrated. We show how to incorporate this field in the model.

Chapter 5 build the FE framework for stress-barrier height relations. It is compared with the phenomenological model mentioned in chapter 4 and showed its advantages in random grain orientations and multigrain calculations.

Chapter 6 gives the varistor FE framework, which includes the stress and bias voltage influence on the barrier height and flux. It firstly demonstrated the nanoscale details of the band structure under external bias voltage, thereby increases the understanding of the physical phenomenons in the varistor device.

Chapter 7 uses the neural networks studying the FE results. In this way, one can avoid the time-consuming FE calculation, thus achieving accurate barrier height and flux results more conveniently.

2 Basics of ZnO

ZnO has a wide direct bandgap (E_g) of around 3.2 eV at 300 K. At such a bandgap, the recombination of electrons and holes can produce ultraviolet radiation. GaN, another leading semiconductor which has a similar bandgap of 3.4 eV at 300 K, can also be used to generate ultraviolet light. However, it is not easy to produce high-quality large bulk single crystals comparing to ZnO. The synthesis methods of ZnO are various, including PVD, CVD, hydrothermal, and pressurized melt growth [38].

Except for growing large crystal bulk, ZnO can also be grown as the morphologies of nanorods and nanowire arrays. Vayssieres reported that by implementing aqueous solutions, a large scale, low-cost nanorods, and nanowires could be fabricated. Besides, by using this method, the scale of the product can be varied from nano to micro crystallites [39]. Another popular ZnO nanowire synthesis method is PVD. Kong et al. [40] reported that they achieved a diameter of around 60 nm and the length up to a few micrometers. Also, a more intense UV light emission was observed than in bulk ZnO due to fewer defects with this method.

Epitaxial ZnO thin films are also heavily studied [41, 42, 43, 44, 45]. Its applications cover many fields, including varistors, transparent conductive electrodes for solar cells, piezoelectric devices, and gas sensors.

Extensive studies have been carried out to fabricate p-type ZnO, which can be formed on an n-type ZnO to produce ZnO diode. It is reported by Aoki et al. [46] that the excimer-laser pulse technique can be implemented to dope p-type ZnO. Ryu et al. doped arsenic (As) into ZnO with pulsed laser ablation to create p-type ZnO [41, 42]. Notwithstanding the above, the reproducibility of p-type ZnO remains controversial [47]. Hence, producing the high conductive p-type ZnO is a major issue for its implementations.

ZnO possesses other outstanding physical properties, which include pyroelectricity [48, 38, 49, 50], and magnetic properties if transition metals are doped [51]. Consequently, high electron mobility, thermal conductivity, direct wide bandgap and large exciton binding energy, plenty of electronic and photonic devices are innovated, such as transparent thin-film transistors, photodetectors, light-emitting diodes, and optically pumped lasers.

2.1 N-type nature of ZnO

To illustrate why ZnO is difficult to form into a p-type semiconductor, the self-compensation mechanism needs to be introduced. The semiconductor crystals possess intrinsic defects such as vacancies, interstitial defects, or more complicated AX or DX centers. The formation of different kinds of ionized defects is dependent on the defect creation enthalpies. For example, when a type of acceptor is introduced into the semiconductor, and the Fermi energy is above the acceptor energy, the electrons fill the acceptor states and, at the same time, releases energy. This released energy can contribute to generating the intrinsic defects (contribute to the defect creation enthalpies), for instance, oxygen vacancies, which happens to be mostly donors. Thus, introducing the acceptor type dopant turns out to trigger the generation of the donor type intrinsic defect, which in the end makes the semiconductor n-type.

C.H. Park et al. [52] studied the p-type doping difficulties in ZnO. They considered the dopants from group-I elements Li, Na, and K and group-V elements N, P, and As, which are all served as donors. Once these dopants are introduced, the atomic structure will have relaxation by cutting and reconnecting the bonds, which is illustrated in Fig. 2.1.

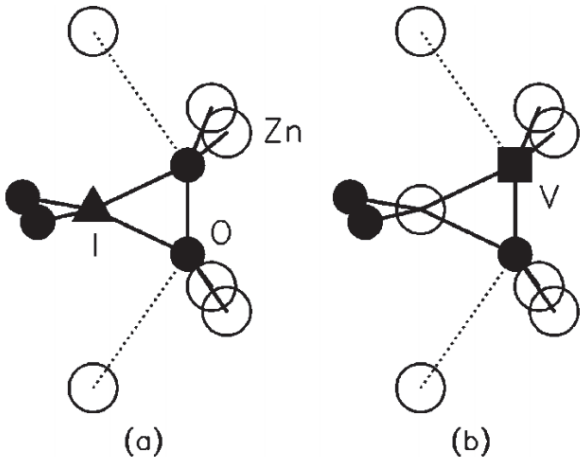

Figure 2.1: Lattice relaxation of ZnO with p-type doping by introducing the group-I (a) or group-V elements (b). [52]

In Fig. 2.1, the solid triangle, and square in (a) and (b) represent the impurities from group-I and group-V, respectively. For the group-I impurities in (a), the relaxation causes the formation of the bonding between oxygen atoms, leaving the double broken bonds for zinc atoms, and thus providing donor type defects. Group-V impurities in (b) have a similar mechanism. Instead of building the bonds between oxygen atoms, the relaxation leads to the bonding formation between the impurities and the oxygen atom. Consequently, the double broken bonds are formed.

Hence, it is not easy to form a p-type ZnO since the self-compensation convert acceptors into deep donors. Nevertheless, there are chances for the p-type doping, such as using N.

2.2 Structures of ZnO

Same as the II-VI binary compound semiconductors, the most commonly seen ZnO has hexagonal wurtzite crystal structure since it is the thermodynamically stable phase at ambient conditions. The wurtzite crystal has no inversion symmetry, as demonstrated in Fig. 2.2, in which Zn is shown in yellow and O in grey. The zinc and oxygen each forms a close-packed hexagonal-close-packed (hcp) sublattice and interpenetrating with each other. Due to the sp^3 covalent bonding, every zinc atom is surrounded by four oxygen tetrahedron, and vice versa, as also shown in Fig. 2.3c. The lattice parameter has the relation of $c/a = \sqrt{8/3} = 1.633$. The crystal is symmetric about the c-axis, which is normal to the x-y isotropy plane; hence it has 6mm symmetry.

Apart from the wurtzite structure, as schematically illustrated in Fig. 2.3, ZnO could have two other crystal structures: zinc blende (ZnS) and rocksalt (NaCl). Both the zinc blende and wurtzite have one kind of atom connected by another four kinds of atoms. However, the zinc blende has a cubic structure while the wurtzite has a hexagonal structure. The difference can be seen from the top views in Fig. 2.3. Unlike in the wurtzite structure, the zinc and oxygen do not overlap on top of each other in zinc blende. In other thermodynamical conditions, these two structures can be fabricated; for example, the external hydrostatic pressure facilitates the formation of rocksalt ZnO structure.

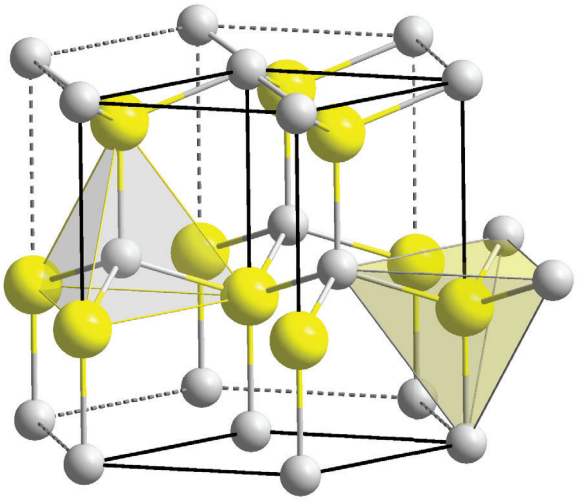

Figure 2.2: Stickball model for hexagonal structure ZnO, in which Zn is shown in yellow and O in gray balls. The zinc and oxygen each forms a close-packed hexagonal-close-packed (hcp) sublattice and interpenetrates with each other [53].

ZnO is often used as a varistor material, which exhibits non-linear current-voltage behavior owing to the potential barriers existing at the grain boundaries. [55, 56, 57] Due to the continuing

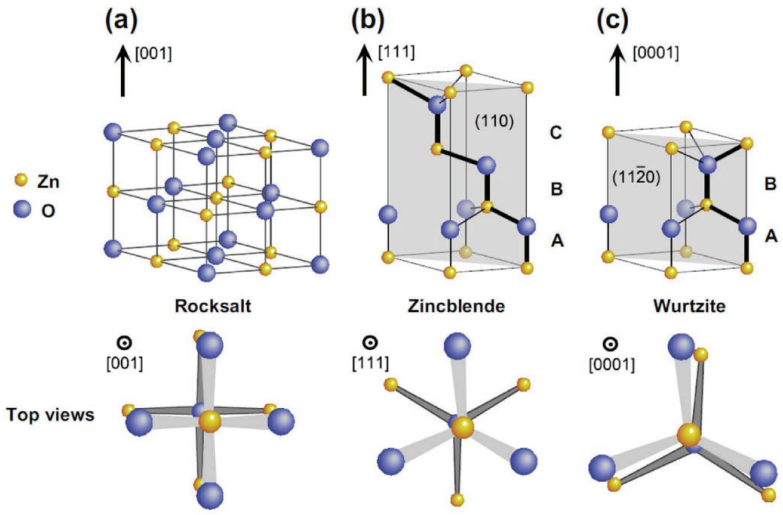

Figure 2.3: Three different structures of ZnO crystals. In ambient conditions, the wurtzite structure is most stable [54].

miniaturization of electrical networks, the research on varistor materials is still a very active field [58, 59, 60]. Other applications are possible to produce due to the different morphologies of ZnO. As mentioned above, high quality and strongly textured ZnO thin films can be deposited via PVD. The thin film can be applied in bio-sensing and microfluidic applications [61]. Since p-type ZnO is the main obstacle in achieving ZnO diode, He et al. reported a single ZnO nanowire device served as piezoelectric diodes [62]. Another recent popular device that uses piezoelectric properties of ZnO is nanogenerators [14, 63, 64]. The nanogenerator is composed of nanowire arrays and bending them separate the charges across the nanowire, thus generate a potential difference. By forming n-ZnO and p-GaN diode, Yang et al. [65, 66] developed an enhanced light emission by exploiting the piezo-phototronic effect. Besides the advantage mentioned before, ZnO is also resistive to high-energy radiation, which can create acceptors and donors, making it superior in space utilizations [67].

3 Theoretical background

Due to the piezoelectric-semiconductive nature of ZnO and the coupling effect, the fundamental theories about electrostatics, mechanics, piezoelectrics, and semiconductors are introduced in section 3.1, 3.2 and 3.3 respectively. The fundamental physics in semiconductor and the classical double Schottky barrier models are introduced.

3.1 Electrostatics

The Maxwell equations provide a continuum description of the electromagnetic theory. Even though the transport behavior involves the time variation of potential (or electric field), this study deals with steady situations. Therefore, the electrodynamic effect can be neglected, and the magnetic effect does not act in the framework.

It has been stated by Coulomb's law that the electric field induced by a stationary point charge is:

$$E_i(r_i) = \frac{q'}{4\pi\epsilon_0}\frac{r_i - r'_i}{|r_i - r'_i|^3} \tag{3.1.1}$$

in which the Latin indice i for 3D run over the range of $1-3$; q' is the amount of the charge; r_i is the position of the electric field; r'_i is the location of the point charge, and ϵ_0 is the permittivity. Thus, the electric field generated by a charged object which contains the charge density ρ at location r'_i is:

$$E_i(r_i) = \frac{1}{4\pi\epsilon_0}\int_{\mathbb{V}} \rho(r'_i)\frac{r_i - r'_i}{|r_i - r'_i|^3}\mathrm{d}v \tag{3.1.2}$$

Take divergence on both sides,

$$E_{i,i}(r_i) = \frac{1}{4\pi\epsilon_0}\int_{\mathbb{V}} \rho(r'_i)\frac{r_{i,i} - r'_{i,i}}{|r_i - r'_i|^3}\mathrm{d}v \tag{3.1.3}$$

where the comma in a subscript denotes spatial differentiation, for example, $E_{i,i} = \partial E_i/\partial x_i$ in

which x_i is the ith Cartesian coordinate direction. The Einstein summation convention is used for the repeated indices. In the above expression, the part regarding the divergence of the position is,

$$\frac{r_{i,i} - r'_{i,i}}{|r_i - r'_i|^3} = 4\pi\delta(|r_i - r'_i|) \tag{3.1.4}$$

where $\delta(r)$ is Dirac function

Actually, $\frac{r_{i,i}-r'_{i,i}}{|r_i-r'_i|^3}$ can be restructured as $(\frac{e_{i,i}}{|R_i|^2})$ where e_i is the unit radial vector and $R_i = r_i - r'_i$. By the divergence theorem, in the spherical coordinates,

$$\iiint_{\text{volume }\tau} \left(\frac{e_{i,i}}{|R_i|^2}\right) \mathrm{d}\tau = \iint_{\text{surface enclosing }\tau} \frac{e_i}{|R_i|^2} \cdot e_i \,\mathrm{d}\sigma = \int_{\phi=0}^{2\pi}\int_{\theta=0}^{\pi} \frac{1}{|R_i|^2}|R_i|^2 \sin\theta \,\mathrm{d}\theta \,\mathrm{d}\phi = 4\pi \tag{3.1.5}$$

where $\mathrm{d}\sigma = \left|\frac{\partial \mathbf{R}}{\partial\theta} \times \frac{\partial \mathbf{R}}{\partial\phi}\right| \mathrm{d}\theta \,\mathrm{d}\phi$

Hence the integral of $\left(\frac{e_{i,i}}{|R_i|^2}\right)$ is 4π over the volume including $|R_i| = 0$, but it is zero $\forall |R_i| > 0$; this implies that it is equivalent to $4\pi\delta(|R_i|)$.

Therefore, the combination Eq. 3.1.3 and Eq. 3.1.4 yields,

$$E_{i,i}(r_i) = \frac{1}{\epsilon_0}\int_{\mathbb{V}} \rho(r'_i)\ \delta(|r_i - r'_i|)\ \mathrm{d}^3 r'_i \tag{3.1.6}$$

Owing to the integral property of the Dirac function, the divergence of the electric field finally is expressed as,

$$E_{i,i}(r_i) = \rho(r_i)/\epsilon_0 \tag{3.1.7}$$

Since the electric field is the negative gradient of electric potential, the Gauss law can also be expressed as,

$$\phi_{,ii}(r_i) = -\rho(r_i)/\epsilon_0 \tag{3.1.8}$$

In fact, for the case of linear dielectrics, Eq. 3.1.8 is equivalent to:

$$D_{i,i} = \rho_{\text{free}} \tag{3.1.9}$$

in which D_i is the electric displacement and ρ_{free} denotes free charge density.

Since the electric displacement is expressed as:

$$D_i = \epsilon_0 E_i + P_i \tag{3.1.10}$$

where P_i is the polarization. Taking the divergence, one has,

$$D_{i,i} = \epsilon_0 E_{i,i} + P_{i,i} \tag{3.1.11}$$

where $P_{i,i} = -\rho_{bound}$, and $\rho = \rho_{\text{free}} + \rho_{\text{bound}}$. Hence Eq. 3.1.8 and Eq. 3.1.9 are equivalent.

The permittivity demonstrates above is applied for an isotropic material. For the transversely isotropic symmetry case as the Wurtzite structure ZnO, the permittivity ε_{ij} has the form,

$$\varepsilon_{ij} = \begin{bmatrix} \varepsilon_{11} & 0 & 0 \\ 0 & \varepsilon_{11} & 0 \\ 0 & 0 & \varepsilon_{33} \end{bmatrix} \tag{3.1.12}$$

If neglecting the spontaneous polarization, due to piezoelectricity, the polarization P_i is linearly proportional to strain S_{mn}:

$$P_i = e_{imn} S_{mn} \tag{3.1.13}$$

The piezoelectric tensor e_{imn} is transformed to the matrix form e_{ij} by the Voigt notation mn->j, following the rule $11 \to 1 \quad 22 \to 2 \quad 33 \to 3 \quad 23 \to 4 \quad 31 \to 5 \quad 12 \to 6$. Hence,

$$\boldsymbol{e}_{ij} = \begin{bmatrix} 0 & 0 & 0 & 0 & e_{15} & 0 \\ 0 & 0 & 0 & e_{15} & 0 & 0 \\ e_{31} & e_{31} & e_{33} & 0 & 0 & 0 \end{bmatrix} \tag{3.1.14}$$

3.2 Continuum mechanics

The solid materials are constructed by atoms or molecules that are separated by space. If one examines on the microscopic level, the solid materials exist defects such as interstitial, vacancies, dislocations, GBs, and even Cracks. These defects may affect the continuity of physical properties. However, for simplicity, certain physical phenomena can be modeled regarding the material as a continuum, which means the matter of the content is continuously distributed in the material volume. The continuum can be studied by dividing the body into infinitesimal elements which contain the properties of its collection.

3.2.1 Displacement and strain

A continuum body creates displacement when its configuration κ changes. The displacement has two components, rigid-body displacement and deformation. The initial configuration is denoted as $\kappa_0(\mathscr{B})$ and the current one is represented as $\kappa_t(\mathscr{B})$. It is often convenient to define a reference

configuration in which all the other configurations are referenced from and frequently the initial configuration $\kappa_0(\mathscr{B})$ is selected.

In the Lagrangian description, the position and physical properties are evolving with time. Usually, the referential configuration is set at $t = 0$. The motion of the continuum body is described by the mapping function $\chi(\cdot)$ from the initial configuration $\kappa_0(\mathscr{B})$ to the current configuration $\kappa_t(\mathscr{B})$.

The current position x_i at time t is described by the mapping function as,

$$x_i = \chi(X_i, t), \tag{3.2.1}$$

in which X_i represents the initial position and t is the current time. Hence, the displacement u_i can be defined as:

$$u_i = x_i - X_i. \tag{3.2.2}$$

The deformation gradient at time t is defined as:

$$F_{ij} := \frac{\partial x_i}{\partial X_j} = \frac{\partial u_i}{\partial X_j} - \delta_{ij}, \tag{3.2.3}$$

in which δ_{ij} is the Kronekcer delta.

The strain is a measurement of the relative displacement between the particles in the body, which ignores the rigid body movements. Hence, to know the change of the relative distance between the two adjacent particles for the undeformed and deformed states is essential to calculate the strain. The square of the distance of the neighbouring particles is:

$$dl^2 = dx_i dx_i = \frac{\partial x_i}{\partial X_j}\frac{\partial x_i}{\partial X_k} dX_j dX_k. \tag{3.2.4}$$

The square of the distance between two adjacent particles in the undeformed body is:

$$dL^2 = dX_i dX_i = dX_i dX_j \delta_{ij}. \tag{3.2.5}$$

Taking the difference between the two above equations, one has:

$$dl^2 - dL^2 = \left(\frac{\partial x_k}{\partial X_i}\frac{\partial x_k}{\partial X_j} - \delta_{ij}\right) dX_i dX_j = \left(F_{ki}F_{kj} - \delta_{ij}\right) dX_i dX_j. \tag{3.2.6}$$

Using Eq. 3.2.2 to replace x_i with $u_i + X_i$ gives:

$$dl^2 - dL^2 = \left(\frac{\partial u_i}{\partial X_j} + \frac{\partial u_j}{\partial X_i} + \frac{\partial u_k}{\partial X_i}\frac{\partial u_k}{\partial X_j}\right) dX_i dX_j = 2E_{ij} dX_i dX_j, \tag{3.2.7}$$

where E_{ij} is Green's strain tensor and is defined as:

$$E_{ij} = \frac{1}{2}\left(\frac{\partial u_i}{\partial X_j} + \frac{\partial u_j}{\partial X_i} + \frac{\partial u_k}{\partial X_i}\frac{\partial u_k}{\partial X_j}\right) \tag{3.2.8}$$

For adequately small displacements ($\frac{\partial u_i}{\partial X_j} \ll 1$) the second-order term can be ignored, hence,

$$E_{ij} \approx \frac{1}{2}\left(\frac{\partial u_i}{\partial X_j} + \frac{\partial u_j}{\partial X_i}\right) = S_{ij}, \tag{3.2.9}$$

where S_{ij} is the Cauchy strain tensor. In this work, the discussion of the strain is limited to the infinitesimal strain framework since the strain applied in this work is less than 0.12%.

3.2.2 Stress and balance principles

The forces in the continuum mechanics are acting on the particles in the body. These forces include surface traction acting on the boundary and body force acting in the interior of the body. The traction and body forces are defined for the unit area and volume, respectively. For the sub-volume $\mathscr{K}$ and its edge $\partial\mathscr{K}$ from the body $\mathscr{B}$, based on Newton's second law, the forces and motion of the body describing by the velocity v_i have the relation:

$$\int_{\mathscr{K}} \rho \dot{v}_i \mathrm{d}v = \int_{\partial\mathscr{K}} t_i \mathrm{d}s + \int_{\mathscr{K}} f_i \mathrm{d}v, \tag{3.2.10}$$

where ρ is the density, t_i is the traction, and f_i is the body force.

In continuum mechanics, the second order Cauchy stress tensor σ_{ij} is utilized to describe the stress states for a particle in the body $\mathscr{K}$. The traction force t_j can then be calculated from the stress tensor σ_{ij} and the surface normal vector n_i as:

$$t_j\left(n_i\right) = \sigma_{ij} n_i. \tag{3.2.11}$$

Ignoring the inertial contribution and applying the divergence theorem, Eq. 3.2.10 is rewritten as:

$$\int_{\mathscr{K}} \left(\sigma_{ij,j} + f_i\right) \mathrm{d}v = 0. \tag{3.2.12}$$

Since the above equation is valid for any arbitrary volume $\mathscr{K}$ in $\mathscr{B}$, it holds for any local balance:

$$\sigma_{ij,j} + f_i = 0 \quad \text{in} \quad \mathscr{B}. \tag{3.2.13}$$

At the equilibrium state, the summation of the moment is zero for any volume $\mathscr{K}$. Hence the symmetry for the stress tensor holds:

$$\sigma_{ij} = \sigma_{ji}. \tag{3.2.14}$$

The Hooke's law applies for the linear elastic material as:

$$\sigma_{ij} = c_{ijkl} S_{kl}, \tag{3.2.15}$$

where c_{ijkl} is the elastic tensor. ZnO, as a hexagonal wurtzite structure, has transverse isotropy. Therefore the number of the independent elastic constants is reduced to 5, as shown in the following:

$$c_{ij} = \begin{bmatrix} c_{11} & c_{12} & c_{13} & 0 & 0 & 0 \\ c_{12} & c_{11} & c_{13} & 0 & 0 & 0 \\ c_{13} & c_{13} & c_{33} & 0 & 0 & 0 \\ 0 & 0 & 0 & c_{44} & 0 & 0 \\ 0 & 0 & 0 & 0 & c_{44} & 0 \\ 0 & 0 & 0 & 0 & 0 & \frac{1}{2}(c_{11} - c_{12}) \end{bmatrix} \tag{3.2.16}$$

3.3 Piezoelectrics

The piezoelectricity can be either generated in crystals or molecular groups. In the crystal structures, this physical phenomenon is a linear electromechanical interaction. This property needs the crystalline material to have no inversion symmetry, which means the point group of the structure does not contain an inversion center, and it is non-centrosymmetric. Among all the 32 point groups, there are 21 non-centrosymmetric, and 20 of them have direct piezoelectricity (the exception is the cubic crystal system 433 since the piezoelectric charges cancel each other along <111> axes). When the piezoelectric crystal is under mechanical loading or thermal expansion (extraction), the positive and negative charge center deviated from each other. Therefore the electric dipole moments are formed. The dipole moment density, i.e., polarization P has a unit of C/m^2 and is used to characterize the intensity of the piezoelectric effect. Since the deformation of the crystal lattice is linearly corresponding to polarization, the polarization is also linearly proportional to strain and stress. This also demonstrates that the reversible process exists since the electric fields cause the deviation of the lattice, which initiates polarization.

The conversion between the electric signal and material deformation of the piezoelectric material make many application possible, for example, ultrasonic sound waves production, detection

generation of high voltages, and controlling movements in microscopic scales.

3.4 Physics in semiconductors

In this section, the basics of semiconductors and the calculations regarding the charge densities, the generation and recombination of electrons and holes, and the Fermi level are introduced.

3.4.1 General introduction to semiconductors

A semiconductor has a conductivity between metal and insulator. While in metal, the dominant charge carriers are electrons, in the semiconductor, there is an additional type of charge carrier, i.e., holes. They are generated when the electrons hop from the valance band to other energy states. The typical single element semiconductors are from the carbon group, for instance, silicon and germanium. A straightforward law to form compound semiconductors is the combination of the elements from Group III and Group V, and the combination of Group IIB and Group VI, for example, gallium arsenide, and zinc oxide.

Intrinsic semiconductors are the types without doping. The pure semiconductors are not useful due to the low conductivity. On the other hand, the impurity-doped semiconductors are widely applied in modern electronic devices since the electrical properties can be adjusted. By doping pentavalent or trivalent elements, additional electrons and holes are provided; hence the n and p-type semiconductors are formed. P and n-type semiconductors and the combination of them, which forms heterojunctions are the cornerstones of the electric devices. The typical elements of the electric devices are junction diode, transistors, MOSFET etc.

The semiconductors have several properties that other materials do not possess. For example, the resistance is different in one direction than another; the resistance is sensitive to light and heat. Usually, in the intrinsic semiconductors, if the electrons are excited (typically by thermal excitation) from valance band to conduction, the holes are generated in the valance band. Thus an electron-hole pair is produced. When an electric field is applied, the electrons and holes are moving toward opposite directions, which is called an ambipolar diffusion. The emergence of electron and hole pairs is termed as "generation", while "recombination" is an opposite process, which leads to the pairs annihilation. During the recombination process, the energies are released as thermal, optical energies, or excitation of other electrons. Naturally, the reverse process that the electrons are excited by the photons could cause electron-hole pair generation is also possible. Therefore, many applications are allowed due to the possibility of modifying the semiconductor electrical properties. For instance, the semiconductors are widely applied in energy conversion, sensors, switching, and light emissions.

In a medium, since the waves with different frequencies also travel at different speeds, the

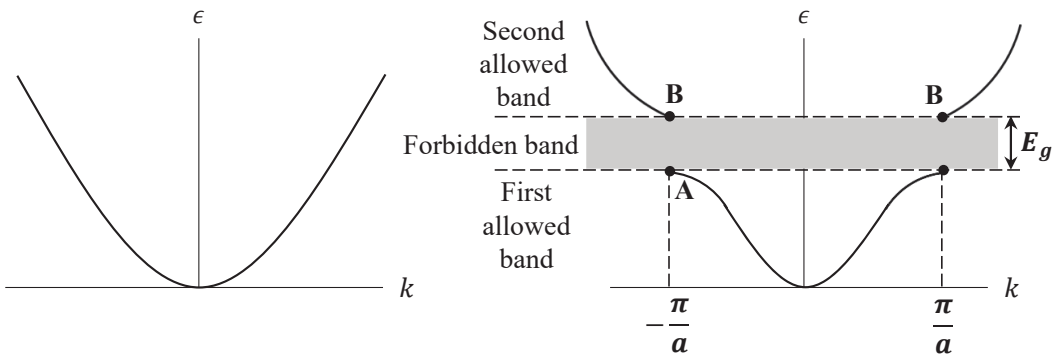

Figure 3.1: (a) Free electron energy with respect to wavevector; (b) Electron energy versus wavevector in a monatomic linear lattice with lattice constant a. The energy gap E_g is associated with the first Bragg reflection at $k = \pm\pi/a$; other gaps lie at $k = \pm n\pi/a$. [68]

wave packets disperse in space. Dispersion relationship is a relationship between wavelength (λ) or wavenumber (k) with frequency (ω), which is denoted as $\omega(\mathbf{k})$. Since energy is linearly proportional to frequency according to de Broglie relations, the dispersion relationship is also generally expressed by $\epsilon(\mathbf{k})$ where ϵ is energy. The first simple model describing the dispersion relationship is the free electron gas model, which outlines charge carrier behaviour in metallic solid. The free-electron gases are the electron gases which obey the Pauli principle, and the interactions between the electrons are neglected. The model uses periodic boundary conditions; therefore, it generates a plane wave function (for the electrons). When the plane wave function is combined with the Schrödinger equation, the dispersion relation is solved out, as shown in Fig. 3.1(a).

Nearly free electron model expands the free electron model. The new model includes the important fact that Bragg reflection for wave propagation is an intrinsic property in the lattice, and the reflection is the origin of the energy gap. The direction of the wave functions which match the Bragg reflection condition is reversed to the opposite direction. Unlike a normal wave, a standing wave stays the same and does not propagate. Some standing wave functions give lower energy states while others provide higher energy states. The energy levels which no state exist is the energy gap, as illustrated in Fig. 3.1. [69].

The allowed energy band characterises different electrical properties of materials. The insulator has the allowed energy bands either fully filled or totally empty. Thus no electrons can flow. The electrons fill the energy states of the metal for 10% to 90%. For semimetals or semiconductors, the bands are almost entirely filled or nearly empty. Thus the conductance of semiconductors is very limited.

The electrons in the crystal have some other remarkable properties, for instance, the effective mass m^*. An effective electron mass could be less or more than the electron mass, or even negative. It is an essential property since it describes the response of the electron to the electric field directly.

3.4.2 Charge carriers of non-degenerate semiconductors

In this section, the charge carrier concentration calculations for the non-degenerate semiconductors are introduced. The simplified calculation can significantly reduce the computational cost.

If the intrinsic semiconductor case is considered, the electrons densities which occupied the conduction energy states is calculated with:

$$n = \int_{\mathscr{E}_C}^{\infty} N(\mathscr{E}) F(\mathscr{E}) d\mathscr{E} \tag{3.4.1}$$

in which the $N(\mathscr{E})$ is the density of states near the bottom of the conduction band, and F($\mathscr{E}$) is Fermi-Dirac distribution, which represents the amount of the occupation of the density of states and is defined as:

$$F(\mathscr{E}) = \frac{1}{1 + \exp\left[\left(\mathscr{E} - \mathscr{E}_F\right)/kT\right]} \tag{3.4.2}$$

where $\mathscr{E}_F$ is the Fermi energy level.

If integrating Eq. 3.4.1, one could get:

$$n = N_C \frac{2}{\sqrt{\pi}} F_{1/2}\left(\frac{\mathscr{E}_F - \mathscr{E}_C}{kT}\right) \tag{3.4.3}$$

where N_C is the effective density of states in the conduction band, $\mathscr{E}_C$ is the bottom of the conduction band energy and $F_{1/2}$ is the Fermi-Dirac integral.

If we define $\eta \equiv \left(\mathscr{E} - \mathscr{E}_C\right)/kT$ and $\eta_F \equiv \left(\mathscr{E}_F - \mathscr{E}_C\right)/kT$, the Fermi-Dirac integral can be written as [70]:

$$\begin{aligned} F_{1/2}\left(\frac{\mathscr{E}_F - \mathscr{E}_C}{kT}\right) \equiv F_{1/2}\left(\eta_F\right) &= \int_{\mathscr{E}_C}^{\infty} \frac{\left[\left(\mathscr{E} - \mathscr{E}_C\right)/kT\right]^{1/2}}{1 + \exp\left[\left(\mathscr{E} - \mathscr{E}_F\right)/kT\right]} \frac{d\mathscr{E}}{kT} \\ &= \int_0^{\infty} \frac{\eta^{1/2}}{1 + \exp\left(\eta - \eta_F\right)} d\eta \end{aligned} \tag{3.4.4}$$

It could be calculated that when $\eta_F < -1$, the Fermi-Dirac integral is very close to exponential function $\left(\sqrt{\pi}/2\right)\exp\left(\eta_F\right)$. As a result, if $\mathscr{E}_f$ is lower than $\mathscr{E}_C - kT$, the Fermi-Dirac integral can be approximated by the exponential function. This approximation is thus suitable for all

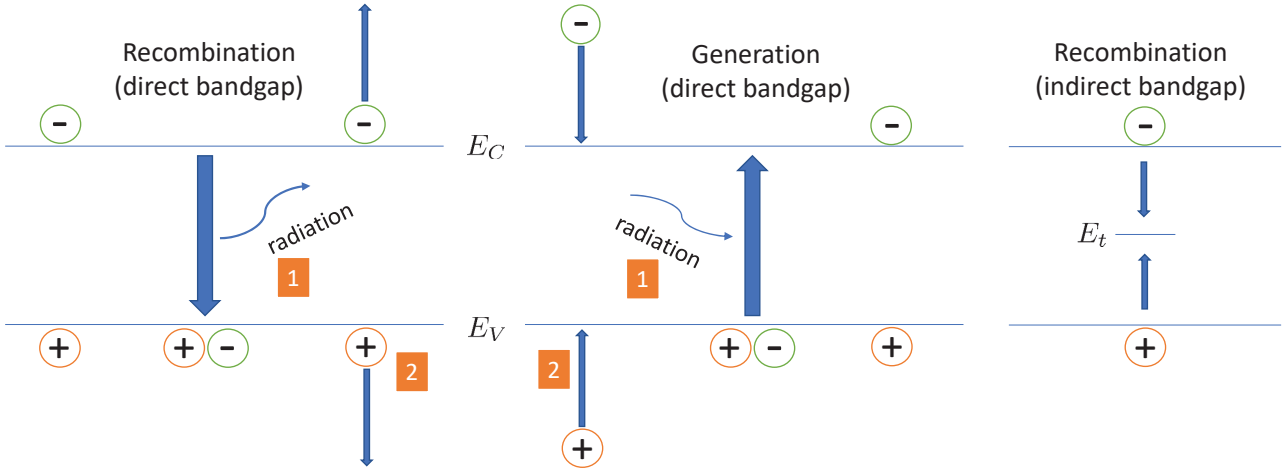

Figure 3.2: The left-hand side shows the recombination of electron and holes with energy release. The middle illustrates the generation process, which is reverse to recombination. The right-hand side one reveals recombination for an indirect bandgap material.

non-degenerate semiconductors. Therefore, Eq. 3.4.1 is turned into:

$$n = N_C \exp\left(-\frac{\mathscr{E}_C - \mathscr{E}_F}{kT}\right) \tag{3.4.5}$$

The same applies for holes:

$$p = N_V \exp\left(-\frac{\mathscr{E}_F - \mathscr{E}_V}{kT}\right) \tag{3.4.6}$$

where p is electron density and N_V is the effective density of states in the valence band.

3.4.3 Generation and recombination

When a semiconductor system is not under thermal-equilibrium condition, for instance, $pn \neq n_i^2$, the system tries to restore the equilibrium ($pn = n_i^2$) by generation and recombination process of electrons and holes. The generation happens when $pn < n_i^2$ and recombination occurs when $pn > n_i^2$. Fig. 3.2 illustrates generation and recombination process. In the recombination process, the electrons on the conduction band transit to the valance band, thus release energy. The energy can mainly be transferred into two forms, the first is that it is radiated as light, the second is the energy can be acquired by the electrons on the conduction band again and transit to a higher energy or, the holes transit to a deeper level. The generation is exactly the reverse process of recombination that the energy used to generate electron and hole pairs can be gained by radiation or the transition of electrons or holes from a higher energy level. Fig. 3.2 demonstrates a band-to-band transition, which is for the direct-bandgap semiconductors. The recombination

rate is defined as:

$$R_e = R_{ec} pn \tag{3.4.7}$$

where R_{ec} is recombination coefficient, which is related to thermal generation rate G_{th}:

$$R_{ec} = \frac{G_{th}}{n_i^2} \tag{3.4.8}$$

Therefore, R_{ec} is temperature and material dependent. Normally a direct-bandgap semiconductor has a much higher recombination rate than indirect-bandgap semiconductor. If the system is in equilibrium $pn = n_i^2$, then no new electron-hole pairs are generated or recombined ($R_e = G_{th}$). When it is in the non-equilibrium system, and the excess charge carriers (Δp or Δn) are low amount, the net transition U for an n-type semiconductor is defined:

$$\begin{aligned} U &= R_e - G_{th} = R_{ec}\left(pn - n_i^2\right) \\ &\approx R_{ec}\Delta p N_D \equiv \frac{\Delta p}{\tau_p} \end{aligned} \tag{3.4.9}$$

in which the lifetime for holes is:

$$\tau_p = \frac{1}{R_{ec} N_D} \tag{3.4.10}$$

for the p-type material,

$$\tau_n = \frac{1}{R_{ec} N_A} \tag{3.4.11}$$

For the indirect-bandgap semiconductors, it is more energy favorable that the recombination and generation occur via bulk traps, which has the density N_t and energy level $\mathscr{E}_t$ shown in Fig. 3.2. The net transition rate can be calculated with the Shockley-Read-Hall law [71, 72, 73]:

$$U = \frac{\sigma_n \sigma_p v_{th} N_t \left(pn - n_i^2\right)}{\sigma_n \left[n + n_i \exp\left(\frac{\mathscr{E}_t - \mathscr{E}_i}{kT}\right)\right] + \sigma_p \left[p + n_i \exp\left(\frac{\mathscr{E}_i - \mathscr{E}_t}{kT}\right)\right]} \tag{3.4.12}$$

in which σ_n and σ_p are the electron and hole capture cross-sections, respectively. It can be noticed that the net transition rate reaches its maximum when $\mathscr{E}_t = \mathscr{E}_i$, indicating that through the trap in the middle of the band, the transition is most efficient. If only consider the trap states in the middle, Eq. 3.4.12 is rewritten to:

$$U = \frac{\sigma_n \sigma_p v_{th} N_t \left(pn - n_i^2\right)}{\sigma_n \left(n + n_i\right) + \sigma_p \left(p + n_i\right)} \tag{3.4.13}$$

which is exactly the net transition rate using in the FE model in this dissertation.

3.4.4 Calculation of Fermi level

For an intrinsic semiconductor, the Fermi level lies very close to the middle of the bandgap. The charge densities have the relation $n = p = n_i$, where n_i is intrinsic carrier concentration. Once the impurities are doped into the material, in order to keep the electrically neutral state, the total amount of negative charges which contains n and N_A^- need to be the same as positive charges which contain p and N_D^-. The ionized donor density is: [74]

$$N_D^+ = \frac{N_D}{1 + g_D \exp\left[\left(\mathscr{E}_F - \mathscr{E}_D\right)/kT\right]} \tag{3.4.14}$$

in which g_D is the ground-state degeneracy of the donor impurity level. Since a donor energy level can contain one electron with two spin states (or empty), the g_D equals to 2.

The ionized acceptor densities have a similar expression:

$$N_A^- = \frac{N_A}{1 + g_A \exp\left[\left(\mathscr{E}_A - \mathscr{E}_F\right)/kT\right]} \tag{3.4.15}$$

where g_A is the ground state degeneracy level for acceptors. In this scenario, g_A has a value of 4 because each acceptor energy level can contain 2 hole spin states and this energy level is doubly degenerated at the wave vector $\boldsymbol{k} = 0$.

As mentioned, the charge neutrality rule is hold by:

$$n + N_A^- = p + N_D^+ \tag{3.4.16}$$

If one considers a n-type semiconductor which has $N_A^- \approx 0$, then:

$$\begin{aligned} n &= N_D^+ + p \\ &\approx N_D^+ \end{aligned} \tag{3.4.17}$$

thus the charge neutrality rule is expressed by:

$$N_C \exp\left(-\frac{\mathscr{E}_C - \mathscr{E}_F}{kT}\right) \approx \frac{N_D}{1 + 2\exp\left[\left(\mathscr{E}_F - \mathscr{E}_D\right)/kT\right]} \tag{3.4.18}$$

Therefore, the Fermi level $\mathscr{E}_F$ can be determined by knowing N_D, $\mathscr{E}_D$, N_C, and T. For a bicrystal which has barrier height at the GB, Eq. 3.4.18 is applied in the bulk far away from GB. Note that this calculation is valid for non-degenerate semiconductors.

Fig. 3.3 illustrates the amount of electron and ionized donors vary with the Fermi energy under

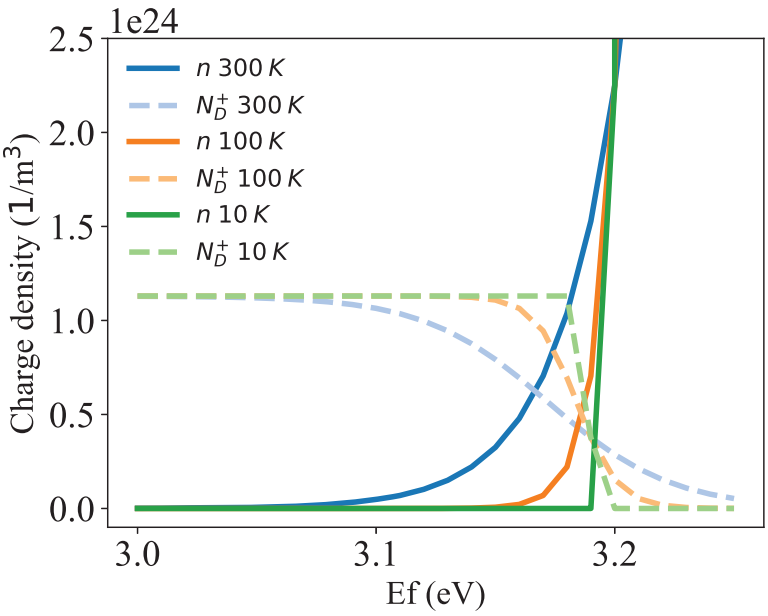

Figure 3.3: Electron and ionized donor density against Fermi energy, with the data from Table 4.1.

a variety of temperatures. The charge neutrality rule determines the Fermi level, which is the cross-section of electron and ionized donor curves under each temperature. With decreasing the temperature, the Fermi level increases while the charge density decreases, which is as expected that lower temperatures are leading to fewer electrons jumping from the donor energy level to the conduction band. If the temperature decreases approaching 0 K, due to degeneracy, Eq. 3.4.5 is not applicable anymore. However, it can be inferred that at 0K, no electron hopping to the conduction band, and the Fermi level lies between $\mathscr{E}_D$ and $\mathscr{E}_C$. The same applies to the p-type semiconductor by $p \approx N_A^+$, which can determine the Fermi level and the number of holes and ionized acceptors.

3.5 Grain boundary

Grain boundaries are the interfaces between two grains. It is a type of 2D defects, and the most straightforward boundaries are tilt and twist GBs. A tilt GB has the rotation axis parallel to the boundary plane, while the rotation axis of a twist GB is perpendicular to the boundary plane. The GBs can be categorized by misorientation. The properties of the GBs are critical to nowadays electronic devices whose performance-based on polycrystalline materials since the atomic structures of GBs significantly affect the electrons transportation. A less than 15 degrees misorientation is called low-angle GBs, and those who are more than 15 degrees are high-angle GBs. The low-angle GBs are formed of a pile of dislocations, as demonstrated in Fig. 3.4 and

the properties of these GBs are a function of the misorientation angles. The properties for the high-angle GBs, however, is typically independent of the misorientation angle.

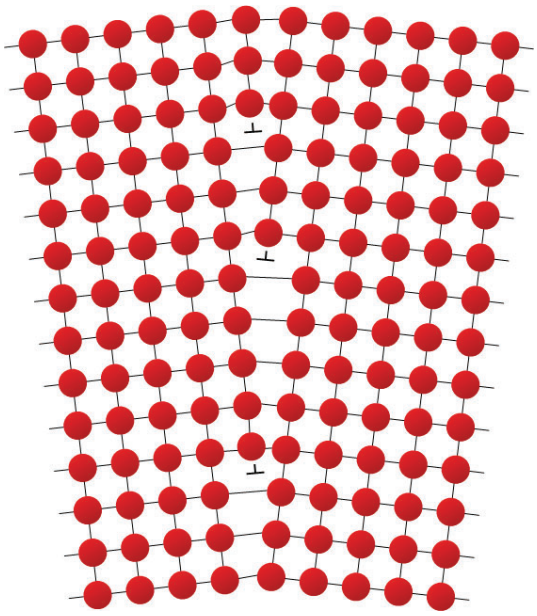

Figure 3.4: Demonstration of low angle GB. The vertical surface in the middle is the GB which is composed of several dislocations and distorted lattices.

The high-angle GBs are more disordered than the low-angles one. Previously, they were thought to be some form of amorphous structures. With the development of electron microscopy, new studies proved that the high-angle GBs are composed of structural units (examples are shown in Table 3.1), which is dependent on the macroscopic degrees of freedom, for instance, tilt, rotation, interface [75, 76]. The description of the structural units is related to the concept of coincidence site lattice (CSL) theory.

The CSL theory describes the repeated units that are composed of the points which are shared by two misorientated lattices. Hence these units are called primitive coincidence site cells. The parameters which depict the degrees of coincidence is the degree of fit (Σ). Σ is the reciprocal of the ratio between the points that are shared by the two lattices and the total points on the boundary. For example, $\Sigma = 3$ means there are $1/3$ of the points shared by the two interface latices together. Since more coincidence sites produce lower energy, high Σ implies a high energy boundary. Some low-Σ have unique properties such as the coherent twin boundaries ($\Sigma 3$); $\Sigma 1$ GB implies a low-angle GB, and the distortion is wholly composed of dislocations.

In Fig. 3.5 (a) and (c), a clear repeated 6684 unit structure is found along the ZnO GB. This demonstrates that the structural units are the fundamental bricks of GB, but not amorphous structures.

The atomic structures in Fig. 3.5, 3.4 and Table 3.1 all demonstrates that either high or low angle GBs can have dangling bonds, which are regarded as defects and can trap electrons inside

Core structure	Name	Core structure	Name
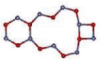	6684	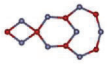	468
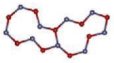	Faceted 5757		457
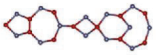	57468		Straight 5757
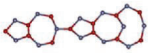	57578	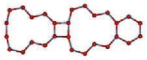	864866

Table 3.1: Boundary structure units of $\Sigma 13$. The left and right columns are $27.8°$ and $32.2°$ [0001] tilt GB.[77]

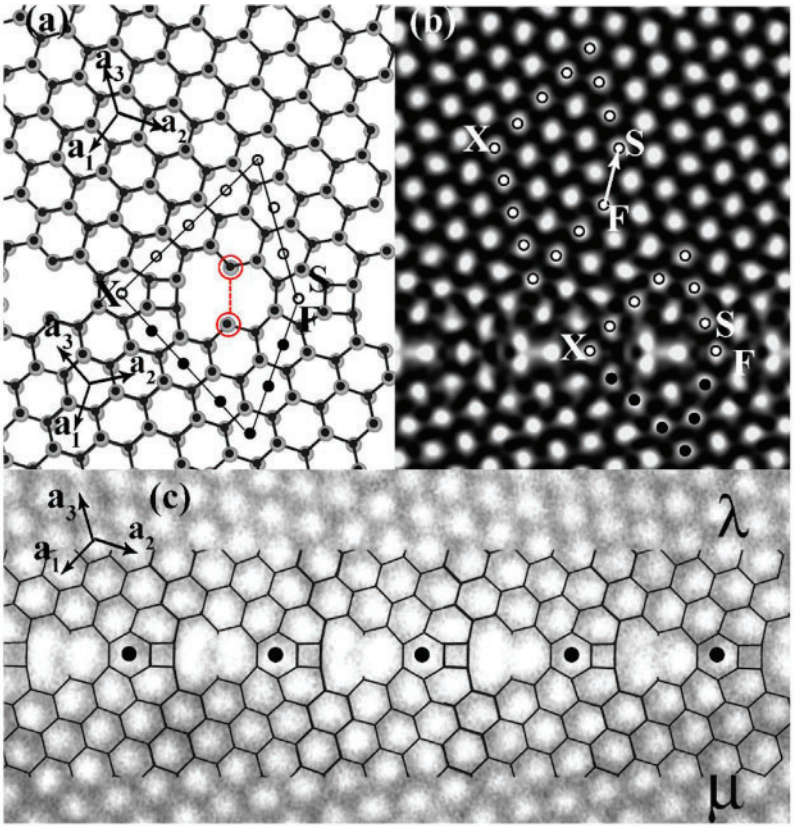

Figure 3.5: Atomic structure of $\Sigma 13$ GB of ZnO hexagonal structure. (a) A periodic atom model of 6684 unit structure; (b) the corresponding simulated image; (c) high resolution TEM image for $27.8°$ tilt GB. This unit structure clearly shows the dangling bonds. [77]

the GB. The GB can also trap dopant or other impurities atoms, which can promote the formation of dopant-like and acceptors-like defects. For example, Bi and Pr promote the formation of acceptor like defects, such as Zn-vacancy V_{Zn} and Oxygen-interstitial O_i[78, 79]. The change of the electrical states at GB has an effect on the electric field; thus, the electric potential can be

altered.

3.6 Classical double Schottky barrier height models

In this section, three classical double Schottky barrier height models are introduced. The model by Blatter and Greuter includes the consistency of the trap charge density and the barrier height. Verghese and Clarke took the piezoelectricity into the calculation. However, he neglected the consistency created by Blatter and Greuter. Raschid Baraki combined them both and made a relatively comprehensive model for the piezotronics.

3.6.1 Model by Blatter and Greuter

Blatter and Greuter [34, 35, 30] developed a self-consistent barrier height model that considers the intricate coupling between the trap charge density Q_I and the barrier height Φ_B at GBs using the density of states theory. They assumed a charge density distribution, which has the form as shown in Eq. 3.6.1:

$$\rho(x) = qN_0 \left[H(x + x_l) - H(x - x_r)\right] + Q_I \delta(x) \tag{3.6.1}$$

where H and δ are the Heaviside function and the Delta function; $q = |q|$ is the elementary charge, N_0 is the ionized donor density and Q_I the surface trap charge density; the coordinate x lies perpendicular to the GB and has its origin at the GB; the to-be-determined x_l and x_r are the left and right edge of the ionized donors, which are also the limits for the depletion region. The distribution of Eq. 3.6.1 is demonstrated in Fig. 3.6b, which has a box shape[35]. Another type of charge distribution assumption is the superposition of the ionized donor charge boxes, which is also given by Blatter and Greuter[34]. In the latter assumption, the temperature is not restricted to 0 K.

The Heaviside function is also known as unit step function and is defined as

$$H(x) := \frac{d}{dx} \max\{x, 0\} \quad \text{for } x \neq 0, \tag{3.6.2}$$

where $\max\{x, 0\}$ is the ramp function. The illustration of the function is shown in Fig. 3.6a. This function is employed since it can mimic a real charge distribution in the depletion region at 0 K. Besides, solving the analytical solution is straightforward with a simple assumption. [35]

To obtain the electrostatic solution, one applies the assumed charge distribution $\rho(x)$ to the

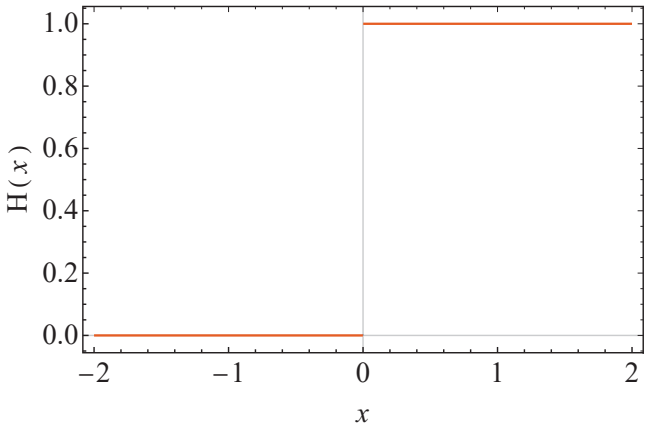

(a) Illustration of a Heaviside step function, where the step lies at $x = 0$ [80].

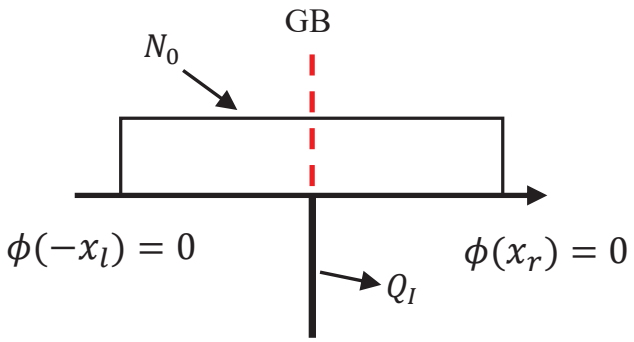

(b) Assumption of charge distributions for a bicrystal at 0 K. N_0 is the ionised donors.

Figure 3.6: Heaviside function and the assumption of charge distributions.

Poisson equation

$$-\epsilon\frac{d^2\Phi}{dx^2} = \rho(x), \tag{3.6.3}$$

with ϵ being the permittivity of bulk material and $\Phi = -\phi$ since we let $q\Phi$ represent the energy of the electrons. Considering the external applied voltage V the following boundary and interface condition were assumed,

$$\Phi(-\infty) = \Phi\left(-x_l\right) = 0 \quad \text{and} \quad \Phi(\infty) = \Phi\left(x_r\right) = -V, \tag{3.6.4}$$

$$\Phi'(-x_l) = \Phi'(x_r) = 0. \tag{3.6.5}$$

Assuming the barrier height is ϕ_b at the interface $x = 0$ and using the continuity produces the other two boundary conditions,

$$\Phi\left(0^-\right) = \Phi\left(0^+\right) = -\Phi_B \quad \text{and} \quad \Phi'\left(0^-\right) - \Phi'\left(0^+\right) = Q_I/\epsilon_s. \tag{3.6.6}$$

Thus for $-x_l \leq x \leq 0$,

$$\frac{d\Phi(x)}{dx} = qN_0x + A_1, \tag{3.6.7}$$

$$\Phi(x) = \frac{1}{2}qN_0x^2 + A_1x + B_1, \tag{3.6.8}$$

where A_1, B_1 and x_l are to be determined. Hence with boundary conditions 3.6.4 and 3.6.5

yields,

$$qN_0x_l + A_1 = 0, \tag{3.6.9}$$

$$\frac{1}{2}qN_0x_l^2 + A_1x_l + B_1 = 0, \tag{3.6.10}$$

For $0 \leq x \leq x_r$,

$$\frac{d\Phi(x)}{dx} = qN_0x + A_2, \tag{3.6.11}$$

$$\Phi(x) = \frac{1}{2}qN_0x^2 + A_2x + B_2, \tag{3.6.12}$$

where A_2, B_2 and x_r are to be determined. Applying again the boundary conditions 3.6.4 and 3.6.5, one has,

$$qN_0x_r + A_2 = 0, \tag{3.6.13}$$

$$\frac{1}{2}qN_0x_r^2 + A_1x_r + B_2 = -V, \tag{3.6.14}$$

For $x = 0$, take the boundary condition 3.6.6

$$B_1 = \Phi_B, \tag{3.6.15}$$

$$B_2 = \Phi_B, \tag{3.6.16}$$

$$A_1 - A_2 = \frac{Q_I}{\epsilon_s}. \tag{3.6.17}$$

Consequently, there are seven unknowns to be determined, A_1, A_2, B_1, B_2, x_l, x_r, Φ_B and seven equations including Eq. 3.6.9-3.6.10, Eq. 3.6.13-3.6.17. Hence, the barrier height, the distribution of Φ and the edge of depletion layer x_l and x_r are resolved. The results are shown below,

$$\Phi(x) = \begin{cases} \frac{\gamma_0}{2}(x + x_l)^2, & -x_l \leq x \leq 0 \\ \frac{\gamma_0}{2}(x - x_r)^2 - V, & 0 \leq x \leq x_r \end{cases} \tag{3.6.18}$$

where the left and right depletion boundaries x_l and x_r are:

$$x_l = \left(\frac{V_c}{2\gamma_0}\right)^{1/2}\left(1 - \frac{V}{V_c}\right), \tag{3.6.19}$$

$$x_r = \left(\frac{V_c}{2\gamma_0}\right)^{1/2}\left(1 + \frac{V}{V_c}\right), \tag{3.6.20}$$

in which $\gamma_0 = \frac{qN_0}{\epsilon_s}$ and V_c is the critical voltage which is,

$$V_c = \frac{1}{2\gamma_0}\left(\frac{Q_I}{\epsilon_0\epsilon}\right)^2. \tag{3.6.21}$$

The barrier height then is dependent on critical voltage and expressed as,

$$\Phi_b = \frac{1}{4}V_c\left(1 - \frac{V}{V_c}\right)^2. \tag{3.6.22}$$

It is then apparent that if the external voltage V reaches V_c, then the barrier height drops to zero.

The trap charge density is governed by a self-consistent calculation. The amount of it is dependent on the trap DOS $\mathscr{D}(\mathscr{E})$, Fermi distribution $F(\mathscr{E})$ and quasi-Fermi level $\xi_I(V)$,

$$Q_I = q\int_{\xi_I^n}^{\infty}\mathscr{D}(\mathscr{E})F(\mathscr{E})d\mathscr{E}, \tag{3.6.23}$$

$$F(\mathscr{E}) = \frac{1}{1+\exp\left(\frac{\mathscr{E}-\xi_I(V)}{kT}\right)}, \tag{3.6.24}$$

$$\xi_I(V) = \mathscr{E}_f - kTln\frac{2}{1+\exp(\frac{-qV}{kT})}, \tag{3.6.25}$$

where q is the positive elementary charge, k is the Boltzmann constant, T is the absolute temperature (K), and $\xi_I(V)$ is the quasi-Fermi level.

Blatter and Greuter [34] chose three distribution types of density of states $\mathscr{D}(\mathscr{E})$ to model the GB physics: the Delta distribution, Gaussian distribution and step distribution, which are defined as,

$$\mathscr{D}_{delta}(\mathscr{E}) = N_t\cdot\delta\left(\mathscr{E} - (\mathscr{E}_I + \Phi_B)\right) \tag{3.6.26}$$

$$\mathscr{D}_{Gau}(\mathscr{E}) = N_t\exp\left\{-\left[\left(\mathscr{E} - \mathscr{E}_I - \Phi_B\right)/\mathscr{E}_{Gau}^g\right]^2\right\} \tag{3.6.27}$$

$$\mathscr{D}_{box}(\mathscr{E}) = N_t\left[H\left(\mathscr{E} - \mathscr{E}_I - \phi_B + \mathscr{E}_{box}^g/2\right) - H\left(\mathscr{E} - \mathscr{E}_I - \phi_B - \mathscr{E}_{box}^g/2\right)\right] \tag{3.6.28}$$

in which $\mathscr{E}_{Gau}^g$ and $\mathscr{E}_{box}^g$ are the characteristic decay energies for the Gaussian and the box distributions.

3.6.2 The piezoelectric model by Verghese and Clarke

Verghese and Clarke have investigated the piezoelectric effect in the polycrystalline ZnO within a stochastic framework. [81] They conducted the numerical simulation on the impact of thermal stress in polycrystalline on the GB electrical characteristics on the macroscopic transport behaviour. The results indicate that considering the statistical random distribution of grains leads to a decrease

in nonlinearity in the I-V curve, comparing to the simple configuration, e.g., bicrystals.

The barrier heights mainly determine the GB electrical characteristics at the GBs. With considering expansion of the crystal constituents and the thermal expansion mismatch between phases, Verghese introduced internal stresses in the calculation of barrier heights:

$$\Phi_B = \frac{\left[-qN_t + \mathbf{n}\cdot(\mathbf{P}_l - \mathbf{P}_r)\right]^2}{8q\epsilon_s N_d} \tag{3.6.29}$$

in which N_t is the trap charge density, $\mathbf{n}$ is the GB normal vector; $\mathbf{P}_l$ and $\mathbf{P}_r$ are the polarisation vectors for the left and right-hand side of the grains respectively. The polarisation can be expressed by the the multiplication of the stress $\boldsymbol{\sigma}$ and piezoelectric coefficient $\mathbf{d}$, i.e. $\mathbf{P} = \mathbf{d}\boldsymbol{\sigma}$ when neglecting the spontaneous polarisation.

Verghese and Clarke focused on the stress distributions on the crystal boundaries and their impact on the flux. Comparing to the work done by Blatter and Greuter, they neglected the self-consistent effect and the effect of the flux on the barrier height. Nonetheless, they introduced the idea on how to introduce the piezoelectric charges at the GB into the barrier height calculation.

3.6.3 The piezoelectric model of Baraki et al.

In order to study the varistor effect of polycrystalline ZnO crystal depending for different external loadings, Baraki et al.[20] extended the phenomenological model from Blatter and Greuter by counting the piezoelectric charge at the GB into the calculation:

$$\Phi_B = \frac{\left((Q_I + Q_P)^2 - 2qN_d V\varepsilon_s\right)^2}{8qN_d\left(Q_I + Q_P\right)^2\varepsilon_s}. \tag{3.6.30}$$

where $Q_P = \mathbf{n}\cdot(\mathbf{P}_l - \mathbf{P}_r)$, as in the paper from Verghese and Clarke.

The necessary components for the barrier height calculation, for instance, GB charge density Q_I, GB trap charge DOS $\mathscr{D}_{delta}$, Fermi distribution $f(E)$ and the quasi-Fermi energy $\xi_I(V)$ are the same as defined in Blatter and Greuter's work.

In the paper, the authors investigated ZnO polycrystals by testing the I-V behaviour with varying external stresses and temperatures. They also applied the Richardson law Eq. 4.3.1 to compute the flux,

$$J(V) = A\cdot T^2\cdot\exp\left(\frac{-\Phi_B(V)}{kT}\right)\cdot\left(1-\exp\left(\frac{-qV}{kT}\right)\right).$$

However, this phenomenological equation which is developed for a bicrystal has difficulty in fitting the experimental data. The experiment can hardly reveal the supposing linear relationship between J/T^2 and $1/T$. Hence, the authors suggested that the flux percolation process is uneven

in the polycrystals since for some current paths, the GBs are less, and for some, the residual stresses lower the barrier height.

These two kinds of paths are more preferred than the others, and the authors proposed that the whole flux is combined by the fluxes from the easy current paths and the rest paths,

$$J = J_1 + J_2 = (1 - S) \cdot A \cdot T^2 \cdot \exp\left(\frac{-\Phi_{B1}(V)}{kT}\right) + S \cdot A \cdot T^2 \cdot \exp\left(\frac{-\Phi_{B2}(V)}{kT}\right) \tag{3.6.31}$$

where S is a weight factor for the difficult path ways.

Hence, the polycrystal cannot be simply rationalized by a bicrystal phenomenological model.

K.A.Taylor et al.[82] used the finite element model to firstly calculate the stress distributions along the GBs and then applied them in the GB resistivity calculation. He then used a nonlinear circuit model and also successfully calculated the resistivity of the bulk.

The model proposed by Baraki et al.[20] and K.A.Taylor el al.[82] successfully depicts the effect of the piezotronics, namely the varistor and piezoelectric effect. However, the internal electric field aroused from the gradient of the potential profile in the depletion region is neglected. Due to the inverse piezoelectric effect, this internal electric effect can change the strain, consequently modifies the polarization. As a result, the polarization charge at the GB is modified, and even space piezoelectric charge can be found in the depletion region.

4 Impact of the internal electric field on the barrier height

The GB is a structure that the crystals between the adjacent grains mismatch with each other. Since this mismatch creates dislocations, dangling bonds and other interface defects, trap states are created at the GB. Another way to create the trap states at the interface is to introduce the dopant or impurity atoms that can act as donors or acceptors. In this work, we consider the acceptor type of impurities. Consequently, semiconductor GB can trap electrons. When the energies of the states are lower than the Fermi energy, the electrons fill these low energy states and are trapped inside the GB. These electrons lead to a screening effect on the other electrons in the depletion region, thus leaves a positively charged region. Hence, a space charge develops. In this chapter, it will show that the trap charges can cause a strong internal electric field which influences the polarization at the depletion region and needs to be taken into account in the barrier height calculation model.

4.1 Formation of the internal electric field

A classical phenomenological model is developed by Blatter and Greuter [34, 35, 30] to calculate the barrier height and flux of the bicrystal. However, in this model, the polarization charge is not considered, as shown in Chapter 3.6.1.

In order to include the effect of the residual thermal stress between phases, Verghese and Clarke [37] extended the above model by adding the thermal stress induced piezoelectric charge Q_P at GB to the electrostatic calculation. Nevertheless, the trap charge density Q_I at GB was assumed to be constant, which is demonstrated in Chapter 3.6.2.

In Chapter 3.6.3, it has shown that Baraki et al. [20] proposed a phenomenological model that combined the two models. In his model, the interface charge is the superposition of polarization charge and trap charge densities. With this set of systems, the piezotronic character can be calculated phenomenologically. In the work of Verghese and Clarke [37] and Baraki et al. [20], the piezoelectric charge is formulated merely from the direct piezoelectric effect, namely the electric response of the material to the mechanical loading. The piezoelectric charge can be

obtained from the superposition of the normal components of the piezoelectric polarization on both sides of the GB. Thus, in their work, the piezoelectric charge is:

$$Q_P = 2\sigma\frac{e}{Y} \tag{4.1.1}$$

with σ, Y, e being the applied stress (positive for tension), the Young's modulus, and the piezoelectric constant.

However, the piezoelectric charge should not only result from the direct piezoelectric effect, but also from the inverse piezoelectric effect, which refers to the mechanical response (e.g., strain) of the material by the electric field. Kusaka et al. [83] used the effect of the inverse piezo effect to explain the Schottky barrier height difference between two types of polar surfaces of II-VI and III-V compounds, while Lagowski and Gatos [84] attributed the photomechanical effect of CdS to the inverse piezo effect. In the study of more recent III-V or II-VI semiconductor junction devices, there is, nevertheless, no explicit work for the impact of the inverse piezoelectric effect for double Schottky contacts. There exist a few numerical studies [85] which include both the direct and the inverse piezoelectricity. However, both direct and inverse piezoelectric effect should be taken into account for ZnO varistor material and its piezotronic applications.

Due to the charges at the GB, a strong internal electric field can be expected, and it leads to strain change through the inverse piezoelectric effect and the polarization charge density in the depletion layer. This strain further modifies the polarization and thus leads to additional piezoelectric charges at the GB and in the depletion layer. Thus, this should also be taken into account self-consistently.

4.2 Modified phenomenological model (MPM)

It is necessary to define the grain orientations due to the anisotropy of the material. Hereafter, head-to-head and tail-to-tail refer to the induced polarization direction for the bicrystal under compressive stress. Note that the polarization charge due to the spontaneous polarization is neglected, as it is usually done in the literature. [86] Thus, the piezoelectric charge is positive for both the case of head-to-head under compression and the case of tail-to-tail under tension. For the sake of simplicity and its importance to single-junction devices, a model with single GB, such as tail-to-tail or head-to-head, is considered.

The stress loading σ in 1D is shown in Fig. 4.1, and its expression is given as,

$$\sigma = YS + eE. \tag{4.2.1}$$

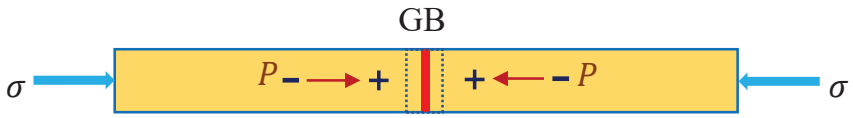

Figure 4.1: Configuration of the bicrystal. The induced polarizations P by the external loading σ align head-to-head with each other.

The strain can be computed from linear piezoelectricity theory as,

$$S = \frac{\sigma}{Y} + e\frac{E}{Y}, \tag{4.2.2}$$

in which the first term on the right-hand side is the elastic contribution, while the second term results from the inverse piezoelectric effect. Since the piezoelectric polarization is given by,

$$P = eS, \tag{4.2.3}$$

which is shown in Fig. 4.1. One then has the corresponding piezoelectric charge,

$$Q_P = 2\frac{\sigma}{Y}e + \frac{e^2}{Y}(E_l - E_r), \tag{4.2.4}$$

where E_l, E_r are the normal components of the electric field at GB in the left and the right grain, respectively. The field E_l, E_r should be self-consistently determined from the GB barrier height and depend on the trap charges at GBs, mechanical loading and applied voltage. Equation (4.2.4) demonstrates that the piezoelectric charge contains not only the direct piezoelectric contribution $2\sigma e/Y$, but also the inverse piezoelectric contribution $e^2(E_l - E_r)/Y$ depending on the internal electric field. It is worth to mention that this field is challenging to be detected from the external field. Subsequently, it is difficult to determine the internal electric field experimentally.

Furthermore, the inverse piezo effect induces an additional space charge in the depletion layer. The electric field E in the depletion layer is inhomogeneous and varies almost linearly. The piezoelectric polarization reads

$$P = e\frac{\sigma}{Y} + e^2\frac{E}{Y}, \tag{4.2.5}$$

with the two terms corresponding to the direct and the inverse piezo effect, respectively.

The stress is homogeneous, while the electric field E varies strongly. Hence, the polarization varies almost linearly in the depletion layer. This inhomogeneity of the polarization leads to space charge with density:

$$\rho_p = -\nabla P = -e^2\frac{\nabla E}{Y}. \tag{4.2.6}$$

In the present work, the complete version of the piezoelectric charge Eq. 4.2.4 at the GB interface

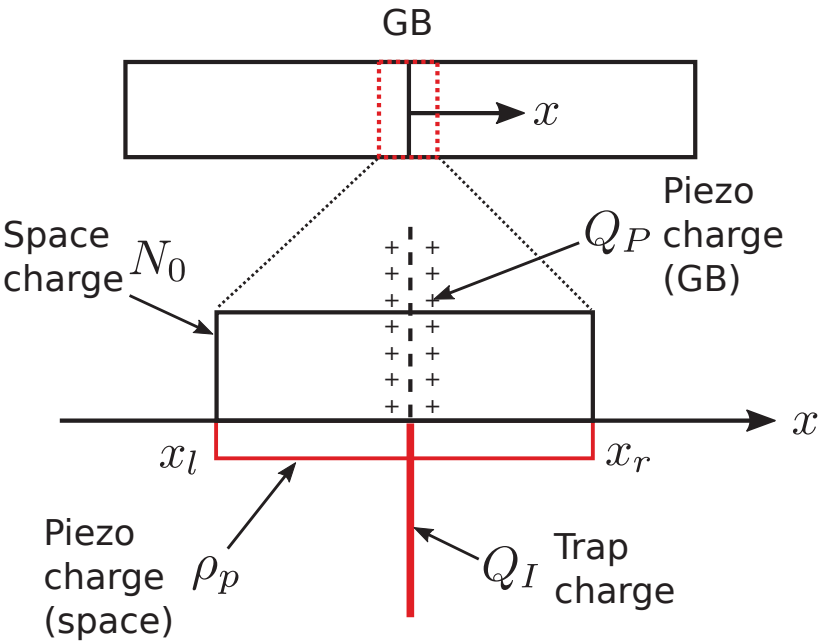

Figure 4.2: The 1D bicrystal configuration and the assumed charge distributions.

and also the space charge Eq. 4.2.6 in the depletion layer induced by the inverse piezoelectric effect was considered. To obtain the barrier height at the GB, the configuration of the charge distribution as assumed by Blatter and Greuter [34] will be modified accordingly. As shown in Fig. 4.2, the interface charge at the GB $\tilde{Q}_I$ and the space charge $\tilde{N}_0$ in the depletion layer each contains two contributions:

$$\tilde{Q}_I = Q_I + Q_P \tag{4.2.7}$$

$$q\tilde{N}_0 = qN_0 + \rho_p \tag{4.2.8}$$

A Heavside step distribution of the space charge $q\tilde{N}_0$ and a Dirac delta distribution of the interface charge density $\tilde{Q}_I = Q_I + Q_P$ at GB are hence applied. In other words

$$\rho(x) = q\tilde{N}_0 \left[H(x + x_l) - H(x - x_r)\right] + \tilde{Q}_I \delta(x) \tag{4.2.9}$$

It should be, however, noted that the piezoelectric charge Q_P is related to the to-be-determined internal electric field E via Eq. 4.2.4.

In the depletion region, the inverse of the potential Φ and the electric field can be expressed

by [34]

$$\Phi(x) = \begin{cases} \frac{\tilde{\gamma}}{2}(x+\tilde{x}_l)^2 & -x_l \leq x \leq 0 \\ \frac{\tilde{\gamma}}{2}(x-\tilde{x}_r)^2 - V & 0 \leq x \leq x_r \end{cases} \tag{4.2.10}$$

$$E(x) = \begin{cases} \tilde{\gamma}\,(x+\tilde{x}_l) & -x_l \leq x \leq 0 \\ \tilde{\gamma}\,(x-\tilde{x}_r) & 0 \leq x \leq x_r \end{cases} \tag{4.2.11}$$

with the obtained boundaries of the depletion layer

$$\tilde{x}_l = \left(\frac{\tilde{V}_c}{2\tilde{\gamma}_0}\right)^{1/2}\left(1 - \frac{V}{\tilde{V}_c}\right), \tag{4.2.12}$$

$$\tilde{x}_l = \left(\frac{\tilde{V}_c}{2\tilde{\gamma}_0}\right)^{1/2}\left(1 + \frac{V}{\tilde{V}_c}\right), \tag{4.2.13}$$

in which the definitions of $\tilde{\gamma}_0$ and $\tilde{V}_c$ is given by,

$$\tilde{\gamma}_0 = \frac{q\tilde{N}_0}{\epsilon_s} \tag{4.2.14}$$

$$\tilde{V}_c = \frac{1}{2\tilde{\gamma}_0}\left(\frac{\tilde{Q}_I}{\epsilon_s}\right)^2. \tag{4.2.15}$$

In the derivation of Eq. 4.2.11, it is assumed that the field in the depletion layer is linear, ρ_p remains constant there, and thus $\tilde{N}_0$ is a constant. More exactly, one has $\nabla E = \tilde{\gamma}_0 = q\tilde{N}_0/\epsilon$ and then $\rho_p = -e^2 q\tilde{N}_0/Y\epsilon$ from Eq. 4.2.6. Thus from Eq. 4.2.8,

$$\tilde{N}_0 = (1-f)N_0 \tag{4.2.16}$$

$$f = \frac{e^2}{\epsilon Y + e^2} \tag{4.2.17}$$

In particular, f in expression 4.2.17 is a dimensionless coefficient based on Young's modulus, the dielectric and the piezoelectric constant. The term $-fN_0$ in Eq. 4.2.16 is due to the space charge associated with the inhomogeneous electric field. We now determine the electric field E, the piezoelectric charge Q_P and the barrier height Φ_B self-consistently. From Eq. 4.2.11 the electric field at the GB reads,

$$E_l = \tilde{\gamma}_0\tilde{x}_l, \tag{4.2.18}$$

$$E_r = \tilde{\gamma}_0\tilde{x}_r. \tag{4.2.19}$$

Inserting Eq. 4.2.18 and 4.2.19 into Eq. 4.2.4, one can solve then the resulting equation with respect to Q_P. It yields,

$$Q_P = (1-f)\,2\frac{\sigma}{Y}e - f\,Q_I, \tag{4.2.20}$$

The internal fields E_l, E_r can be expressed explicitly via Q_I, σ, V after one replaces the last equation into Eq. 4.2.18 and 4.2.19. As it will be discussed later, the trap charge Q_I can be formulated by the barrier height using different trap charge density of states. It is evident that the piezoelectric charge depends on the trap charge Q_I and the mechanical loading, but independent of the applied voltage. The two terms in Eq. 4.2.20 associated with the dimensionless factor f are attributed to the influence of the internal electric field. The first term indicates that the internal electric field lowers the direct piezoelectric polarization by a factor of f. The second term implies that the internal field induces additionally piezoelectric charge $-fQ_I$. In other words, it effectively lowers the trap charge by a factor of f. In the case of n-type ZnO, the trap charge is usually negative, thus the additional piezoelectric charge $-fQ_I$ tends to increase the piezoelectric charge. Since the factor f quadratically depends on the piezoelectric constant, this statement is valid for both the tail-to-tail and the head-to-head configuration. From Eq. 4.2.20 and 4.2.7, one obtains

$$\tilde{Q}_I = (1-f)(Q_I + 2\sigma e/Y). \tag{4.2.21}$$

Thus from Eq. 4.2.10 the potential at the GB can be expressed by external mechanical loading and bias voltage as:

$$\Phi_B = -\frac{qN_0}{2\epsilon_s}(1-f)\left(-\frac{Q_I + 2\sigma e/Y}{2qN_0} + \frac{1}{(1-f)}\frac{\epsilon_s V}{Q_I + 2\sigma e/Y}\right)^2. \tag{4.2.22}$$

For the case with no applied potential, i.e. $V = 0$, Eq. 4.2.22 is reduced to

$$\Phi_B = -\frac{(1-f)(Q_I + 2\sigma e/Y)^2}{8qN_0\epsilon_s}. \tag{4.2.23}$$

For the case with $V \neq 0$ but vanishing mechanical loading $\sigma = 0$, Eq. 4.2.22 becomes

$$\Phi_B = -\frac{qN_0}{2\epsilon_s}(1-f)\left(-\frac{Q_I}{2qN_0} + \frac{1}{(1-f)}\frac{\epsilon_s V}{Q_I}\right)^2. \tag{4.2.24}$$

If $f = 0$, Eq. 4.2.20 and Eq. 4.2.23 are reduced to,

$$Q_P = 2\sigma\frac{e}{Y}, \tag{4.2.25}$$

$$\Phi_B = \frac{(Q_I + 2\sigma e/Y)^2}{8\epsilon_s qN_0}, \tag{4.2.26}$$

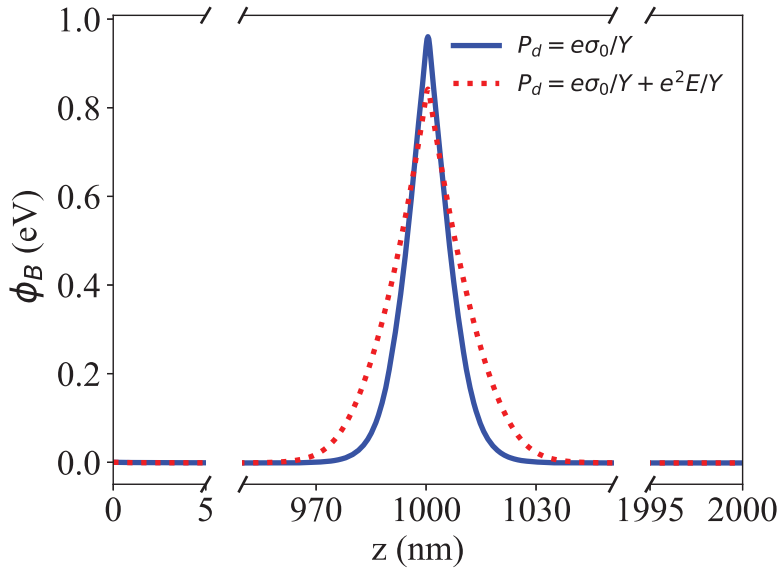

Figure 4.3: Comparison of the barrier height in a bicrystal without mechanical loading. The red dashed curve is for the case in which the internal electric field is considered, while the solid blue curve is for the instance in which the internal electric field is ignored.

which are the results of the models by Verghese and Clarke [37] and Baraki et al. [20].

4.3 Result and discussion

An energy barrier distribution with no bias voltage is calculated for the case with (red dashed line) and without (solid blue line) the impact of the inverse piezoelectric field. As Fig. 4.3 demonstrated, it is apparent that the barrier height (negative of the potential) declines due to the influence of the internal electric field.

The dimensionless factor f is non-trivial. Given the parameters of ZnO: $Y = 2.11 \times 10^{11}$ N/m^2, $e = 1.57$ C/m^2, and $\epsilon_s = 7.989{\times}10^{-11}$ F/m, the factor $f \approx 0.128$. The parameters are taken from Table 5.1. Thus from Eq. 4.2.23 we expect if Q_I is constant the GB barrier value obtained from our generalized model to be 87,2% of the result obtained by the model of Verghese and Clarke [37] and Baraki et al. [20]. In other words, the internal electric field can lower the barrier by 12.8%.

This effect is shown in Fig. 4.4. Though ZnO, in reality, can not bare immense stress as shown in Fig. 4.4 (the realistic stress range for ZnO is 250 MPa and is marked with grey), in order to demonstrate the effect of factor f more clearly, an extensive stress range from -1000 MPa to 1500 MPa is computed.

The barrier height pinning happens, as shown in Fig. 4.4 in the stress range of -200 MPa to 700 MPa. This pinning effect takes place when the trap states are not fully filled [37, 20], which will be demonstrated later. This effect also limits the internal electric field barrier lowering effect,

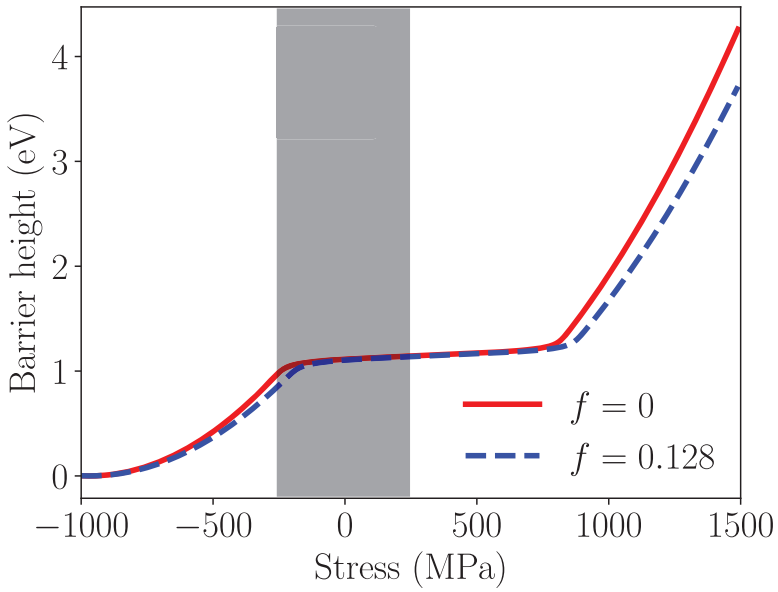

Figure 4.4: Barrier height comparison for the modified and traditional phenomenological model. The grey region denotes the realistic stress region. (The trap DOS is Delta function in this case.)

which is compensated by filling the electrons in the trap state. When the stress is outside this range, the trap states are either occupied (under compressive loading) or empty (under tensile loading), and the barrier height is reduced due to the internal electric field. It is observed more clearly from Fig. 4.5 that the barrier height is reduced for 12.8%, which is the value of factor f. The barrier height at the compressive stress of 1000 MPa drops to zero since due to the entire compensation by the trapped charge. It is worth to mention that the barrier height reduction can not be totally compensated by the electron filling. Fig. 4.5 shows that the reduction effect still exists in the pinning region, but reduces to less than 1%.

When the bias voltage V and the applied stress are taken into account simultaneously, the influence of the internal electric field becomes more complex. In the following, specific examples will be presented to demonstrate the impact of the internal electric field.

The barrier height of a head-to-head n-type ZnO bicrystal under compression is further investigated. Fig. 4.6 shows the variation of the barrier height with respect to the applied compression, calculated from Eq. 4.2.23. Note that the plateau region results from the self-consistent formulation of the trap charge by the density of state theory in relation to the barrier height Φ_B [37, 20] which is shown in Chapter 3.6.1 in Eq. 3.6.23 to 3.6.25 and the trap DOS in Eq. 3.6.26 to 3.6.28.

The corresponding parameters from Baraki et al. [20] and from Blatter and Greuter [34] are both applied, as listed in Table 4.1, where N_t is the effective trap density of states and $\mathscr{E}_I$ is the centre of the DOS distribution. The results on the impact of the inverse piezoelectric effect are

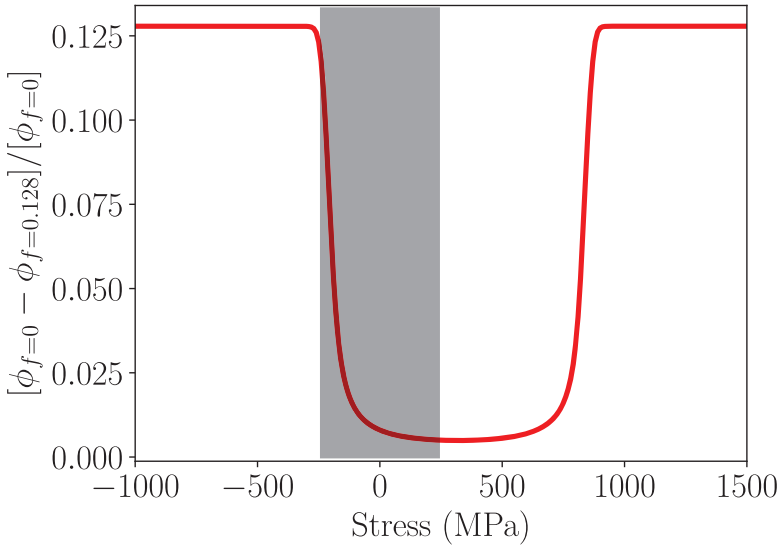

Figure 4.5: This figure demonstrates how much does the internal electric field influence the barrier height. The stresses from -200 MPa to 700 MPa are the range for a not fully occupied trap states. Outside this range, the non-modified and the modified barrier heights have a 12.8% difference, which is the value of factor f. The grey region denotes the realistic stress region.

Table 4.1: Parameters for density of states $\mathscr{D}(\mathscr{E})$

Parameters	Baraki et al. [20]	Blatter and Greuter [34]
T (K)	300	400
$\mathscr{E}_I$ (eV)	2.02	2.0
N_t (1/cm^2)	0.9e13	1.0e13
$\mathscr{E}_f$ (eV)	3.167	3.133
N_0 (1/cm^3)	1.13e18	1.0e18
A (A/cm^{2}K^2)	30	30

quite similar for both sets of parameters. For the following results, the parameters from Baraki et al. [20] are used. From Fig. 4.6, one can see the general tendency of the barrier height reduction with respect to the applied stress. The behavior can be explained by the fact that the piezoelectric charge is positive and tends to counteract the negative trap charge. With increasing compression, more trap charges are compensated, and thus the barrier decreases with increasing compression. A comparison between the curves for the case with ($f = 0.128$) and without ($f = 0$) the influence of the internal electric field shows two additional features. One is that the significant decrease of the barrier height occurs at a lower level of compression if the influence of the internal electric field is considered. The barrier height decreases considerably with increasing compressive stress already at the critical stress around 120 MPa for the case of $f = 0.128$ and around 220 MPa for

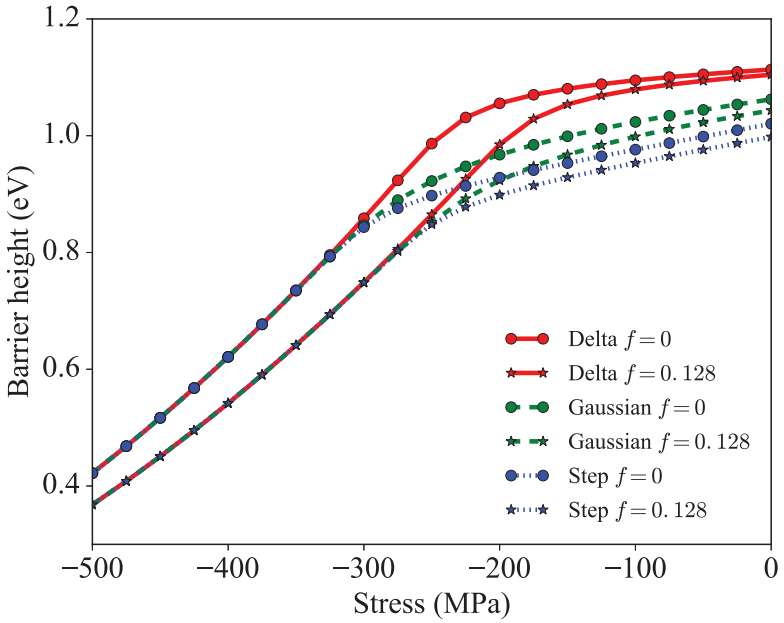

Figure 4.6: Barrier height variation against the applied stress under $V = 0$ V, for the case with ($f = 0.128$) and without ($f = 0$) the influence of internal electric field. Results are given for three distribution types of defect density of states.

the case $f = 0$. The other feature appears in the functional region beyond the drop of the barrier height. The slope of the barrier height curves in this region becomes smaller if the influence of the internal field is regarded. It implies that the internal field makes the barrier height less sensitive to the applied stress. The same features are observed for all three distribution types of defect density of states. In addition, the barrier height variation of the same head-to-head ZnO bicrystal under the applied bias potential is studied by using Eq. 4.2.24. Fig. 4.7 demonstrates that with increasing bias potential, the barrier height generally tends to be lowered correspondingly. The decrement of the barrier height by the internal electric field has also been well demonstrated for all three distributions of the defect density of states. Similar to what is observed with the application of stress, two additional features should be noted. One is that the prominent drop of voltage appears at much lower bias potential if the internal field is considered, i.e. $f = 0.128$. The other is in the functional region the slope of the curves with $f = 0.128$ is slightly smaller than that of the curves with $f = 0$. It indicates the decreased sensitivity of barrier height on the applied voltage.

To compare the effects of the three DOS, the integrated GB defect state densities N_t are set to be the same value for the three distributions. This guarantees that these three fully occupied DOS will have the same charge density. The characteristic decay energies are $\mathscr{E}^g_{Gau} = 0.15$ eV and $\mathscr{E}^g_{box} = 0.5$ eV. Combine Eq. 3.6.26,3.6.27,3.6.28 with Eq. 3.6.24 one can have the relation of trap charge density and barrier height, as shown in Fig. 4.8. The comparison of these DOS suggest that when the barrier height is below a certain value (0.8 eV for Gaussian and box DOS, 1.05 eV for

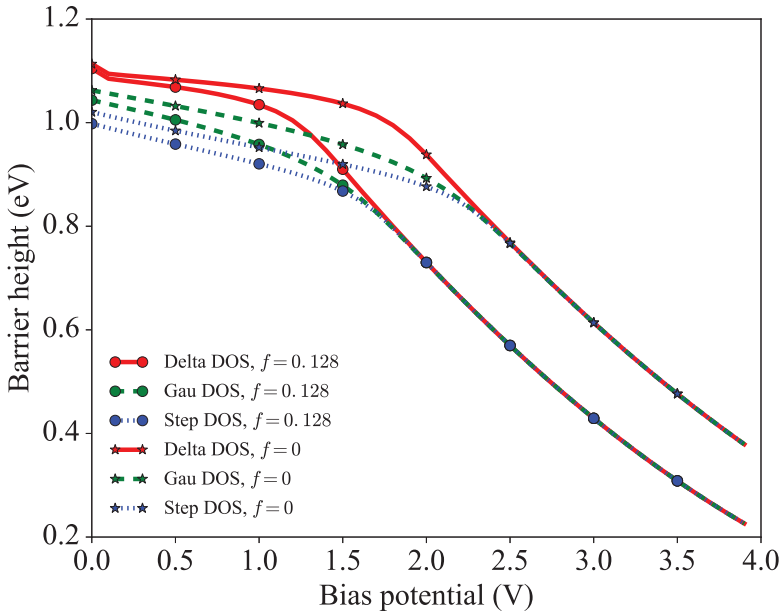

Figure 4.7: Barrier height variation against the applied voltage under $\sigma = 0$ MPa, for the case with ($f = 0.128$) and without ($f = 0$) the influence of internal electric field . Results are given for three distribution types of defect density of states.

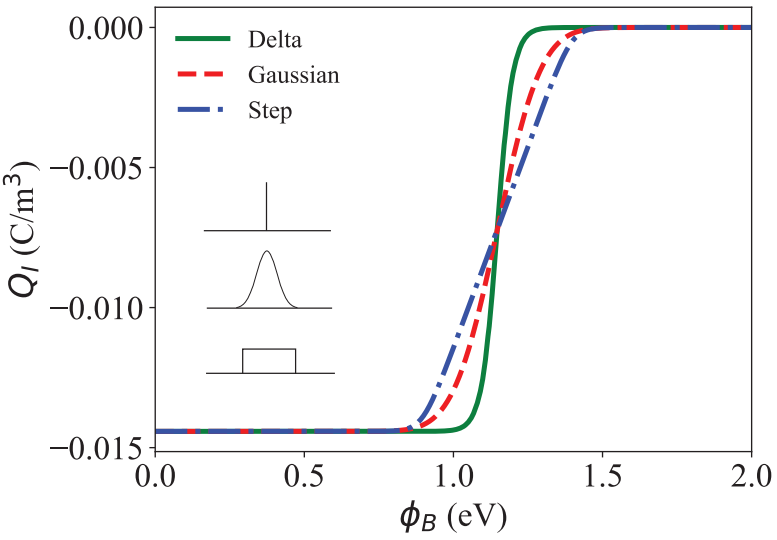

Figure 4.8: Delta, Gaussian and box shape of DOS inside the GB result in different reactions for the trap charges to the barrier height.

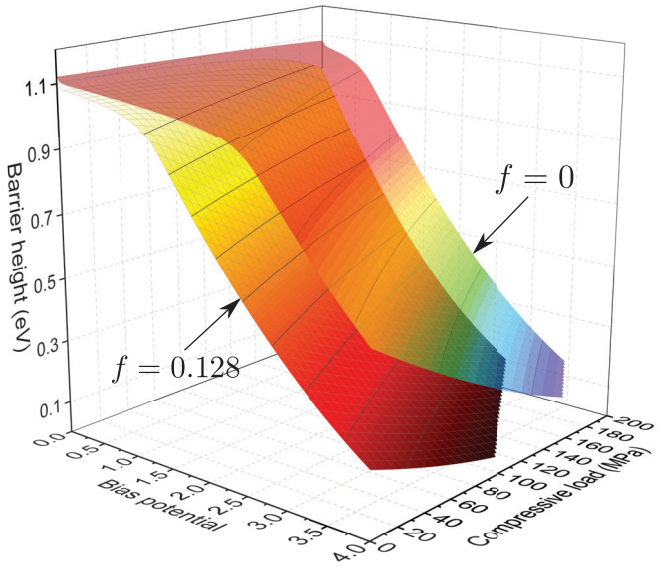

Figure 4.9: The demonstration of of the influence of the internal electric field with considering both bias potential and external loading. The calculation is studied with delta distribution of trap DOS.

Delta shape DOS), the trap states for all the three types of DOS are fully occupied whereas above a certain value (1.4 eV for Gaussian and box DOS, 1.15 eV for Delta shape DOS), the trap charges vanish. In between these two values, the trap states are partly occupied, and one can observe that the delta DOS have the sharpest slope and then follows Gaussian and box shape DOS.

As a consequence, in both stress variations in Fig. 4.6 and voltage variations in Fig. 4.7, the transition of the sudden drop of the barrier height is more prominent for a sharper slope DOS as shown in Fig. 4.8 than a smoother one. Also, one can notice that before the critical point in Fig. 4.6, 4.7, the barrier height for a narrower DOS is higher than a wider DOS. This is because there are more occupations for a narrower DOS under the same integrated GB trap state density.

After obtaining the barrier height and bias voltage, the current flowing through the bicrystal material can then be calculated in two parts. The electron current emitting over the barrier height $\Phi_B(V)$ is $AT^2 \exp\left(-\Phi_B(V)/kT\right)$ into the positive bias part, where A is Richardson constant. The second current which is flowing in the opposite direction is suppressed by the factor $\exp\left(-qV/kT\right)$. The combination of the two currents is determined as:

$$J(V) = A \cdot T^2 \cdot \exp\left(\frac{-\Phi_B(V)}{kT}\right) \cdot \left(1 - \exp\left(\frac{-qV}{kT}\right)\right). \tag{4.3.1}$$

It can be noticed that the flux reaches the maximum $A \cdot T^2$ when the barrier height is reduced to zero, and the bias voltage is relatively high. The calculated flux is shown in Fig. 4.10. The result illustrates that the larger external stress leads to higher flux. Since the internal electric field lowers the barrier height, the flux calculated from MPM is greater than from PM. As the

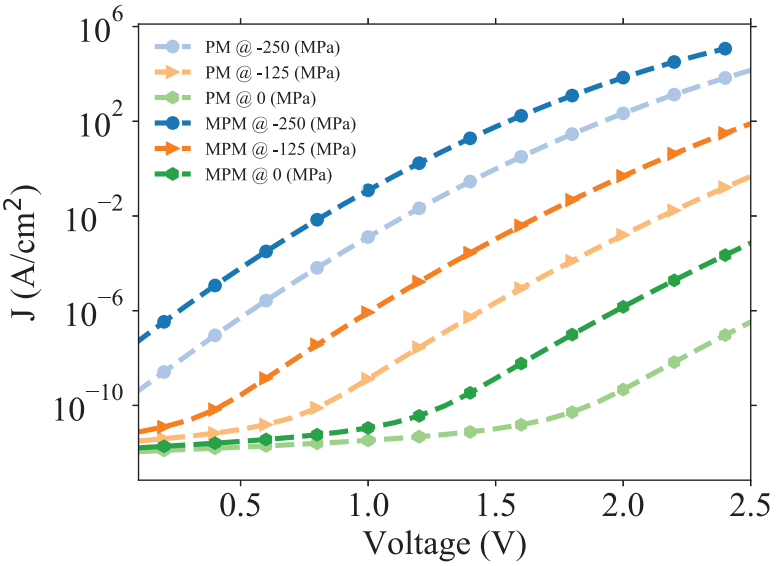

Figure 4.10: Flux comparison between PM and MPM. The MPM has a higher flux output due to the lower barrier height compare to PM

difference of the barrier height is reduced when the load increases, which are demonstrated in Fig. 4.9, the flux difference between the MPM and PM is reduced when increasing the loading. With the logarithmic y-axis, for the low-stress states, the flux stays at a low number then starts to increase dramatically. While for the high-stress states, the flux increases directly.

To summarise how the electrical property varies under different potential and external loadings, the complete relation of the bias potential, compressive load and barrier height is studied using Eq. 4.2.22. The result is plotted in Fig. 4.9. It is obviously seen that when increasing the external loading, the plateau region becomes smaller. Thus the breakdown happens at a lower bias potential. In this figure, it is also evident that at the same bias potential, the compressive loading lowers the barrier height. Another effect is that when increasing the compressive loading, the influence of the internal electric field becomes smaller. This is because, with a lower barrier height, the internal electric field is smaller. Since the flux is exponentially dependent on the barrier height (Eq. 4.3.1), a small variation of the barrier height results in a magnitude of change in flux. Hence, the internal electric field increases the flux significantly.

In conclusion, we signified the influence of the internal electric field on barrier height of the varistor like boundaries and therefore presented an extended phenomenological model of the barrier height Eq. 4.2.22. It is shown that the influence of the electric field can be characterized by a dimensionless coefficient f. The extended model is well reduced to the previous model [37, 20] if $f = 0$. Results show that the piezoelectric charge induced by the internal field tends to alter the GB charge and lowers the barrier height. If the extended model is implemented, the sensitivity of barrier height on the mechanical loading decreases while on the bias voltage, it does not. We believe that the inverse piezoelectric effect has a similar impact, independent of the model used

for the trap charge at the GB.

The previous models [37, 20] have been widely used to fit the experimental data of barrier heights with estimated parameters on GB charge densities. If our extended model is applied to fit the same experimental data, the determined GB trap charge densities are expected to be higher than those determined by the previous model. Moreover, the high gradient of the electric field near the GB may lead to an additional impact on the strain via the reverse flexoelectric effect, which can be an interesting topic in the future. Besides, The inverse piezoelectric effect can have a general impact on the III-V or II-VI semiconductor junction devices, e.g. the thin GaN films, AlGaN/AlN/GaN diodes, since they are also piezoelectric materials [87, 88]. Therefore, the results of this work are not only limited to potential barriers at GBs of ZnO but also have practical consequences on the study of other junction devices.

5 Finite element investigation of external loading influence on double Schottky barriers

As stated in the previous chapter, the PM or MPM need several assumptions. For example, the box shape charge distribution is only valid at 0 K; the potential at the left and right end of the box shape charge distribution is assumed zero; the GB width for MPM is assumed to be zero, which is not the case for a real bicrystal. These assumptions have a particular impact on the accuracy of the barrier calculation. For a more accurate prediction, the fully coupled electromechanical finite element model was developed in this work. Besides, FEM can expand to two or three dimensions, and more complicated geometries are supported. In particular, FEM can demonstrate more physical details, such as the distribution of different kinds of charge densities and polarisations.

5.1 Piezoelectric finite element model

A FE model is developed in which mechanics and electrostatics are coupled. To describe these two properties, the classical equations for force balance and electrostatics are implemented as governing equations:

$$\sigma_{ij,j} = 0, \tag{5.1.1}$$

$$D_{i,i} = \rho_f, \tag{5.1.2}$$

where σ_{ij} and D_i are the stress and electric displacement tensors respectively and ρ_f stands for free charge densities. For the 3D case, the Latin indices (i, j, k, m, n) run from 1 to 3 to define the three different directions in the Cartesian coordinate system. The comma in a subscript represents spatial differentiation, e.g. $\sigma_{ij,j} = \partial\sigma_{ij}/\partial x_j$. The Einstein summation convention is adopted for repeated indices.

In conventional piezoelectric theory, the constitutive equations are formulated as:

$$\sigma_{ij} = C_{ijkl}S_{kl} - e_{nij}E_n, \tag{5.1.3}$$

$$D_m = e_{mkl}S_{kl} + \varepsilon_{mn}E_n, \tag{5.1.4}$$

where C_{ijkl} is the stiffness tensor, S_{kl} is the strain tensor, e_{nij} is the piezoelectric tensor, and E_n is the electric field vector, D_m and ε_{mn} are the electric displacement and dielectric tensors, respectively.

The free charge density ρ_f in ZnO semiconductors consists of several components:

$$\rho_f = q(-n + p + N_D^+ - N_A^- - Q_I), \tag{5.1.5}$$

where n, p, N_D^+ and N_A^-, denote electrons, holes, ionized donors and ionized acceptors densities, respectively. These four kinds of charges distribute spatially in the grains, whereas the volume trap charge density Q_I is the integration of the occupied delta-shape DOS, which is confined inside the GB (taken as 1 nm thick) and vanishes in the grain interior. The charge densities can be expressed as:

$$n = N_C \exp(\frac{\mathscr{E}_f - \mathscr{E}_C + q\phi}{kT}), \tag{5.1.6}$$

$$p = N_V \exp(\frac{-\mathscr{E}_f + \mathscr{E}_V - q\phi}{kT}), \tag{5.1.7}$$

$$N_D^+ = Z_d N_d t_d, \tag{5.1.8}$$

$$N_A^- = Z_a N_a t_a, \tag{5.1.9}$$

$$Q_I = N_I \int_{\mathscr{E}_v}^{\mathscr{E}_c} f(\mathscr{E}, \phi)\delta\left(\mathscr{E} - \mathscr{E}_I\right) \mathrm{d}\mathscr{E}, \tag{5.1.10}$$

in which

$$t_d(\phi) = \frac{1}{1 + g_D \exp(\frac{\mathscr{E}_f + q\phi - \mathscr{E}_D}{kT})}, \tag{5.1.11}$$

$$t_a(\phi) = \frac{1}{1 + g_A \exp(\frac{\mathscr{E}_A - \mathscr{E}_f - q\phi}{kT})}. \tag{5.1.12}$$

In the above equations, ϕ is the electric potential. N_C, N_V are the effective density of states (effective DOS). $\mathscr{E}_C$ and $\mathscr{E}_V$ are the bottom of the conduction band and the top of the valence band energy. N_D^+ and N_A^- are the ionized donor and acceptors. $\mathscr{E}_A$ and $\mathscr{E}_D$ are acceptor and donor energy levels. Z_a and Z_d are the acceptor and donor valences. N_a is the acceptor impurity concentration. t_a and t_d are the fractions of ionized acceptors and donors. g_D and g_A are the ground-state degeneracy factors of donor and acceptor impurities, respectively. The trap charge

density Q_I takes the same form as defined in Eqs. (3.6.23-3.6.24).

As ZnO is a traditional n-type semiconductor, in order to fulfill the charge neutrality condition inside the grain, the approximation:

$$n \approx N_D^+, \tag{5.1.13}$$

is employed to calculate the Fermi level.

Table 5.1: Parameters used in the FE simulations.

Parameter	Value	Parameter	Value	Parameter	Value
C_{11} [1]	2.10×10^{11} N/m^2	e_{31}	-0.36 C/m^2	$\mathscr{E}_D$	3.19 eV
C_{12}	1.21×10^{11} N/m^2	e_{32}	-0.36 C/m^2	$\mathscr{E}_A$	0.15 eV
C_{13}	1.05×10^{11} N/m^2	e_{33}	1.57 C/m^2	z_d [2]	1
C_{21}	1.21×10^{11} N/m^2	e_{42}	-0.36 C/m^2	z_a	1
C_{22}	2.10×10^{11} N/m^2	e_{51}	-0.36 C/m^2	g_d	2
C_{23}	1.05×10^{11} N/m^2	ε	7.98×10^{-11} F/m	g_a	4
C_{31}	1.05×10^{11} N/m^2	q	1.60×10^{-19} C	N_C	2.25×10^{24} m^{-3}
C_{32}	1.05×10^{11} N/m^2	k_B	1.38×10^{-23} J/K	N_V	4.43×10^{24} m^{-3}
C_{33}	2.11×10^{11} N/m^2	T	300 K	N_d [3]	11.3×10^{23} m^{-3}
C_{44}	4.30×10^{10} N/m^2	$\mathscr{E}_F$	3.16 eV	N_a	0 m^{-3}
C_{55}	1.05×10^{11} N/m^2	$\mathscr{E}_C$ [4]	3.2 eV	$\mathscr{E}_I$	2.02 eV
C_{66}	4.45×10^{10} N/m^2	$\mathscr{E}_V$	0 eV	N_I [5]	9×10^{25} m^{-3}

The outlined piezoelectric model is numerically implemented using the finite element method in the academic software FEAP[91]. In the simulation, the first order shape function is applied due to memory saving and sufficient accuracy, and the degrees of freedom are potential and displacements which have three components indicating three directions. The parameters used in the simulation are listed in Table 5.1.

5.2 Head-to-head bicrystal under compression

The barrier height distribution for three different external compressive loads on a GB of head-to-head configuration is depicted in Fig. 5.1. For the purposes of computational efficiency and adequate physical interpretation resolutions, the dimensions and mesh size of the simulation object are as follows. Each grain is a bar shape of 1 nm × 1 nm × 1000 nm, and the GB has a

[1] From C_{11} to e_{51}, see ref. [89]

[2] From z_d to g_a, see ref. [70]

[3] From N_d to N_I, see ref. [90]

[4] From $\mathscr{E}_C$ to $\mathscr{E}_A$, see ref. [34]

[5] With the GB width of 1nm, N_I is the volume charge density converted from the surface charge N_t, which is 9×10^{16} m^{-2}.

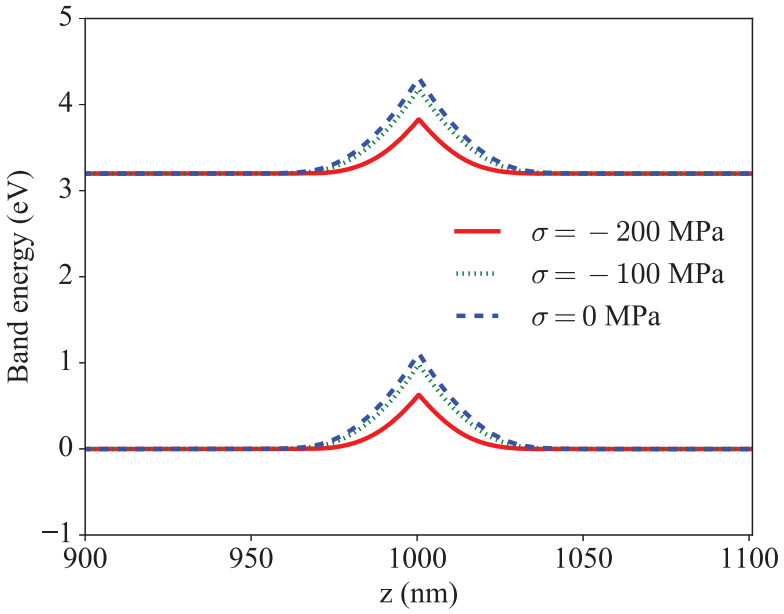

Figure 5.1: FE results for the band energy distribution under three compressive stress levels (head-to-head induced polarization)

width of 1 nm. Inside the grain, the FEM mesh size is set as 1 nm $\times$ 1 nm $\times$ 1 nm, whereas in the GB the size is 1 nm $\times$ 1 nm $\times$ 0.25 nm in order to increase the resolution within the GB in the [0001] direction.

Compressive loading is imposed by traction boundary conditions on the left and right ends of the sample, as shown in Fig. 5.3, and the values vary between 0 and -250 MPa. As for the potential, the Dirichlet boundary condition is implemented on the two ends of the sample. Specifically,

$$\sigma(z)\big|_{z=-z_l} = \sigma_0, \tag{5.2.1}$$

$$\sigma(z)\big|_{z=z_r} = \sigma_0, \tag{5.2.2}$$

$$\phi\big|_{z=-z_l} = 0, \tag{5.2.3}$$

$$\phi\big|_{z=z_r} = 0, \tag{5.2.4}$$

where $-z_l$ and z_r are the coordinate of the left and right boundaries of the simulated sample, respectively, as shown in Fig.5.3. For the other four surfaces, both the potential and displacements have Neumann boundary conditions, and the gradient is zero. Having no mechanical constraint means that these surfaces are free to move.

Fig. 5.1 depicts FE results for the band energy distribution for the external loading σ_0 = 0, -100 MPa, -200 MPa. The barrier height falls with increasing compressive stress due to the increased piezoelectric polarization. The reason for this is that, for the head-to-head configuration, the polarization charge is positive at the GB and increases with the magnitude of the compressive loading. Thus it compensates the negative trap charges at the GB and reduces the barrier height.

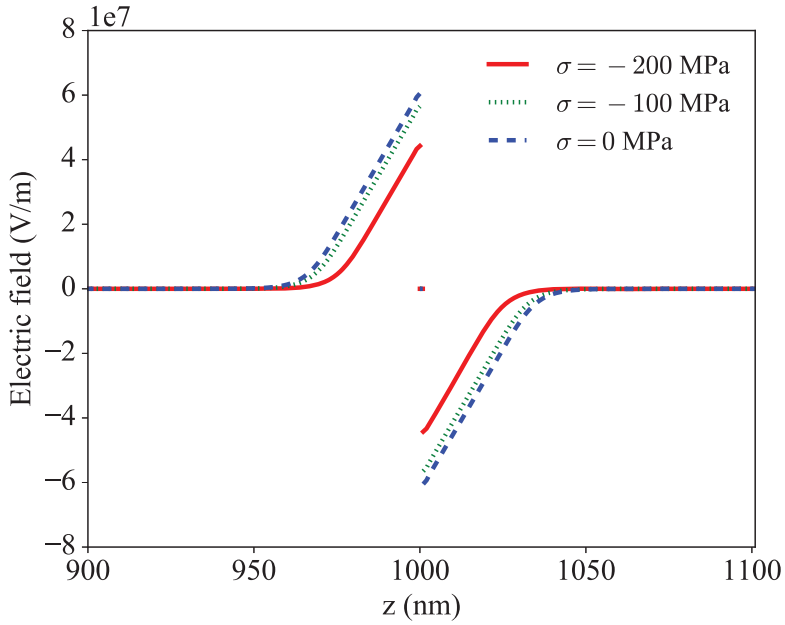

Figure 5.2: FE results for the electric field distribution in the depletion layer.

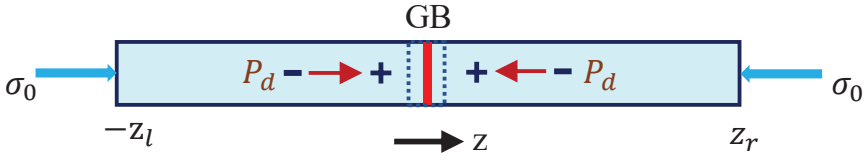

Figure 5.3: Configuration of the bicrystal. The external loadings are applied on the left and right end $-z_l$ and z_r.

In the depletion region, the band energy or the potential has a second-order dependency with respect to space. Therefore, the electric field shows a linear progression with distance from the boundary, as demonstrated in Fig. 5.2. The reduction in the internal electric field with increasing applied compression is due to the lowering of the barrier height.

In this paper, it is assumed that the dopants and charges are distributed homogeneously. From the charge densities in Table. 5.1, it is estimated that, in the depletion region, the average distance between each donor is 9.6 nm. For trap charges, the value is 2.23 nm, and for electrons, the value is 7.63 nm. Fig. 5.8 shows that the length of the depletion region is around 100 nm. Since the FEM resolves nanometer scale, it must be noted that, in reality, the band energy and electric field, as shown in Fig. 5.1 and Fig. 5.2, are not as continuous as in these two figures. Nevertheless, we treat these quantities as continuous and smooth, since it is sufficient to capture the behavior of the electrons and holes in the depletion region such that varistor behavior is depicted.

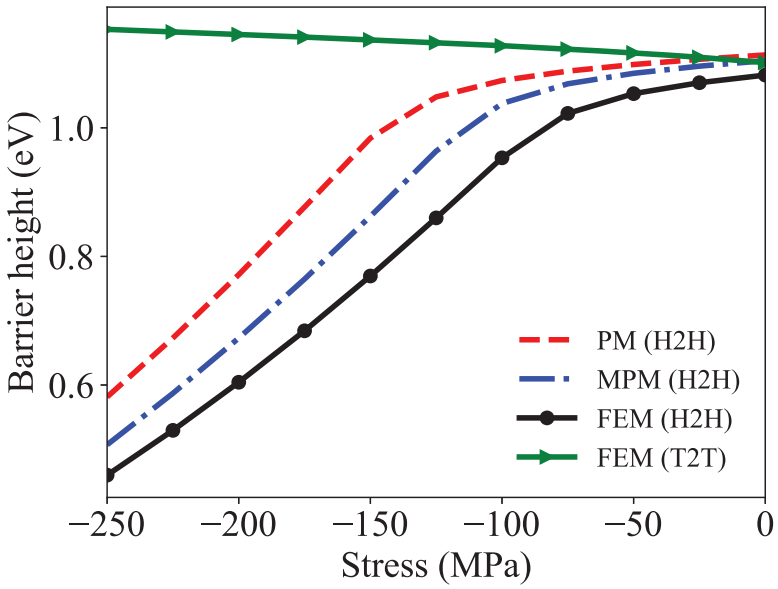

Figure 5.4: Barrier height calculation from FEM, MPM.

5.3 FEM results and comparisons with PM and MPM

The bar shape FE simulation considers the influence of anisotropy in all directions. Hence, for a higher accuracy, the MPM could also take this effect into account. In the calculation, the bold symbol denotes the matrix form of the physical quantities, and the superscript T signifies the transpose of the matrix. In Fig. 5.4, the variation of the GB barrier height with respect to the applied compressive stress is shown. The solid black line and blue dashed line describe the FEM and MPM results, respectively. The three curves show a general decrease of barrier height with the applied compressive stress.

For the head-to-head configuration illustrated in Fig. 5.4, both the FE and MPM are conducted self-consistently, and produces similar curves. It is evident that the barrier height from the MPM is lower than the one from the PM due to the internal electric field. Last but not least, it can be observed that the barrier height obtained from the FE piezoelectric model is lower than the one from the MPM, the reasons for which will be shown later. For the tail-to-tail instance in Fig. 5.4, increasing the compressive stress leads to a gradual increase in the barrier height, which is correlated with the strong pinning of the potential barrier. In this case, negative polarization charges are induced however, a drastic increase in barrier height is prevented by electrons leaving the interface while their energies are above the interface Fermi-level.

5.4 Differences between FEM and MPM

One big difference between the MPM and the FEM is the assumptions made when calculating ϕ. In the MPM for the ϕ boundary conditions, we assume $\phi(-z_l) = 0$ and $\phi(z_r) = 0$, where the $-z_l$ and z_r are the edge of the assumed charge distribution which is defined in Fig. 4.2. In the FEM, the boundary conditions for ϕ are only set at the crystal end. In fact, the positions where $\phi = 0$ and $N_d = 0$ are quite close to each other, but not the same.

Another difference is that the FE model is implemented for $T = 300$ K, which generates a trapezoidal shape of ionized donor distribution, as suggested in Fig 5.5. The FEM at $T = 0$ K is not calculated since, at this temperature, ZnO is non-degenerate. For the MPM a box-like ionization of donor distribution is assumed, which represents the case of $T = 0$ K. It is easy to calculate the analytical solution for a box-shaped ionization donor, and it does not sacrifice too much accuracy. However, it is one of the reasons that these two models do not produce the same result. In Fig. 5.5, the amount of charges is almost the same for both models if one integrates the areas enclosed by the distribution shape and the z-axis. For the FE model, the space charge region extends further in a smooth curve. Thus, due to different temperatures, the trapezoidal charge distribution produces a lower barrier height in comparison to a box-shape charge distribution.

It is also worth noting that the GB width is 1 nm for the FEM and 0 nm for the MPM. In Fig. 5.6 the influence of the GB width on the barrier height is studied. While altering the width, the number of trap charges remains the same. Thus $Q_I \cdot l \cdot A = Q_I^0 \cdot l^0 \cdot A$, where Q_I and l are the trap charge density and GB width, the superscript '0' denotes a datum value, and 'A' is the flat area of the GB. It is observed that a thinner GB width leads to a higher barrier height. The thin GB is also one of the reasons that the barrier height from the MPM is higher than the one from the FEM. Nevertheless, the MPM provides quick access to the barrier height and is convenient to apply.

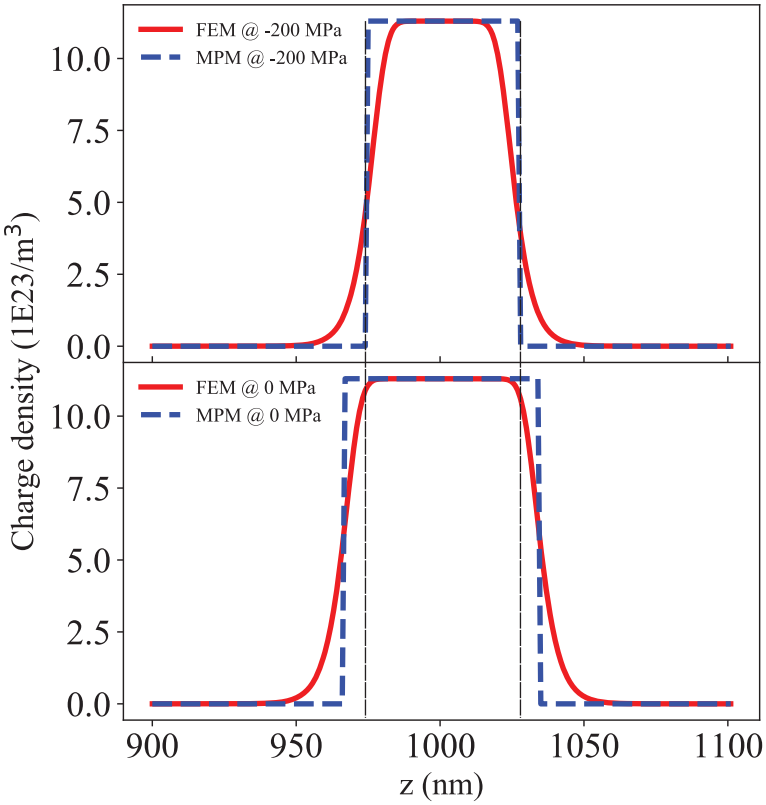

Figure 5.5: Comparison of ionized donor density distributions which diverge from one another for FEM and MPM. By increasing external loading, the width of both models shrinks due to the reduced barrier height.

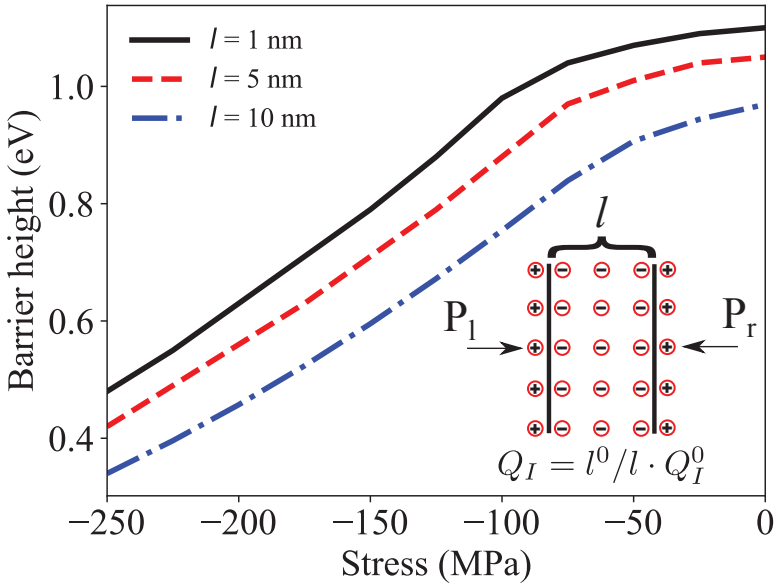

Figure 5.6: The influence of the GB width on the barrier height under different compressive loading.

5.5 Self consistency between the trap charge density and the barrier height

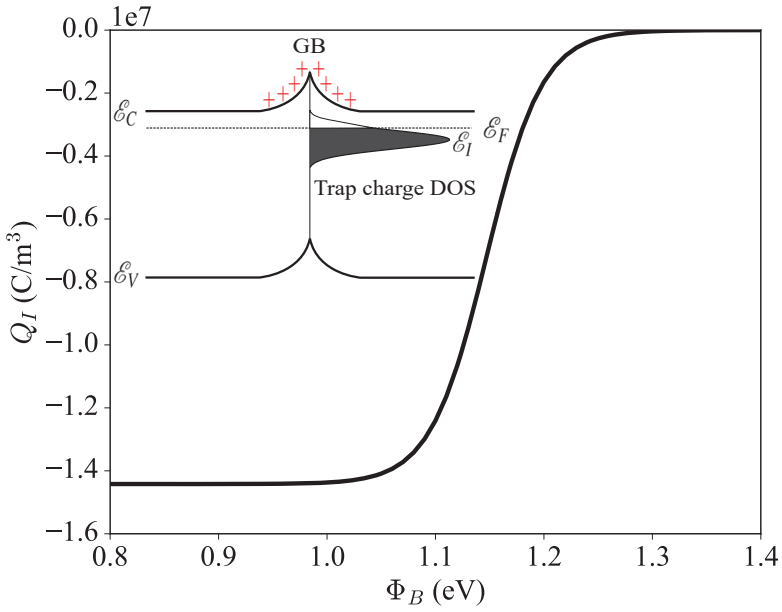

Figure 5.7: Trap charge density variation with barrier height. For visualisation purposes, the trap charge DOS is illustrated with a width rather than the delta function used in this paper.

The higher barrier height observed at low-stress levels in Fig. 5.4 correlates to the highly non-linear current-voltage behavior illustrated in Fig. 5.7 [35, 34, 19]. When applying compressive stress (induction of positive polarization charges) or voltage to a ZnO-bicrystal, as shown in Fig. 4.2, the barrier height decreases and the energy level of the states at the GB $\mathscr{E}_I$, which is pinned to $\mathscr{E}_V$, is shifted to lower energies. This decrease in $\mathscr{E}_I$ leads to more free trap states moving below the Fermi-Level and, subsequently, more electrons trapped inside the GB, which compensates for the drop in the barrier height. Once the barrier height is low enough that the DOS is fully occupied, there are no more states in the trap DOS to be filled with new electrons. Thus, the barrier height begins to shrink drastically.

Once the trap charge density increases to maximum due to high stress, all the trap states at the interface are occupied. For greater applied stresses, the barrier height depends only on the induced polarization charge (Eq. (4.2.23)).

Fig. 5.8a illustrates the charge density distribution of electrons, holes, ionized donors, and ionized acceptors at zero stress. The summation of these four charges is depicted in Fig. 5.8b by the solid red line. Additionally, the piezoelectric charge and trap charge at the GB is also illustrated. It should be noted that far away from the GB, the net charge density complies with the charge neutrality rule, whereas near the GB, in the depletion area, the net charge is positive.

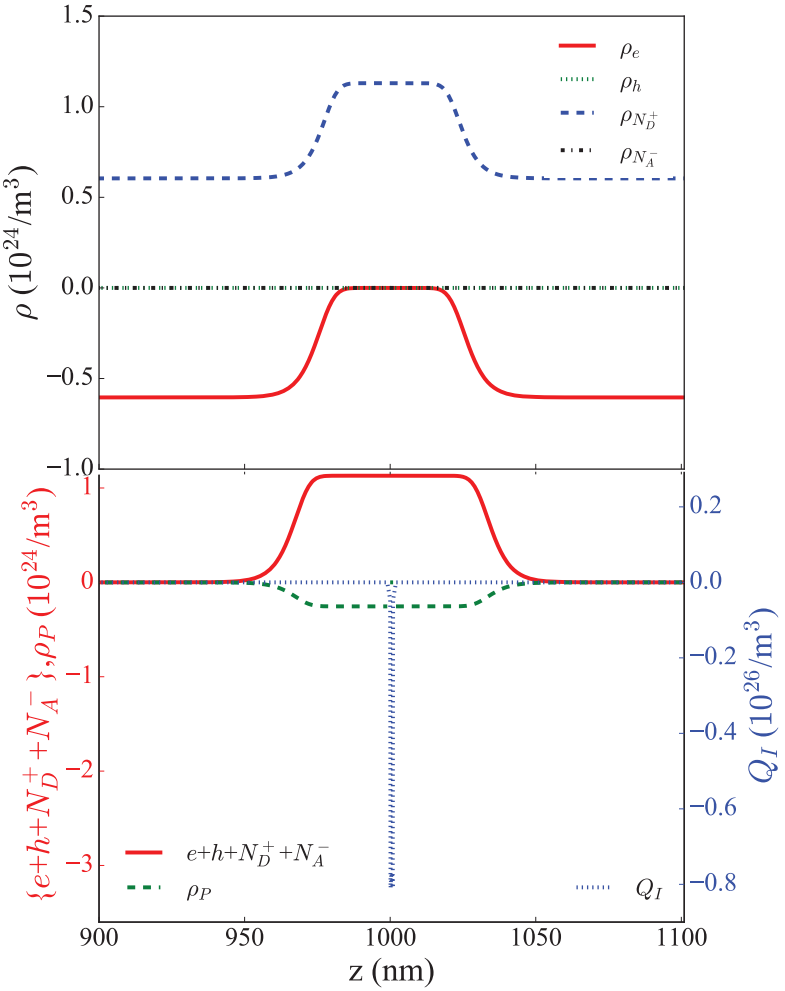

Figure 5.8: Charge density distribution for zero external loading. (a) Charge density distribution of ionized donors and acceptors, electrons and holes. (b) Distribution of all charge densities, the solid red curve is the summation of charge densities in (a).

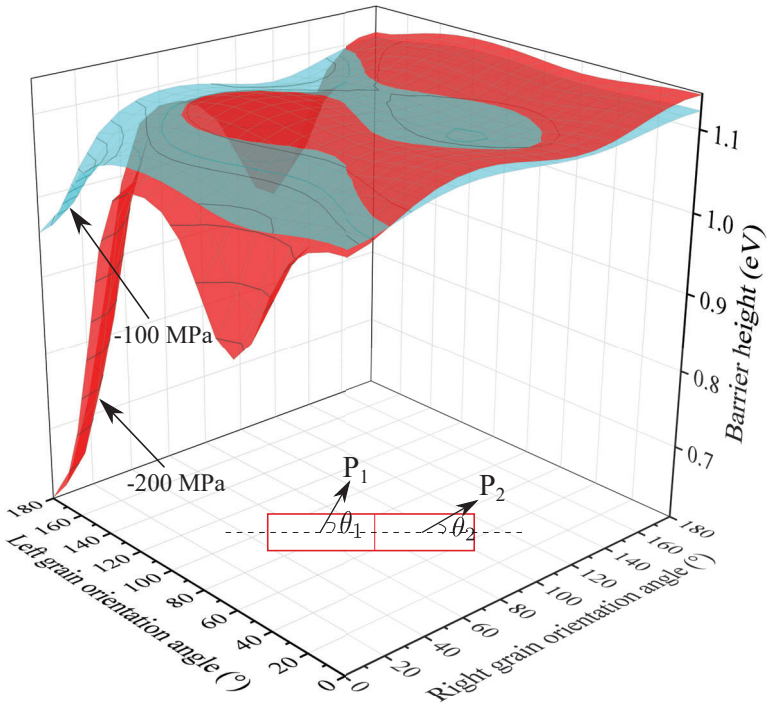

Figure 5.9: 3D illustration of the barrier height for different crystallographic orientations and external loading conditions. -200 MPa and -100 MPa are shown exemplarily.

According to the Poisson equation $\nabla E = \rho/\varepsilon$, positive net charge leads to a positive electric field slope. Since the net charge is positive in most parts of the depletion region, the electric field has a positive slope, as illustrated in Fig. 5.2.

Fig. 5.8a shows a trapezoid distribution of ionized donors and electrons. The donors are fully ionized around 1000 nm and gradually decrease to a constant value, because the ionization is determined by $\mathscr{E}_f + q\phi - \mathscr{E}_D$ as shown in Eq. 5.1.11. When ϕ is zero, the amount of ionization is constant, as shown outside of the depletion region. Close to the GB, ϕ slowly decreases (as the barrier height increases), while the amount of ionized donors grows until it reaches a saturation point (flat region of the trapeze). The same mechanism applies to electron densities. The profile of ionized donors and electrons together forms a trapezoidal space charge distribution. As for the MFM, since it is calculated at T=0 K, the Fermi-Dirac distribution becomes a standard step, which suggests that below the Fermi energy the states are 100% occupied, while above it the occupation is 0%. This occupation divided by Fermi energy leads to a step ionized donor distribution for the MPM.

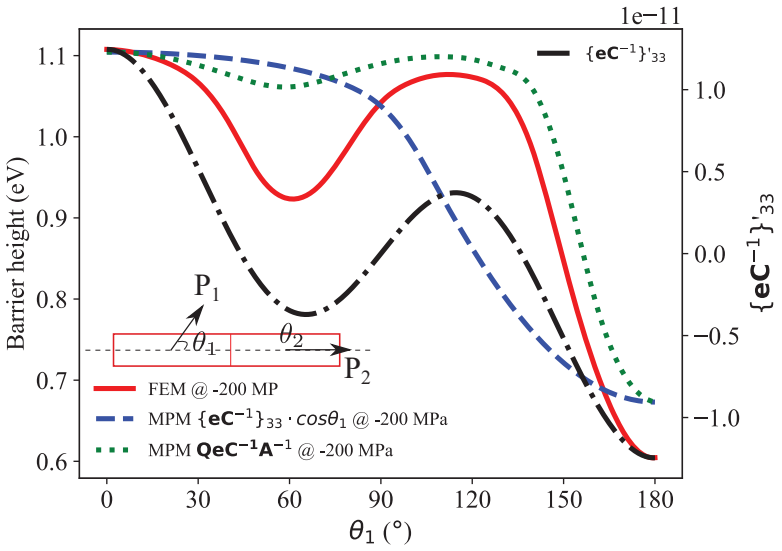

Figure 5.10: Barrier height dependence on grain orientation. The orientation for the right part of the bicrystal stays $0°$ while the left grain rotates anticlockwise from the vertical axis from $0°$ to $180°$. $\{\mathbf{eC}^{-1}\}_{33}$ as the coefficient of σ is also illustrated.

5.6 Dependence of barrier height on grain orientation

In a polycrystal, the orientation of every single crystal is random. Assuming the same DOS exists at the interfaces, the dependence of the barrier height on applied mechanical stress is different for various angles from the head-to-head to the tail-to-tail configuration. In this section, different crystal orientations and stresses are considered in the bicrystal system, and the barrier heights are calculated with FEM. These barrier heights can be used as a data set for each GB in the polycrystalline system. Using this data set, much higher accuracies can be obtained. Note, again, that we assume no change in the trap DOS for the simulation. In real crystals, the situation is more complex as the different orientation of the connecting crystals may also lead to a difference in trap states.

As depicted in Fig. 5.9, it is defined in the paper that the directions of P_1 and P_2 are the direction of [0001] for each crystal. P_1 and P_2 rotate in the plane and when θ_1 and θ_2 increases, the crystals rotates anti-clockwise along the [1000] direction.

The results for different stress states are presented in Fig. 5.9. It is clear that except for the global minimum at $\theta_1 = 180°$ and $\theta_2 = 0°$ (head-to-head), a second local minimum occurs at $\theta_1 = 60°$ and $\theta_2 = 0°$ (or $\theta_2 = 60°$ and $\theta_1 = 0°$). It is worthy of mention that when no external loading is applied to the bicrystal, for different grain orientations, the barrier height varies from 1.09 eV to 1.11 eV, which results in a relatively flat surface.

Consider the example that the configuration where only the left grain rotates and the right grain stays at $0°$, as shown in Fig. 5.10. Since MPM is calculated for one dimensional, how to

integrate the anisotropy into calculation becomes a problem. For the bicrystal, one can simplify the Q_P calculation as $Q_P = P_1 \cos\theta_1 - P_2 \cos\theta_2$, where the θ_1 and θ_2 range from 0 to π. The Q_P expression implies the polarization charge is the projection of the polarization onto the GB normal. When the θ_2 is fixed at zero, the right grain contributes positive polarization charge to the GB, if compressive stress is applied. Meanwhile, when θ_1 is between $0°$ and $90°$, the left grain provides negative charge to the GB and from $90°$ to $180°$ positive charge is supplied. When θ_1 increases, there is more positive polarization charge at the GB thus, the barrier height is lowered, as the blue dashed line shows in Fig. 5.10. While this simplification is intuitive, the barrier height from the FEM shows a different trend.

As the solid red curve in Fig. 5.10 shows, the barrier height first drops to a local minimum at $60°$ and then rises again at 120°. After that, the barrier height drops again abruptly to the minimum at $180°$. The black dash-dotted line is illustrated to demonstrate why the result from the FEM behaves so differently. This line is the element of the third column and third row in the matrix $\mathbf{Q}\mathbf{e}\mathbf{C}^{-1}\mathbf{A}^{-1}$, which is the matrix $\mathbf{e}\mathbf{C}^{-1}$ rotated by an angle of θ_1. $\mathbf{Q}$ is the traditional rotation matrix and $\mathbf{A}$ is the matrix that rotates $\boldsymbol{\sigma}$ in Voigt notation. Details are given in the appendix 9.1.

In this manner, the anisotropy takes effect. This means that when the crystal is rotated, every element in the $\mathbf{e}\mathbf{C}^{-1}$ matrix takes part in the calculation of $\{\mathbf{e}\mathbf{C}^{-1}\}'_{33}$, where $\{\mathbf{e}\mathbf{C}^{-1}\}'$ is the rotation of $\mathbf{e}\mathbf{C}^{-1}$. The $\{\mathbf{e}\mathbf{C}^{-1}\}'_{33}$ is positive when $\theta_1 < 45°$ or $90° < \theta_1 < 135°$. All other angles are negative. When $\{\mathbf{e}\mathbf{C}^{-1}\}'_{33}$ is positive, the direct piezoelectric part $\{\mathbf{e}\mathbf{C}^{-1}\}'_{33}\sigma_3$ is negative since σ_3 is -200 MPa. Neglecting the inverse piezoelectric effect, this indicates that the left grain induces negative charge at the GB. Vice versa, $\{\mathbf{e}\mathbf{C}^{-1}\}'_{33}\sigma_3$ is positive when $\{\mathbf{e}\mathbf{C}^{-1}\}'_{33}$ is negative, hence positive charge at the GB contributes to the reduction of the barrier height. Thus, the barrier height trend follows $\{\mathbf{e}\mathbf{C}^{-1}\}'_{33}$.

If the $\{\mathbf{e}\mathbf{C}^{-1}\}'_{33}$ is implemented in the MPM, the green dotted line is obtained. It can be observed that it shows a similar trend to the FEM result, though not as intense. The anisotropy effect for FEM is stronger than MPM since in FEM the shear stresses and the electric field such as E_x and E_y are taken into account, while for MPM these numbers are not achievable.

These comparisons indicate that neglecting the anisotropy in the $\mathbf{e}\mathbf{C}^{-1}$ matrix leads to inaccurate calculation of barrier height. Rotating the full matrix $\mathbf{e}\mathbf{C}^{-1}$ is necessary when calculating the MPM. In large scale calculations, e.g., polycrystalline cases, the orientation of the crystal is complicated and has a true influence on the accuracy of the prediction of barrier height. In this case, the anisotropy should be taken into account by using the barrier height data from the FEM.

This data set can be employed for the large scale network simulation of polycrystals, in order to investigate the impact of the internal electric field on the mesoscopic electric and piezoresistive properties.

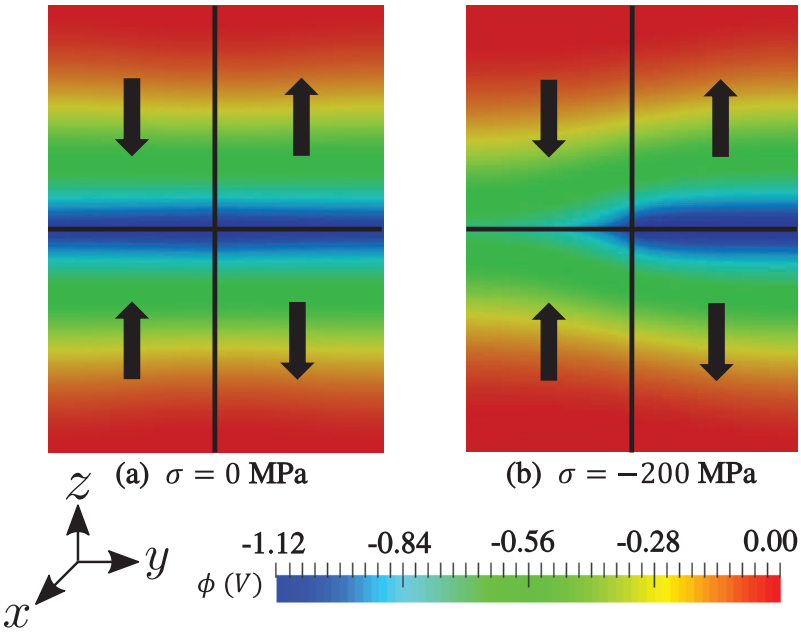

Figure 5.11: FE results for the electric potential distribution for a four-grain configuration with tail-to-tail and head-to-head GBs.

5.7 Four-grain configuration

The microscopic FE model with spatially resolved GBs covers not only the impact of the internal electric field self-consistently, but also allows access to the inhomogeneity of the barrier height along the GB. In this section, a thin film containing four perfect grains, as depicted in Fig. 5.11 is simulated. Here both head-to-head and tail-to-tail GBs are presented.

The dimensions of the four-grain sample are 50 nm in the y-direction and 2000 nm in the z-direction. The contour plot, Fig. 5.11, compares the potential distribution in the sample without loading and with a compressive loading of 200 MPa. With no external loading, the potential from the two models is evenly distributed at around -1.1 V, as demonstrated in Fig. 5.12. Under 200 MPa of compressive stress, the results change considerably as shown in Fig. 5.12. Since the compressive stress reduces the negative piezoelectric charge for the head-to-head configuration at the GB, but increases the negative piezoelectric charge for the tail-to-tail configuration, the potential from the two models rises on the left-hand side and decreases on the right. It can be recognized that for the head-to-head GB, the potential height decreases significantly, while for the tail-to-tail GB it hardly varies at all with the mechanical loading. The potential varies significantly from the head-to-head to the tail-to-tail GB. Hence, the inhomogeneity of the barrier height across the GB junction becomes apparent. The MPM yields a barrier height which is higher than the FEM result along the GB. However, since the MPM is a 1D model, the barrier height is a single dot which is expanded to a line or plane in 2D or 3D cases. Hence it is incapable of exhibiting the homogeneity. We expect that a different potential distribution would have an impact on the

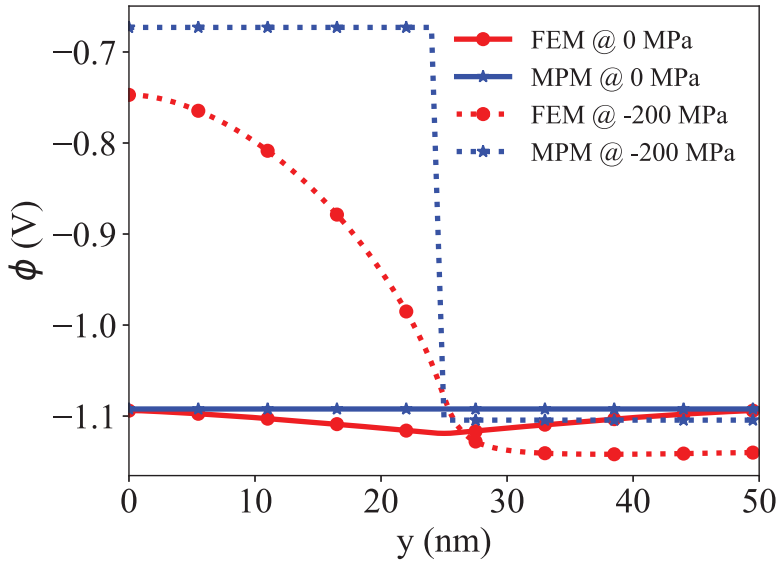

Figure 5.12: Potential distribution along the horizontal GB for a four-grain configuration. The results of the MPM are obtained from a 1D configuration and extended to 2D by extending a single point to a line along the GB.

calculation of the effective current passing area (the area in which the barrier height is low enough that the current prefers to pass through there than at other higher barrier height areas). This inhomogeneity naturally impacts the current-voltage behavior.

Even though this geometry is an ideal case and in real situations usually a triple junction exists rather than a quadruple one, it can demonstrate the capability of the FEM in dealing with inhomogeneous GBs. In contrast, the MPM does not represent this simple case physically.

In the future, more realistic multigrain configurations can be simulated using the FEM, such as honeycomb grain shapes, controlled GB orientation, and various GB junctions.

5.8 Conclusion

The constitutive equations of the FEM cover the coupling of the mechanical and electrostatic effects. In this way, multiple aspects are included, which are neglected in phenomenological models to describe potential barriers at ZnO-ZnO interfaces. For example, the inverse piezoelectric effect of the internal electric field on the barrier height is automatically taken into account. For a bicrystal, since the electric field always points in the direction of the GB, it increases the amount of positive charge at the GB, as indicated by Eq. 4.2.20. Therefore, considering the internal electric field leads to a reduction in the barrier height, which is well demonstrated in Fig. 5.4. The reason that the results from the FEM and the MPM are different stems from three main points. Firstly, at $T = 300$ K, the ionized donor states from FEM results show a trapezoidal shape rather than a box shape as assumed in the MPM at $T = 0$ K. Secondly, in the FEM, there are no

additional assumptions for the potential at the edge of the depletion region. Thirdly, the width of the GB for the FEM is 1 nm rather than 0 nm assumed by the MPM. For these reasons, the FEM is physically more meaningful. Crystallographic orientation and external loading for a bicrystal are also investigated in this work. The FEM results show a significant difference in the variation of the barrier height with mechanical stress in comparison to traditional phenomenological models. This difference can be explained by $\{\mathbf{e}\mathbf{C}^{-1}\}'_{33}$, the variation in which, when anisotropy is taken into account, is not monotonic. Rather than a smooth decrement, the barrier height firstly drops to a local minimum at $\theta_1 = 60°$, before returning to a local maximum at $\theta_1 = 120°$. After that, a sudden drop occurs. After considering the effect of anisotropy in the MPM, a similar result close to that of the FEM is produced. However, the effect is not extensive in the MPM, which suggests that when the configuration is complicated, the anisotropy needs to be considered for the piezoelectric parameters. Though the four-grain simulation is an ideal case, it still indicates that the spatial resolution of the FEM can resolve nanometer scales, and the barrier height along the GBs is not homogeneously distributed. This is due to to the high spatial resolution in all dimensions of the FEM. It is worthy of mention that though the FEM can provide resolution in the nanometer scale, the charge densities applied in this paper result in average distances between the charges of several nanometers. Subsequently, in reality, the band energy and charge density distributions are not continuous. Nevertheless, the continuous illustration in this paper can well interpret the influence of these physical quantities on the properties of the material, and guide the physical behavior of the sample.

6 Piezoelectric varistor finite element model

The response of the GB barrier height to the external loading has been demonstrated in chapter 5. In this chapter, the model will be further developed to include the effect of bias voltage. In this way, both the mechanical and electrical properties are considered.

Even though the former FEM barrier height simulations are efficient and provide useful information such as the charge densities and potential profile, the varistor behaviour under bias voltage and particularly the I-V curves should also be examined. Especially, what happens exactly to the band energy and the charge density profile before and after the breakdown can not be physically illustrated by the MPM or the FE model shown in the last chapter. Therefore, this chapter is individually opened.

6.1 Theory of the quasi-Fermi energy and its influences on the flux calculation

For the current-voltage calculation of the bicrystal with one GB, in this chapter, two assumptions are made for the current-voltage calculations: (1) the charge inside the grain bulk is neutral, which can be used to calculate the Fermi level; (2) the semiconductor is assumed to be non-degenerate. Hence Eq.3.4.5 is applied due to a much more straightforward calculation than the Fermi-Dirac integral. Therefore, considering the Boltzmann statistics and the electric potential, we have:

$$F_{1/2}\left(\frac{\mathscr{E}_F-\mathscr{E}_C-q\phi}{kT}\right)\approx\frac{\sqrt{\pi}}{2}\exp\left(-\frac{\mathscr{E}_C-\mathscr{E}_F+q\phi}{kT}\right). \tag{6.1.1}$$

It needs to be noted that since the energy for the band energies usually have the unit as eV and ϕ has the unit V, q in the equation have the value of -1. In the above equation, the approximation is very accurate when the semiconductor is nondegenerate. Hence the calculation in the equilibrium

states for electrons and holes are:

$$n = n_i \exp\left(\frac{\mathscr{E}_F - \mathscr{E}_i - q\phi}{kT}\right), \tag{6.1.2}$$

$$p = n_i \exp\left(\frac{\mathscr{E}_i - \mathscr{E}_F + q\phi}{kT}\right), \tag{6.1.3}$$

in which n_i is intrinsic carrier concentration and $\mathscr{E}_i$ is the intrinsic Fermi level. The two equations are identical to Eq. 3.4.5 and Eq. 3.4.6, since n_i:

$$n_i = N_C \exp\left(-\frac{\mathscr{E}_C - \mathscr{E}_i}{kT}\right) = N_V \exp\left(-\frac{\mathscr{E}_i - \mathscr{E}_V}{kT}\right) \tag{6.1.4}$$

In the equilibrium state, one can notice from Eq. 6.1.2 and 6.1.3 that the product of electrons and holes is fixed to n_i^2. However, in the non-equilibrium state, the balance is broken since the density of the minority carriers are changed. Consequently, the product is not equal to n_i^2 anymore. Hence, we define quasi-Fermi energies for electrons $\mathscr{E}_{fn}$, for holes $\mathscr{E}_{fp}$ so the calculation of electrons and holes can be determined:

$$n = N_C \exp\left(\frac{\mathscr{E}_{Fn} - \mathscr{E}_C - q\phi}{kT}\right), \tag{6.1.5}$$

$$p = N_V \exp\left(\frac{-\mathscr{E}_{Fp} + \mathscr{E}_V + q\phi}{kT}\right), \tag{6.1.6}$$

Then, the off-balance charge densities are determined by $\mathscr{E}_{Fn} - \mathscr{E}_{Fp}$.

Many aspects can influence the electric current: drift by the electric field, diffusion, thermionic drift, recombination, and tunneling. In this work, the drift caused by the electric field, diffusion caused by the carrier concentration gradient and recombination are considered. Traditionally the flux is arisen by drift and diffusion as demonstrated by Eq. 6.1.7. However, it can also be converted to the function of quasi-Fermi energy:

$$J_n = q\mu_n nE + \mu_n kT\nabla n \tag{6.1.7}$$

$$= q\mu_n n(-\nabla\phi) + \mu_n kTn\left(\nabla\mathscr{E}_{Fn} + q\nabla\phi\right)/(kT) \tag{6.1.8}$$

$$= \mu_n n\nabla\mathscr{E}_{Fn}, \tag{6.1.9}$$

where J_n is electron flux (A/m^2) and μ_n is drift mobility ($m^2/V \cdot s$). Therefore, the drift and diffusion have been merged into one term, and the flux is controlled by the density of electrons and gradient of $\mathscr{E}_{Fn}$.

In the FE calculation in this chapter, the potential ϕ, the three displacements u_1, u_2, u_3 and the quasi-Fermi energies $\mathscr{E}_{Fn}$ and $\mathscr{E}_{Fp}$ are chosen as degrees of freedom. The reason that the quasi-Fermi energy is chosen rather than charge density n and p is obvious: n and p are needed to

be determined by the electric potential, once they are independent of ϕ, the coupling is broken.

In the FEM framework that considers drift and diffusion, the quasi-Fermi energies rather than Fermi energy need be considered. Therefore, in the calculations for charge density carriers, including electrons, holes, ionized donors, ionized acceptors and trap charges, the Fermi energy needs to be replaced with the quasi-Fermi energy.

The ionization fraction for acceptors and donors is regarded,

$$t_a(\phi) = \frac{1}{1 + g_A \exp\left[\frac{\mathscr{E}_A - \mathscr{E}_{Fp} + q\phi}{kT}\right]}, \tag{6.1.10}$$

$$t_d(\phi) = \frac{1}{1 + g_D \exp\left[\frac{\mathscr{E}_{Fn} - q\phi - \mathscr{E}_D}{kT}\right]}. \tag{6.1.11}$$

The trap charges read,

$$n_a = N_t \int_{\mathscr{E}_v}^{\mathscr{E}_c} f(\mathscr{E}, \phi)\delta\left(\mathscr{E} - \mathscr{E}_{1a}\right) \mathrm{dE} = N_t f\left(\mathscr{E}_{1a}, \phi\right) = \frac{N_t}{1 + \exp\left(\frac{\mathscr{E}_{1a} - \mathscr{E}_{fp} + q\phi}{kT}\right)}. \tag{6.1.12}$$

Since generation and recombination always create or annihilate electron-hole pairs, the rates for them are the same and are expressed by the Shockley-Read-Hall formula [70]:

$$U_{np} = U_n = U_p = \frac{pn - n_i^2}{\tau_p\left(n + n_t\right) + \tau_n\left(p + p_t\right)} \tag{6.1.13}$$

where U_n and U_p are the generation and recombination rate for electrons and holes respectively. Moreover, τ_n and τ_p are the electron and hole lifetimes and n_t and p_t are the trap densities existing in the band gap, as shown in Fig. 3.2. In this work, n_t and p_t are assumed to be the same as intrinsic carrier concentration n_i. It needs to be noticed that Eq. 6.1.13 has the assumption that the recombination center lies at the middle of the bandgap, which can produce the highest rate than at other energy levels.

Similar to the flux of electrons, the flux of holes can be expressed as:

$$J_p = \mu_p p \nabla \mathscr{E}_{Fp}, \tag{6.1.14}$$

where J_p is the hole flux (A/m^2), and μ_p is drift mobility for holes ($m^2/V \cdot s$).

In this work, we denote the time derivative of electrons and holes as $\dot{\mathrm{n}}$ and $\dot{\mathrm{p}}$. The relation between flux and the charge changing rate is given as: $\dot{\mathrm{p}} = -\frac{1}{\mathrm{q}}\nabla \cdot \mathrm{J_p}$.

In fact, the flux flowing out of a specific volume equals the change of the charge densities inside

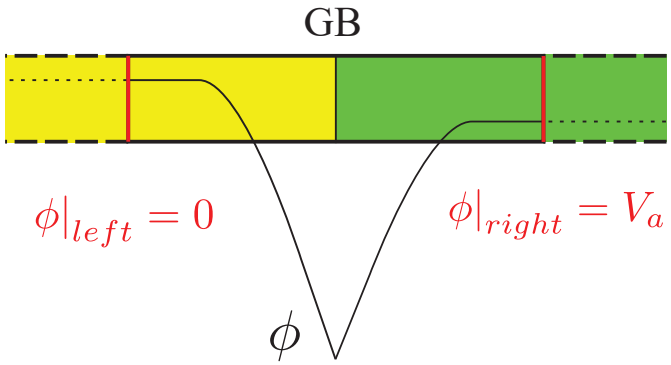

Figure 6.1: The bicrystal that is simulated in this chapter. The yellow and green parts represent left and right crystals. The actual boundary in the simulation is not at the real end of grain, but rather within a grain.

a volume:

$$\int_S \mathrm{J_p} \cdot \mathrm{d}\mathbf{A} = -\frac{\mathrm{d}}{\mathrm{d}t}\int_V \mathrm{p}\mathrm{d}V = -\int_V \dot{\mathrm{p}}\mathrm{d}V \tag{6.1.15}$$

where the negative sign indicates the reduction of the charge rate.

Owing to the Gauss theorem $\int_S \mathrm{J_p} \cdot \mathrm{d}\mathbf{A} = \int_V \nabla \cdot \mathrm{J_p}\mathrm{d}V$, we have $\int_V \nabla \cdot \mathrm{J_p}\mathrm{d}V = -\int_V \dot{\mathrm{p}}\mathrm{d}V$. Hence the flux and charge changing rate is expressed as:

$$\dot{\mathrm{p}} = -\frac{1}{\mathrm{q}}\nabla \cdot \mathrm{J_p} \tag{6.1.16}$$

Similarly, one has for electrons,

$$\dot{\mathrm{n}} = \frac{1}{\mathrm{q}}\nabla \cdot \mathrm{J_n} \tag{6.1.17}$$

in which there is no negative sign because the accumulation of the electrons at a position implies a positive out-coming flux.

If we consider generation and recombination, then the continuity equations are expressed as:

$$\dot{\mathrm{n}} = \frac{\partial \mathrm{n}}{\partial \mathrm{t}} = \frac{1}{\mathrm{q}}\nabla \cdot \mathrm{J_n} - \mathrm{U_{np}} = 0 \tag{6.1.18}$$

$$\dot{\mathrm{p}} = \frac{\partial \mathrm{p}}{\partial \mathrm{t}} = -\frac{1}{\mathrm{q}}\nabla \cdot \mathrm{J_p} - \mathrm{U_{np}} = 0 \tag{6.1.19}$$

in which only the steady-state ($\dot{\mathrm{n}} = \dot{\mathrm{p}} = 0$) is considered. On the one hand, in this work, it is more focused on the equilibrium state; on the other hand with this approach the time derivative of potential can be neglected, which will be addressed in the numerical part later.

In this chapter, the simulation still concentrates on the bicrystal, which represents one important feature of a polycrystalline. The conclusion drawn from the simulations is applicable to polycrys-

talline to a certain extent. Therefore, the bicrystal is regarded as cut out from a polycrystalline, which is demonstrated in Fig. 6.1. In this figure, the yellow and green parts represent left and right grains, respectively. The two vertical lines on the left and right-hand sides are the actual geometry boundary in the simulation. The dash lines are the cut-out part of the grains. As indicated by Fig. 6.1, the left and right boundaries are cut-off in the middle but not the actual ends of these two grains. Since in the middle of the grain, the physical quantities like potential and quasi-Fermi energy are steady. Therefore, it is easy to set as BCs.

The boundary conditions that are implemented on the bicrystal are as followings:

$$\sigma(z)\big|_{left} = \sigma_0, \tag{6.1.20a}$$

$$\sigma(z)\big|_{right} = \sigma_0, \tag{6.1.20b}$$

$$\phi|_{left} = 0, \tag{6.1.20c}$$

$$\phi|_{right} = V_a, \tag{6.1.20d}$$

$$\mathscr{E}_{Fn}|_{left} = \mathscr{E}_{Fp}|_{left} = \mathscr{E}_{f0}, \tag{6.1.20e}$$

$$\mathscr{E}_{Fn}|_{right} = \mathscr{E}_{Fp}|_{right} = \mathscr{E}_{f0} - qV_a. \tag{6.1.20f}$$

Thereby, σ_0 is the applied external stress, V_a is the applied voltage on a bicrystal and $\mathscr{E}_{f0}$ is the Fermi level which calculated from charge neutrality rule inside the bulk. In order to maintain the charge neutrality inside the grain, on the left side, both the quasi-Fermi energies for electrons and holes are held the same as $\mathscr{E}_{f0}$. Whereas on the right hand side since the $\mathscr{E}_C$ and $\mathscr{E}_V$ are altered by the external electric loading, the $\mathscr{E}_{Fn}$ and $\mathscr{E}_{Fp}$ need to be changed accordingly in order to meet the charge neutrality requirement on the right hand side.

6.2 Numerical implementation

The governing equations describing the force balance and electrostatics are Eq. 5.1.1 and 5.1.2; the drift and diffusion quantities are depicted by Eq. 6.1.18 and 6.1.19. Since in this work we choose FEM to solve these equations, the weak forms for these equations are derived as followings

respectively,

$$\begin{cases} \int_\Gamma \boldsymbol{\sigma} \cdot \delta \boldsymbol{u} \cdot \mathbf{n}_l \mathrm{ds} - \int_V \boldsymbol{\sigma} : \nabla \delta \boldsymbol{u} \mathrm{dv} = 0, \\ \int_\Gamma \mathbf{n}_l \cdot \boldsymbol{D} \delta\phi \mathrm{ds} - \int_V \boldsymbol{D} \cdot \nabla \delta\phi \mathrm{dv} - \int_V \rho_f \delta\phi \mathrm{dv} = 0, \\ -\int_V U_{np} \delta \mathscr{E}_{fn} \mathrm{dv} + \int_\Gamma \frac{1}{q} (\boldsymbol{J}_n \delta \mathscr{E}_{fn}) \cdot \mathbf{n}_l \mathrm{ds} - \int_V \frac{1}{q} \boldsymbol{J}_n \cdot \nabla \delta \mathscr{E}_{fn} \mathrm{dv} = 0, \\ \int_V U_{np} \delta \mathscr{E}_{fp} \mathrm{dv} + \int_\Gamma \frac{1}{q} \mathbf{n}_l \cdot (\boldsymbol{J}_p \delta \mathscr{E}_{fp}) \mathrm{ds} - \int_V \frac{1}{q} \boldsymbol{J}_p \cdot \nabla \delta \mathscr{E}_{fp} \mathrm{dv} = 0, \end{cases} \tag{6.2.1}$$

in which $\mathbf{n}_l$ is normal vector, ∇ represents taking gradient and bold symbol stands for tensor.

It should be noted that in the FEM calculation the displacements in three directions $\boldsymbol{u}$, potential ϕ, electron and hole quasi Fermi energy $\mathscr{E}_{fn}$ and $\mathscr{E}_{fp}$ are the degrees of freedom, which are not explicitly expressed and hidden in stress $\boldsymbol{\sigma}$, electric displacement $\boldsymbol{D}$, free charge densities ρ_f, recombination rate U_{np}, flux of electrons and holes $\boldsymbol{J}_n$ and $\boldsymbol{J}_p$.

The weak form can be explained by the virtual work principle. For example, the left part of the first equation Eq. 6.2.1 stands for the virtual work done on the boundary, and the right part corresponds to the virtual work done by the body.

In the former chapter, it has been demonstrated the importance of anisotropy. Hence we take advantage of FEM that it can be easily applied in 3D and continue to develop the drift and diffusion part in 3D.

Both the investigated geometry and the studied quantities are discretized. Specifically, the geometry is decomposed into the combination of 20-node quadratic elements; the quantities are discretized onto the nodes of the elements. Hence, each element has 20 nodes, and each node has 6 degrees of freedom,

$$\underline{\mathbf{d}} = [u_1^I \;\; u_2^I \;\; u_3^I \;\; \phi^I \;\; \mathscr{E}_{fn}^I \;\; \mathscr{E}_{fp}^I]^T, \tag{6.2.2}$$

where the quantities with superscript I denote the corresponding nodal values of the node I and the underlined bold symbol represents a matrix.

The values of the DOFs for points inside one element are interpolated by the shape functions N^I, which is based on the nodal values. Hence the degrees of freedoms on any point in the geometry

are expressed as,

$$\begin{cases} \boldsymbol{u} = \sum_I N_u^I \boldsymbol{u}^I; & \delta\boldsymbol{u} = \sum_I N_u^I \delta\boldsymbol{u}^I, \\ \phi = \sum_I N_\phi^I \phi^I; & \delta\phi = \sum_I N_\phi^I \delta\phi^I, \\ \mathscr{E}_{fn} = \sum_I N_{fn}^I \mathscr{E}_{fn}^I; & \delta\mathscr{E}_{fn} = \sum_I N_{fn}^I \delta\mathscr{E}_{fn}^I, \\ \mathscr{E}_{fp} = \sum_I N_{fp}^I \mathscr{E}_{fp}^I; & \delta\mathscr{E}_{fp} = \sum_I N_{fp}^I \delta\mathscr{E}_{fp}^I, \end{cases} \tag{6.2.3}$$

where the second-order shape functions are implemented to increase the convergence.

The second-order tensor stress and strain are symmetric by introducing the Voigt notation. The following expressions are denoted by the matrix form where the strain, stress, electric field and dielectric displacement are expressed by,

$$\begin{cases} \underline{\boldsymbol{S}} = \sum_I \underline{\boldsymbol{B}}_{\boldsymbol{u}}^I \underline{u}^I, \\ \underline{\boldsymbol{\sigma}} = \underline{\mathbf{C}}\,\underline{\mathbf{S}} - \underline{\mathbf{e}^T}\,\underline{\mathbf{E}}, \\ \underline{\boldsymbol{E}} = -\sum_I \underline{\boldsymbol{B}}_\phi^I \phi^I, \\ \underline{\boldsymbol{D}} = \underline{\boldsymbol{\varepsilon}_s}\underline{\boldsymbol{E}} + \underline{\boldsymbol{P}} + \underline{\boldsymbol{P}}_s, \end{cases} \tag{6.2.4}$$

where $\underline{\boldsymbol{B}}_{\boldsymbol{u}}^I$ and $\underline{\boldsymbol{B}}_\phi^I$ are the matrices regarding the gradient of shape functions,

$$\begin{cases} \underline{\boldsymbol{B}_{\mathbf{u}}^{\mathbf{I}}} &= \begin{bmatrix} N_{,1}^I & \mathbf{0} & \mathbf{0} & \mathbf{0} & N_{,3}^I & N_{,2}^I \\ \mathbf{0} & N_{,2}^I & \mathbf{0} & N_{,3}^I & \mathbf{0} & N_{,1}^I \\ \mathbf{0} & \mathbf{0} & N_{,3}^I & N_{,2}^I & N_{,1}^I & \mathbf{0} \end{bmatrix}, \\ \underline{\boldsymbol{B}}_\phi^I &= [N_{,1}^J \quad N_{,2}^J \quad N_{,3}^J]^T. \end{cases} \tag{6.2.5}$$

From Eq. 6.2.1 the residuals of the degrees of freedoms within the element volume V are derived as,

$$\begin{cases} \underline{\boldsymbol{R}}_u^I = -\int_V \underline{\boldsymbol{B}}_u^I \left[\underline{\boldsymbol{C}}\left(\underline{\boldsymbol{B}}_u^J \underline{\boldsymbol{u}}^J\right) + \underline{\boldsymbol{e}}^T \underline{\boldsymbol{B}}_\Phi^I \cdot \phi^J\right] \mathrm{dv}, \\ R_\phi^I = -\int_V \left(\underline{\nabla N^I}\right)^T \left(-\underline{\boldsymbol{\varepsilon}_s}\underline{\boldsymbol{B}}_\phi^J \cdot \phi^J + \underline{\boldsymbol{e}}\underline{\boldsymbol{B}}_u^J u^J + \underline{\boldsymbol{P}}_s\right) \mathrm{dv} - \int_V \rho_f N^I \mathrm{dv}, \\ R_{\mathscr{E}_{fn}}^I = -\int_V (U_{np} N^I + \frac{1}{q}\underline{\boldsymbol{J}}_n \cdot \underline{\nabla N^I}) \mathrm{dv}, \\ R_{\mathscr{E}_{fp}}^I = \int_V (U_{np} N^I - \frac{1}{q}\underline{\boldsymbol{J}}_p \underline{\nabla N^I}) \mathrm{dv}, \end{cases} \tag{6.2.6}$$

Table 6.1: Normalization factors of some main physical quantities

Normalized physical quantities	Scaling factors	
	Name	Value
Space	Extrinsic Debye length	$L = \sqrt{\frac{\kappa_0 V_{th}}{qN}}$
Potential	Thermal voltage	$V_{\text{th}} = \frac{k_{\text{B}}T}{q}$
Carrier concentration	Doping concentration	$N = N_{\text{d}}$
Pressure		$P = qV_{th}N$
Electric displacement and piezoelectric constants		$D_{\text{E}} = qLN$

(6.2.8)

where the $\underline{\underline{e}}$ is piezoelectric matrix taking the Voigt notation from piezoelectric tensor.

The stiffness matrix can be expressed by the positive partial differential of the residuals with respect to degrees of freedoms as,

$$\begin{cases} \underline{\underline{\boldsymbol{K}}}^{IJ}_{\boldsymbol{uu}} = \dfrac{\partial \underline{\boldsymbol{R}}^I_{\boldsymbol{u}}}{\partial \underline{\boldsymbol{u}}^J}; \quad \underline{\boldsymbol{K}}^{IJ}_{\boldsymbol{u}\phi} = \dfrac{\partial \underline{\boldsymbol{R}}^I_{\boldsymbol{u}}}{\partial \phi^J}; \quad \underline{\boldsymbol{K}}^{IJ}_{\boldsymbol{u}\mathscr{E}_{fn}} = \dfrac{\partial \underline{\boldsymbol{R}}^I_{\boldsymbol{u}}}{\partial \mathscr{E}^J_{fn}}; \quad \underline{\boldsymbol{K}}^{IJ}_{\boldsymbol{u}\mathscr{E}_{fp}} = \dfrac{\partial \underline{\boldsymbol{R}}^I_{\boldsymbol{u}}}{\partial \mathscr{E}^J_{fp}} \\ K^{IJ}_{\phi\boldsymbol{u}} = \dfrac{\partial R^I_{\phi}}{\partial \underline{\boldsymbol{u}}^J}; \quad K^{IJ}_{\phi\phi} = \dfrac{\partial R^I_{\phi}}{\partial \phi^J}; \quad K^{IJ}_{\phi\mathscr{E}_{fn}} = \dfrac{\partial R^I_{\phi}}{\partial \mathscr{E}^J_{fn}}; \quad K^{IJ}_{\phi\mathscr{E}_{fp}} = \dfrac{\partial R^I_{\phi}}{\partial \mathscr{E}^J_{fp}} \\ K^{IJ}_{\mathscr{E}_{fn}\boldsymbol{u}} = \dfrac{\partial R^I_{\mathscr{E}_{fn}}}{\partial \underline{\boldsymbol{u}}^J}; \quad K^{IJ}_{\mathscr{E}_{fn}\phi} = \dfrac{\partial R^I_{\mathscr{E}_{fn}}}{\partial \phi^J}; \quad K^{IJ}_{\mathscr{E}_{fn}\mathscr{E}_{fn}} = \dfrac{\partial R^I_{\mathscr{E}_{fn}}}{\partial \mathscr{E}^J_{fn}}; \quad K^{IJ}_{\mathscr{E}_{fn}\mathscr{E}_{fp}} = \dfrac{\partial R^I_{\mathscr{E}_{fp}}}{\partial \mathscr{E}^J_{fp}} \\ K^{IJ}_{\mathscr{E}_{fp}\boldsymbol{u}} = \dfrac{\partial R^I_{\mathscr{E}_{fp}}}{\partial \underline{\boldsymbol{u}}^J}; \quad K^{IJ}_{\mathscr{E}_{fp}\phi} = \dfrac{\partial R^I_{\mathscr{E}_{fp}}}{\partial \phi^J}; \quad K^{IJ}_{\mathscr{E}_{fp}\mathscr{E}_{fn}} = \dfrac{\partial R^I_{\mathscr{E}_{fp}}}{\partial \mathscr{E}^J_{fn}}; \quad K^{IJ}_{\mathscr{E}_{fp}\mathscr{E}_{fp}} = \dfrac{\partial R^I_{\mathscr{E}_{fp}}}{\partial \mathscr{E}^J_{fp}}. \end{cases} \tag{6.2.7}$$

As mentioned before, the quantities in the residuals, for instance, U_{np} and $\underline{\boldsymbol{J}}_n$ are in the end the functions of degrees of freedoms. Hence the derivative of them with respect to degrees of freedoms can be calculated by chain rules.

The model is implemented in the finite element environment MOOSE [92]. Note that it is a convention that the stiffness matrix is defined as a positive partial differential.

In the simulation, to increase the convergence of the computation, normalization is implemented. The factors are shown in Table 6.1. The full relation of the normalized quantities is demonstrated in Appendix 9.3.

6.3 Results and discussion

For the drift and diffusion calculation, the parameters listed in Table 5.1 for the barrier height calculation are taken over for the simulations here. The rest parameters that are involved in the

diffusion model are shown in Table 6.2:

Table 6.2: Parameters used in simulation. [93]

Parameter	Value
n_i	1.268×10^{-15} m^{-3}
n_t	1.268×10^{-15} m^{-3}
p_t	1.268×10^{-15} m^{-3}
τ_n	1×10^{-7} s
τ_p	1×10^{-7} s
μ_n	1.80 cm^2/Vs
μ_p	1.80 cm^2/Vs

Thereby, n_t and p_t are assumed to be the same as n_i [94], which has the definition as:

$$n_i = \sqrt{N_c N_v}\exp\left(-\frac{\varepsilon_g}{2k_B T}\right) \tag{6.3.1}$$

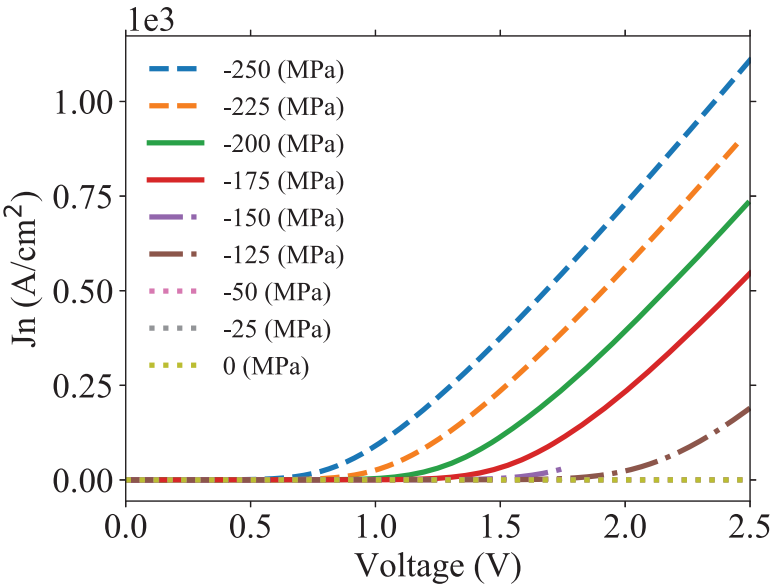

Figure 6.2: The variation of electron flux with voltage and external loading.

The FEM results show that the ZnO bicrystal has a typical varistor behaviour, as demonstrated in Fig. 6.2. As the bias voltage increases, the electron flux is constrained until a specific voltage. When the bias voltage increases further, the flux escalates intensely and the breakdown happens. In the simulation, several external stress states are implemented, varying from 0 MPa to -250 MPa. The lines in Fig. 6.2 indicate that when the loading increases, the breakdown occurs at a lower voltage. It also illustrates that when applying the same external voltage, the larger external loading resulting in a higher flux output. Moreover, after the breakdown, the higher mechanical

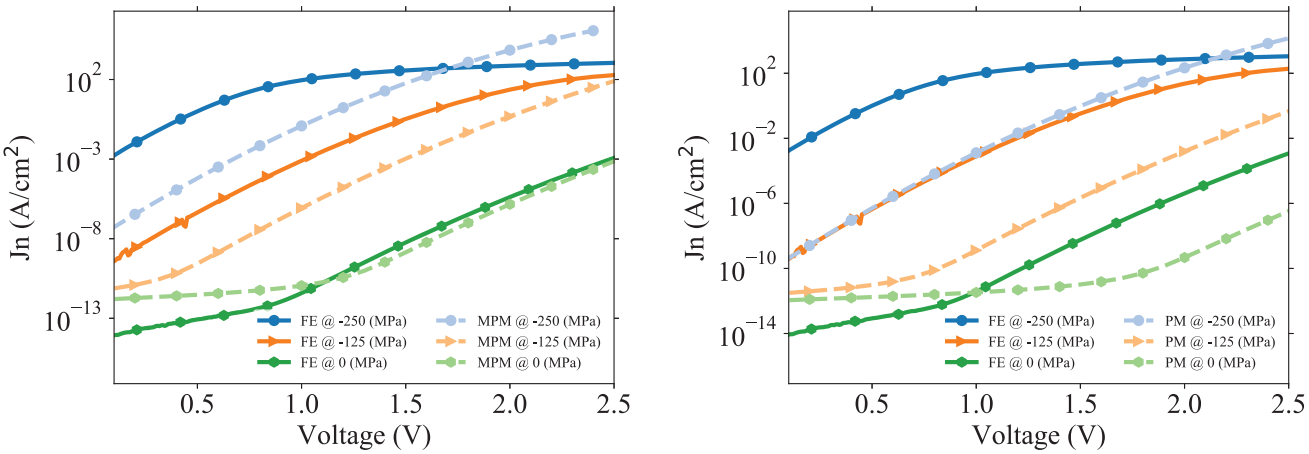

(a) Flux comparison FE vs MPM (f=0.128).

(b) Flux comparison FE vs PM (f=0).

Figure 6.3: Comparison of FE with two phenomenological models PM and MPM. All the three models give the varistor behaviour of ZnO. The MPM produces a much closer flux prediction comparing to PM, especially at low stress regions.

loading produces a steeper slope, which implies the bicrystal is more sensitive to the applied voltage.

On the other hand, the hole flux J_p is zero in the simulation for all cases. Since $\mathscr{E}_{Fp}$ is far apart from $\mathscr{E}_V$, the hole density is extremely low and can be neglected. Hence, the hole flux is not plotted and is not considered in this work.

The flux calculation from FE, PM and MPM are compared and shown in Fig. 6.3. The three stress states are compared, and the trend agrees with each other. It is obvious that compared to the PM results, the results from MPM agrees much better with FEM, especially at low-stress levels. At high stress levels, as demonstrated in Chapter 4, the maximum of J_n for MPM is $AT^2 = 2.7 \times 10^6$. Whereas the FEM reaches its maximum at around 10^3, which is demonstrated by FE @ -250 MPa.

In the head-to-head depending configuration, it has been demonstrated in Fig. 5.4 that with no bias voltages, the barrier height decreases with the increasing of the external stress. This effect has been proven again in Fig. 6.4. Moreover, it is shown in Fig. 6.4 that increasing the applied voltage tends to decrease the barrier height. In the low applied mechanical stress level, for instance, 0 MPa, -25 MPa, and -50 MPa, there are still plateaus when applying voltage, while the plateau vanishes for the stress larger than -125 MPa. The reason is that at 0 voltage, for the large stresses, e.g. -125 MPa, the barrier height is low so that the trap DOS is already fully occupied, as demonstrated in Fig. 5.4 with black solid line. It can be observed from Eq. 4.2.22 that when external loading is fixed, the barrier height depends only on external voltage V. Consequently, the barrier height is quadratic polynomial depending on the voltage.

It can be noticed from Eq. 4.2.22 that the MPM (and the PM) do not provide a negative barrier height. However, in the FE simulation, it can be observed that the barrier height can be negative

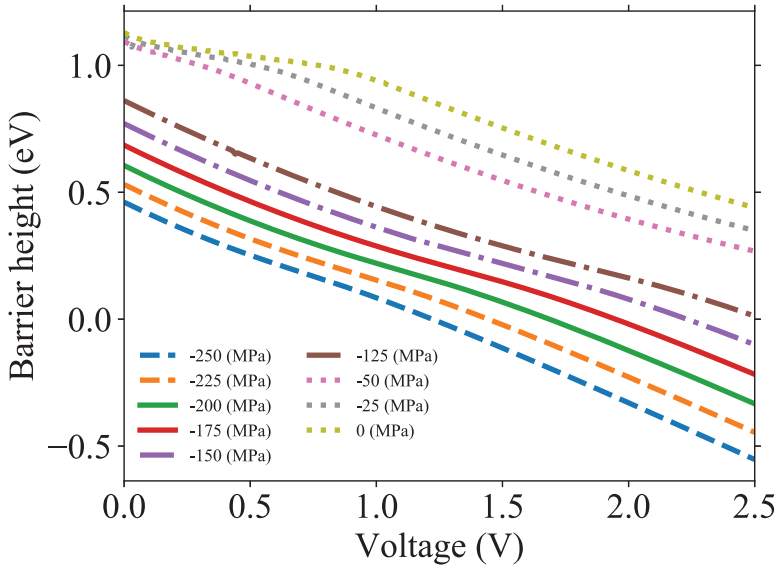

Figure 6.4: Barrier height variation with external voltage. Several external voltages are implemented.

when the external voltage and stress are high enough, which will be addressed later in this chapter.

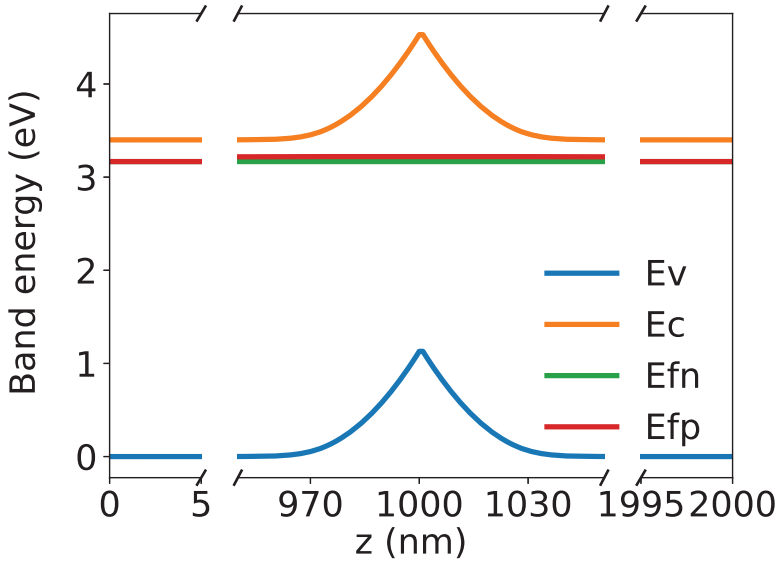

Figure 6.5: Band structure @ 0 MPa and 0 V

Fig. 6.5 illustrates the band structure for zero external stress and voltage. The difference between Fig. 6.5 and Fig. 5.1 is that the two quasi-Fermi energies do not equal in the depletion region, although they are set to be equal at the boundary. In Fig. 6.5, the $\mathscr{E}_{fp}$ is lifted up in the depletion region. Therefore, there are more trap densities in the GB than in Fig. 5.1, producing a higher barrier height (1.10 eV in Fig. 5.1 VS 1.13 eV in Fig. 6.5). In fact, by taking quasi-Fermi

energies into account, the barrier height is higher than that of the case where a single Fermi energy is considered. Nevertheless, the difference is not that prominent.

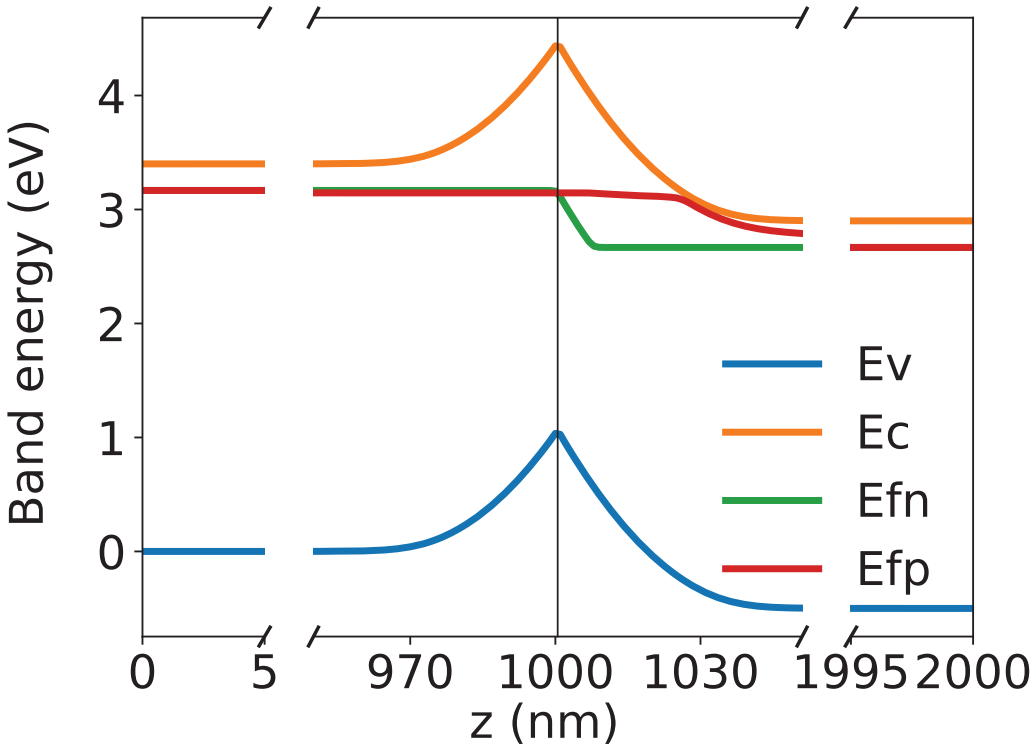

Figure 6.6: Band structure @ 0 MPa and 0.5 V

The band structure of the bicrystal with no external stress and 0.5 V bias voltage is shown in Fig. 6.6. Since 0.5 V is applied, based on Eq. 6.1.20, the boundary conditions for potential and quasi-Fermi energies are adjusted accordingly. Hence, on the right-hand side $\mathscr{E}_V$, $\mathscr{E}_C$, $\mathscr{E}_{fn}$, and $\mathscr{E}_{fp}$ are turned down for 0.5 eV. The calculation result shows $\mathscr{E}_{fn}$ is shifted with a step near around the GB while $\mathscr{E}_{fp}$ lowers down when it meets $\mathscr{E}_C$.

The arrangement of the quasi-Fermi energies in the depletion region is formed by two steps. At the first step, hot electrons and subsequent holes are generated. Hence, as Fig. 6.7 (a) illustrates, the quasi-Fermi energy for holes $\mathscr{E}_{fp}$ shifts down close to the conduction band for a higher concentration of holes, whereas the quasi-Fermi energy for electrons $\mathscr{E}_{fn}$ only shifts upward Imperceptibly, since the generated electrons are significantly less compared to the state before the bicrystal is biased. At the second step, as Fig. 6.7 (b) shows, the generated holes then diffuse back to the GB, reducing the negative charges. Consequently, the barrier height is reduced. The reducing of the holes lifts the $\mathscr{E}_{fp}$ up.

The negative barrier heights in Fig. 6.4 are allowed in FEM showing in Fig. 6.8. When the bias voltage is high enough, the band energies could be bent and the barrier height could be lower than the 0 eV reference point on the left end. According to Eq. 4.2.10, Eq. 4.2.22 and the assumption $\Phi(-\infty) = \Phi(-x_l) = 0$ and $\Phi(\infty) = \Phi(x_r) = -V$, the MPM (or PM) on the other

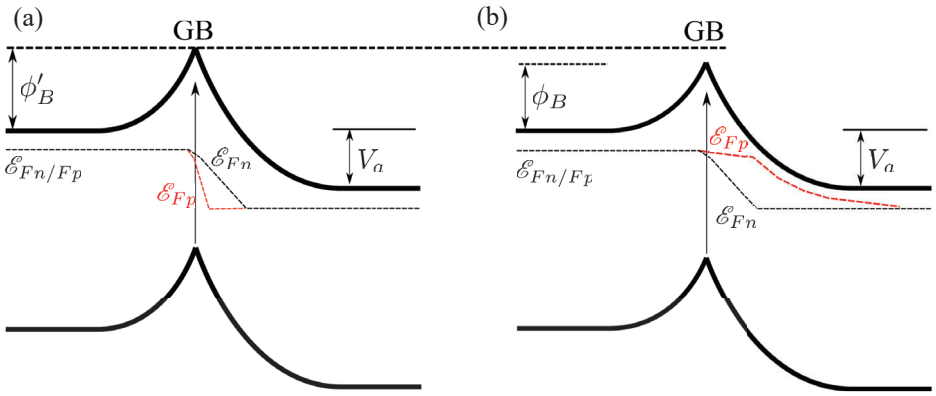

Figure 6.7: The shift of quasi-Fermi energy during hole diffusing to GB. (a)Generation of electron and hole pairs; (b) holes diffuse to the GB, leading to the decrease of the barrier height.

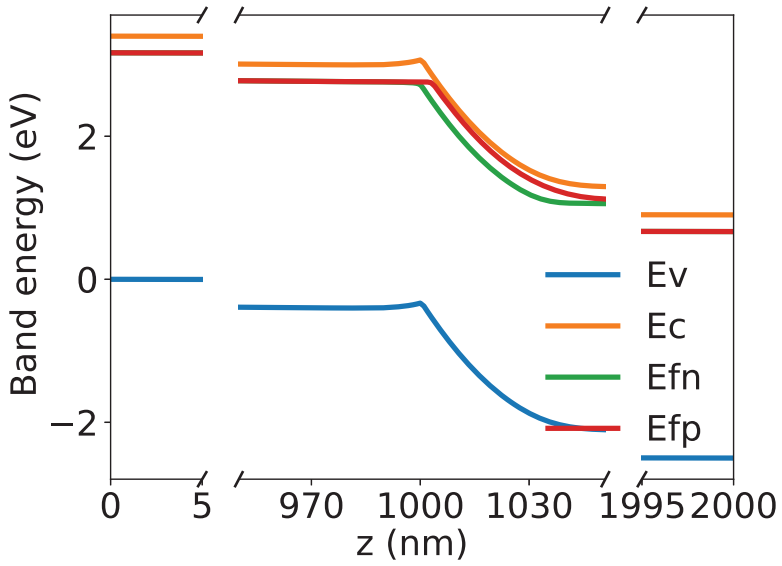

Figure 6.8: Band structure for a 200 MPa external stress and 2.5 V bias voltage

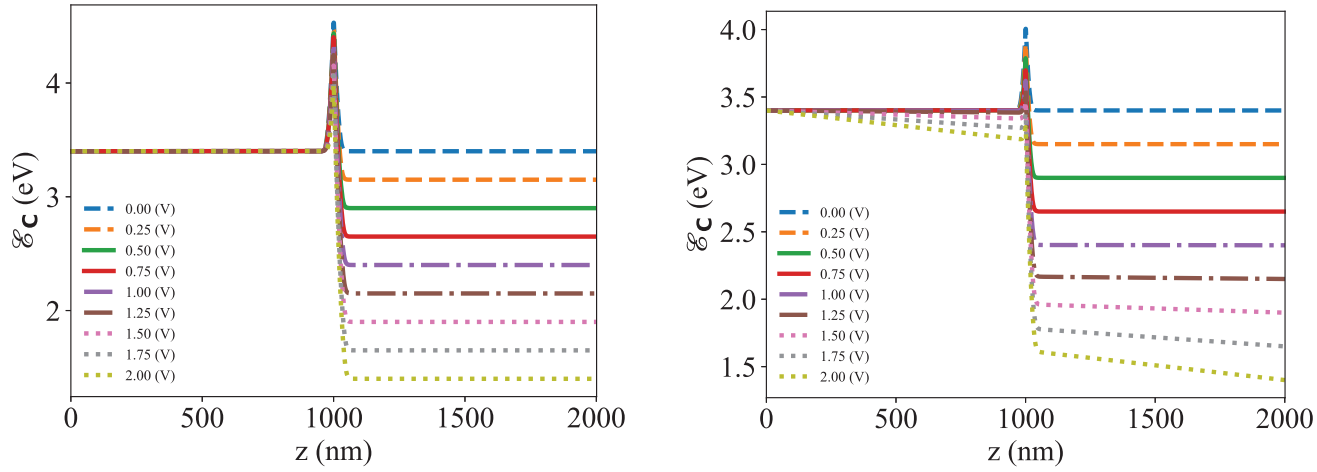

(a) $\mathscr{E}_C$ distribution in space at zero stress. The voltage increases from 0.00 V to 2.00 V with an 0.25 V interval;

(b) $\mathscr{E}_C$ distribution along z-axis at 200 MPa compressive stress. The negative barrier heights are observed;

Figure 6.9: $\mathscr{E}_C$ distribution at 0 and 200 MPa

hand, has a flat $\mathscr{E}_c$ band outside the depletion region and the barrier height can only be positive, which is not the real case when the external electric field is high enough (will be demonstrated later). As it can also be observed from Fig. 6.8, the $\mathscr{E}_{fn}$ also has the gradient along the z-axis, which is exactly the driving force of the motion of the electrons. These differences of the FEM and MPM naturally have influences on the flux calculation results.

Fig. 6.9a illustrates the distribution of conduction band $\mathscr{E}_C$ with no external stress loading. By increasing the voltage, the barrier height decreases, and the $\mathscr{E}_C$ of the right grain lowers an amount of the applying bias voltage. However, the band is almost flat outside the depletion region, which indicates the electrons do not have the potential gradient to move across the grain. Therefore there is no driving force inside the grain, hence no electron flux.

The density distributions of electrons, holes, ionized donors and ionized acceptors with a variation of external stresses and bias voltages are illustrated in Fig. 6.10. As shown in Fig. 6.10a, since the band structure and quasi-Fermi energies are very close to the result of the previous FEM model, the charge distributions are very similar to Fig. 5.8; when applying an electric field, i.e. increasing the potential on the right end, the electrons are driven to right side whereas the ionized donors are pushed to the left which is shown in Fig. 6.10b; the intensify of the mechanical loading leads to lower barrier height, hence the depletion region is shrunk, showing in Fig. 6.10c; at high mechanical and electric loadings, the electron distribution in the depletion region shows gradient, which also contributes to the flux.

The distribution of $\mathscr{E}_C$ with 200 MPa compressive loading is shown in Fig. 6.9b. Since it is a head-to-head configuration, the barrier height is lowered compared to the case with mechanical loading. When the bias voltage increases to 1.25 V, the band is still flat. Therefore there is no

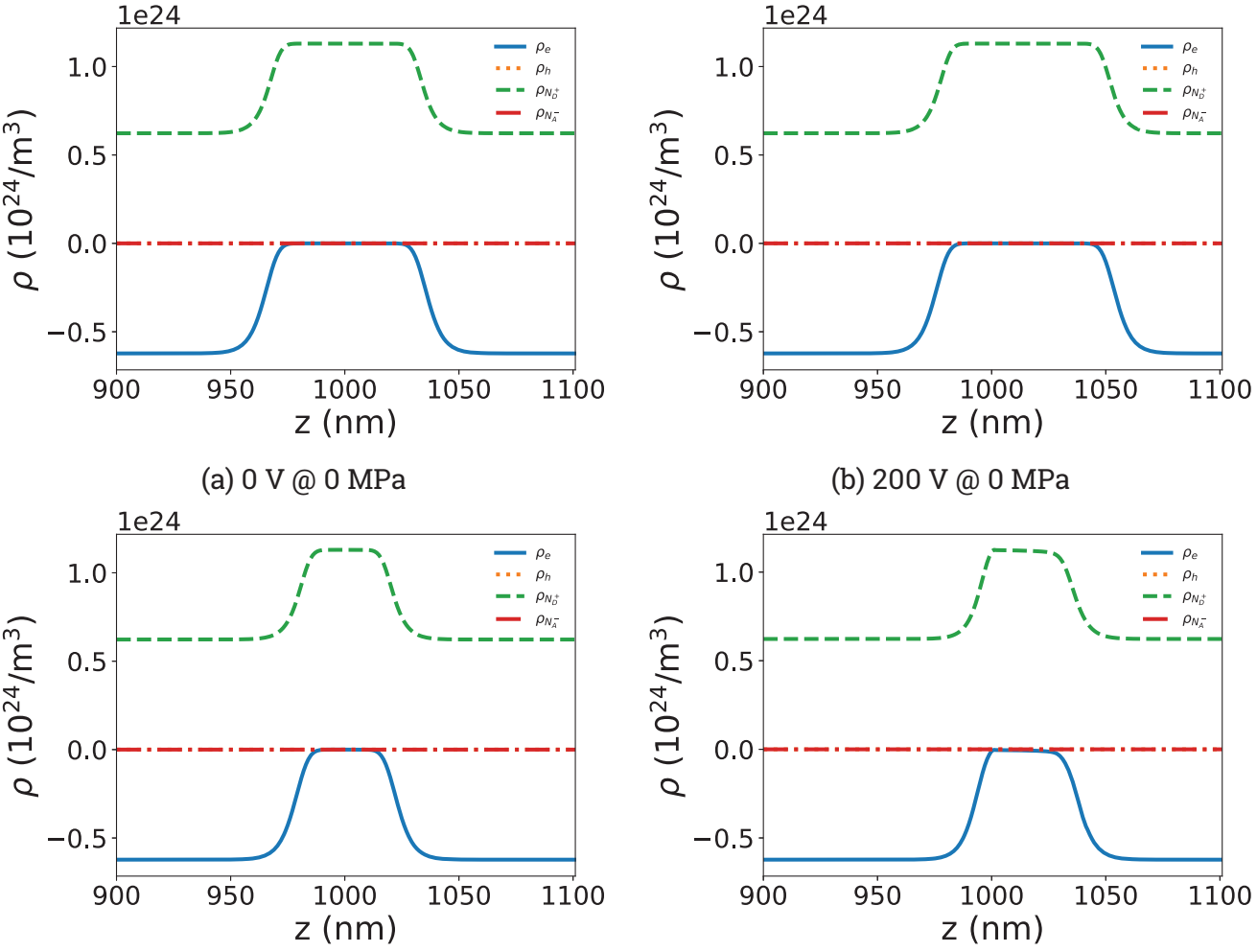

(a) 0 V @ 0 MPa

(b) 200 V @ 0 MPa

(c) 0 V @ 250 MPa

(d) 200 V @ 250 MPa

Figure 6.10: Densities of electrons, holes, ionized donors, and ionized acceptors with the variation of external stresses and bias voltages. (a) Since the band structure and quasi-Fermi energies are very close to the result of the previous FEM model, the charge distributions are very close comparing to Fig. 5.8; (b) the electrons are driven to the right side which has a higher potential whereas the ionized donors are pushed to the left; (c) the barrier height is lowered by the mechanical loading, hence the depletion region is shrunk; (d) similar to case (b), the electrons and ionized donors are pushed to the opposite directions, the gradient of the electron distribution in the depletion region also contributes to the flux.

electron flux from 0 V to 1.25 V bias voltage, which is demonstrated in Fig. 6.2. Increasing the bias voltage further, the conduction band starts to bend, which suggests that there is electron flux flow through the grains. Fig. 6.9b also shows that with a higher bias voltage, $\mathscr{E}_C$ is bent more, implying that the higher bias voltage leads to higher electron flux.

Fig. 6.9a and Fig. 6.9b imply that both applying voltage and stress can lower the barrier height. However, to let the electron flux flow through, the barrier height needs to be lowered close to zero. Fig. 6.11 suggests that with 2 V applying, the breakdown happens when the external loading reaches 150 MPa.

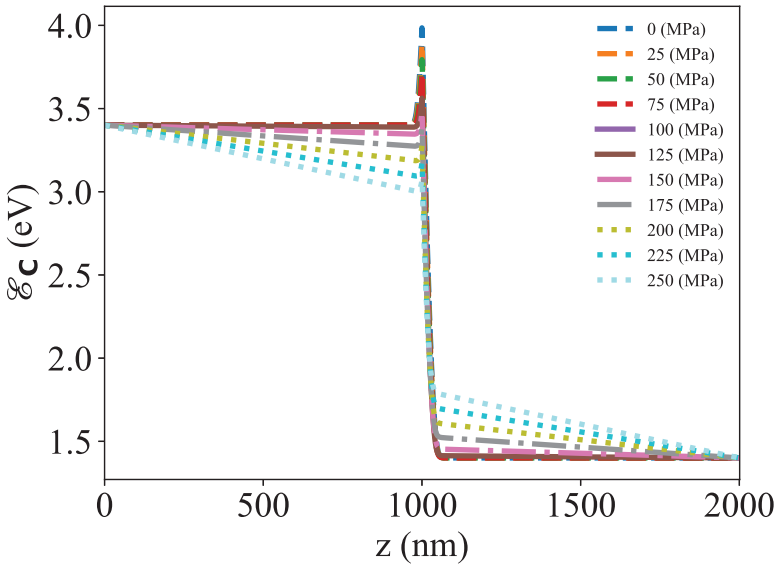

Figure 6.11: $\mathscr{E}_C$ distribution with different external loadings at 2 V bias voltage.

A bias voltage of 2 V with different stress states is demonstrated in Fig. 6.11. It shows the ability of the bicrystal using as a field-effect transistor. When external loading is 125 MPa or lower, the device is switched off, while the stress above that value can let the current through. Note that the electron can cross the barrier height when it is very low.

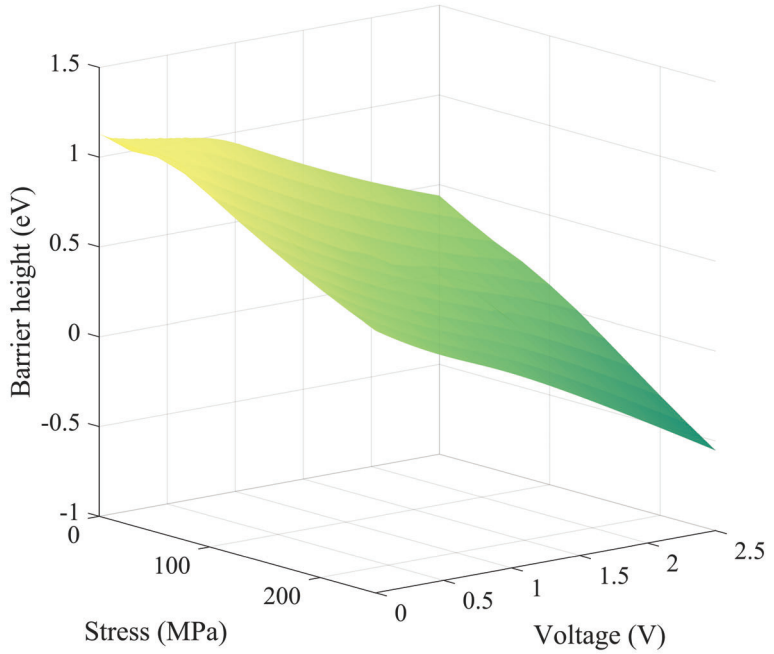

Figure 6.12: Barrier height variation with respect to bias voltage and stress. The barrier height has a plateau when the bias voltage and stresses are low. It can be noticed that when the stress is above 50 MPa or the voltage is larger than 1.0 V, the sudden drop of the barrier height already begins.

A bias voltage, stress and barrier height contour plot is shown in Fig. 6.12. The barrier height has a plateau when both the bias voltage and stresses are low. It can be noticed that when the stress is above 50 MPa or the voltage is more extensive than 1.0 V, the sudden drop of the barrier height already begins. Comparing to the MPM shown in Fig. 4.9, the plateau region from FEM is significantly smaller, and the barrier height can reach down to the negative barrier height.

The contour plot of flux is plotted in Fig. 6.13a, which shows the higher the stress, the lower is the breakdown voltage. The figure also shows at low stresses the breakdown will not happen at the bias voltage scale which we calculated. This indicates that if the device needs to be operated at low voltage scales, the initial barrier height needs to be lowered, which means the defect DOS needs to be reduced.

In order to compare the trends of the data with different magnitudes, the Φ_B and J_n are normalized and plotted in Fig. 6.13b. The breakdown of the flux is marked with a green plane. The cross-section of green and purple surfaces reveals the value of the barrier height that the breakdown happens. This normalized value 0.4 refers to the actual barrier height 0.1202 eV, which demonstrates again the breakdown happens when the barrier height is near zero.

The contour plot of trap charge density Q_I is shown in Fig. 6.14a. The relation between Q_I and barrier height Φ_B is presented in Fig. 6.14b. A clear plateau of Q_I is established after the

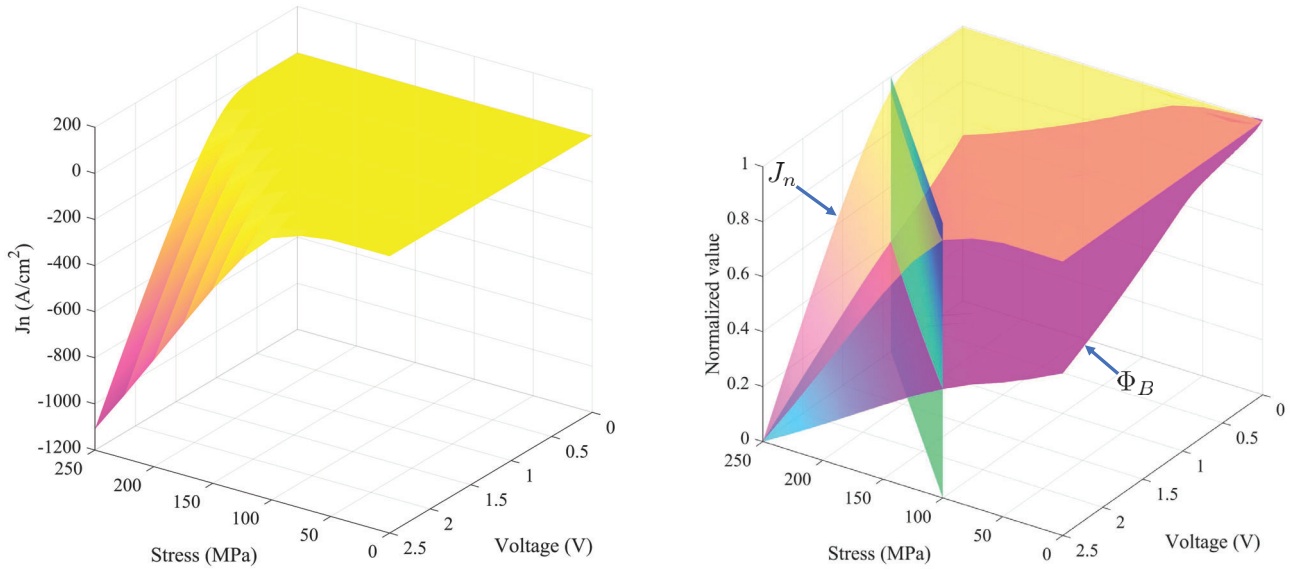

(a) The variation of electron flux J_n with respect to stress and bias voltage. The breakdown happens when the stress is more extensive than 100 MPa, or the voltage is large than 1.5 V. Comparing to Fig. 6.12, the plateau is much larger, which suggests the start of the sudden drop of barrier height does not indicate the start of breakdown.

(b) The normalized plot for barrier height and electron flux density. The vertical plane demonstrates the start of breakdown. Normalized point 0.4 on the z-axis refers to the barrier height 0.1202 eV

Figure 6.13: Contour plot of flux Jn and its comparison with barrier height Φ_B.

sudden drop of barrier height.

6.4 Conclusion

Instead of using the flux equations, which divide the flux into drift and diffusion parts and which require the employment of charge density as the degrees of freedom, we introduced the quasi-Fermi energies into the system to calculate the I-V curve. It brings much more convenience, and the densities of charges can be calculated from a more physical foundation. Since ZnO is naturally an n-type semiconductor, the hole flux J_p is miniature which can be neglected. The electron flux J_n reveals a clear varistor behaviour; in other words, after the breakdown, the flux increases dramatically. With the head-to-head configuration, increasing the external loading decreases the barrier height, and hence also decreases the breakdown point. The comparison among FEM, MPM and PM demonstrated again that consideration of the internal electric field is necessary and has a vast influence in calculating the flux. Unlike the MPM, in FEM, the barrier height can reach below 0 eV, and the flux breakdown is not relevant to the sudden drop of the barrier height. On

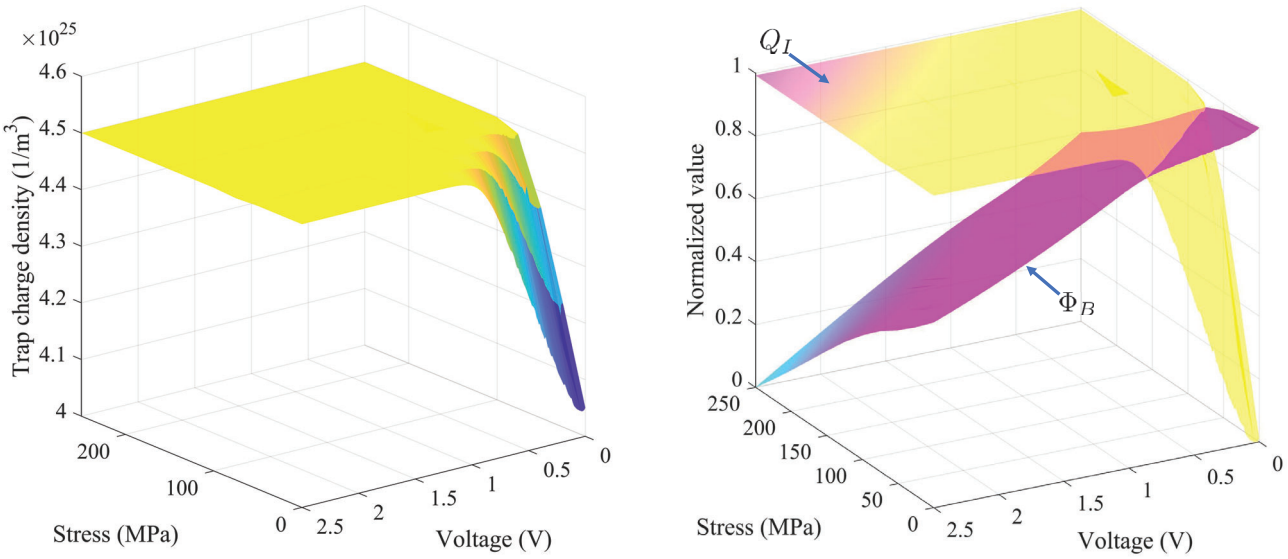

(a) Trap charge variation concerning stress and bias voltage. The plateau region denotes a higher trap charge which is associated to the lower barrier height. The lower trap charge regions indicate higher barrier height. The amount of trap charges corresponds to the barrier height which is shown in Fig. 5.7.

(b) The normalized plot for barrier height and trap charge density. The vertical plane demonstrates the start of breakdown.

Figure 6.14: Contour plot trap charge density Q_I and its comparison with barrier height Φ_B.

the other hand, breakdown of the flux is controlled by the gradient of the band structure and happens always accompanied by a minimal barrier height.

7 Parameter study via neural networks

Even though the physical FE simulations provide insightful knowledge, the computation capacity is limited, and the investigated parameter regions are restricted. Moreover, the numerical results can be made more accessible via surrogate models for a broad community. As shown in Chapter 6 in FEM we applied the external voltage from 0 V to 2.5 V with an interval of 0.01 V, and the external loading varies from 0 MPa to -250 MPa, with an increment of 25 MPa. Hence, there are more than 2500 datasets (including the input and output data) as labelled examples which is enough for the accuracy of predicting the unlabelled examples. Comparing to a standard fitting procedure, the neural network is able to output the errors of the predictions which evaluate the accuracy of the model. Moreover, with the massive tools from neural networks, it is much easier to evaluate the data quality. Thus one can have a better grasp of how confident is the prediction.

7.1 Theory

Machine learning becomes a hot topic not only in computer science, but also in other fields for instance: economics [95], finance [96], robotics [97], and material science [98, 99]. Machine learning requires a large amount of input dataset, which can be well obtained from the simulation results using the physical models. Therefore, in this work, we implement a neural network to predict unknown dataset by using the results from the FEM. In this part, machine learning and its terminologies are briefly introduced to let the reader from material science quickly capture the basic ideas. [100]

Labels are the values which need to predict. In this thesis these values are for instance, "Φ_B", "J_n", "n" and "p" are the labels; features are the input variables, which in our case are external applying stress and electric loading; examples are the instance of data which have two categories: labelled examples and unlabelled examples. The labelled examples contain both labels and the corresponding features and are normally used to train the model. The unlabelled examples contain only features, and we use the trained models to predict the labels; models build the relationship between features and labels. In our case, for example, a model is to build the neural network for external mechanical and electrical loading with barrier height or the flux of electrons; training a model means to use the labelled examples to let the model learn the relationship between features

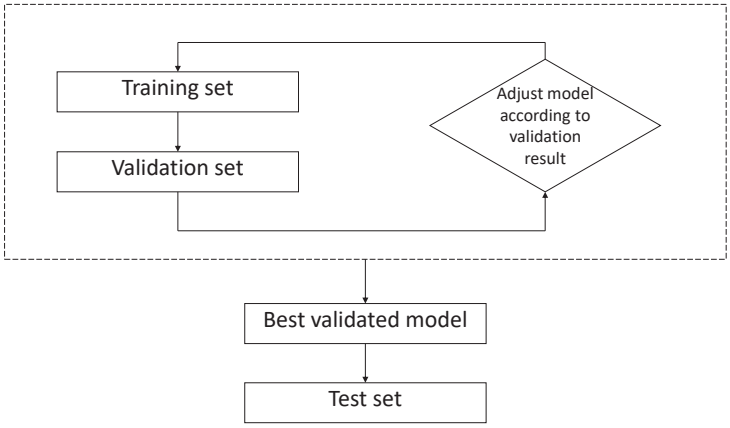

Figure 7.1: Work flow of the neural networks

and labels; the mean square error (MSE) is often referred to as loss, depicts the square of the difference between predictions (y) and observations ($\hat{y}$):

$$MSE = \frac{\sum_{i=1}^{n} (y_i - \hat{y}_i)^2}{n} \tag{7.1.1}$$

The MSE has an outstanding property that the predictions far away from the true values are penalized much more than the less deviated predictions.

The mean absolute error (MAE) is a measure of the absolute difference between predictions (y) and observations ($\hat{y}$):

$$MAE = \frac{\sum_{i=1}^{n} |y_i - \hat{y}_i|}{n} \tag{7.1.2}$$

Since the MAE has no penalty for the far away predictions, it reviews a more intuitive impression of how large the predictions deviate from the true values.

We use supervised machine learning, which means the input dataset contains both labels and features, while the unsupervised learning only contains labels. The former is usually used in regression, while the latter is employed regularly in classification.

In order to have proper training, the dataset is necessarily divided into three parts: the training set, the test set, and the validation set, as illustrated in Fig. 7.1. The training process is like followings: the training set is used to train the data; the model is then evaluated using validation set; during the validation, the training process is adjusted by for instance tuning the learning rate or remove some labels; the best-validated model is then evaluated by the test set.

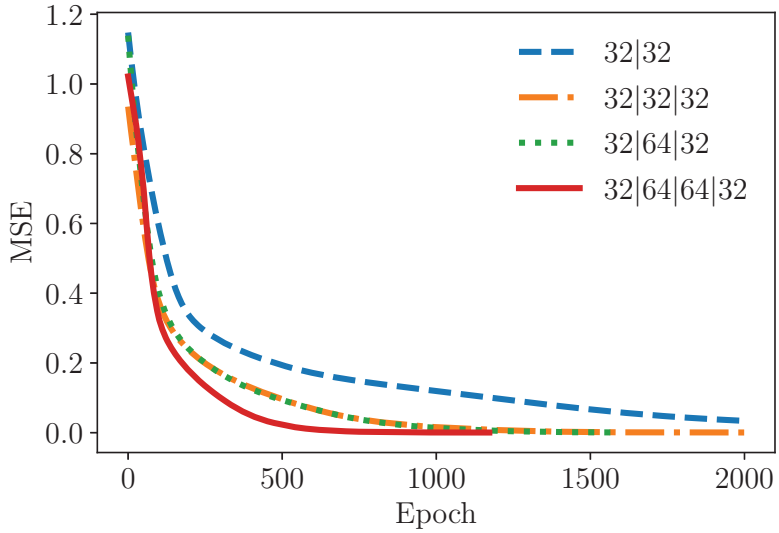

Figure 7.2: The MSE comparison for different numbers of hidden layers and neurons.

7.2 Model description

The training implements the famous open-source neural-network library Keras on top of Tensorflow. The Keras and the Tensorflow version versions are 2.24 and 1.14, respectively. The activation function is ReLU (rectified linear unit), which has a definition of $f(x) = \max(0, x)$. The optimizer is RMSprop, and the learning rate is adjusted to 0.00001 due to the high non-linearity of electron flux density and trap charge density. In the simulation, one batch contains 10 examples from the training set, and the model uses one batch instead of all the training set to provide a much faster convergence and at the same time keep the accuracy.

The model automatically stops if the validation mean square error does not improve for 10 epochs.

Several models are built with different numbers of hidden layers and neurons. The convergence of the MSE is tested for these models, as shown in Fig. 7.2. In this work, we tested layers and neurons: 32|32, 32|32|32, 32|64|32 and 32|64|64|32, in which the numbers represent the number of neurons in one layer, for instance, 32|64|32 has the first, second and third layers of 32, 64 and 32 neurons. As suggested by Fig. 7.2, increasing the number of layers or the neurons in one layer can significantly improve the convergence of MSE. Both the 32|32 and 32|32|32 models reach the limit of the 2000 epochs which is set as default for each model, while the 32|64|32 and 32|64|64|32 has a stop of around 1600 and 1250 epochs, since the MSE triggers an early stop function. The 32|64|64|32 hidden layer structure shows a much quicker convergence than the other structures. As a consequence, the 32|64|64|32 hidden layer structure is selected for the model.

Since the electron flux density varies in a large range and trap charges have large magnitude,

normalization for the quantities is necessary to obtain a better convergence. In our training process, the normalization is applied to all samples. Assuming the variable X has mean value $\bar{X}$ and standard deviation X_{SD}, the normalization of the variable X_{norm} is calculated as:

$$X_{norm} = \frac{X - \bar{X}}{X_{SD}} \tag{7.2.1}$$

7.3 Results

If one has m attributes in the dataset, pairplot can create m $\times$ m subplots to produce the relationship between each attribute. The Fig. 7.3 is the pairplot which is constructed by 36 subfigures. The main diagram subplots are the histograms for each variable. These plots are used to give a quick inspection of the relation of the variables. In this work, since at particular external applied stress and voltage levels, the FEM model has a bad convergence, there are a few data points are missing.

From the stress-stress plot, one can directly see that the data from $\sigma_0 = -100$ MPa are less than the other. From the stress-voltage (x-y) plot it is much clear that at $\sigma_0 = -100$ MPa the data miss from the voltage 0.5 V to 2 V. At $\sigma_0 = -75$ MPa and $\sigma_0 = -150$ MPa the data also miss at some certain voltages. The Jp-Jp plot demonstrates that the hole flux is extremely small; hence, it can be neglected in the flux contribution.

Some interesting relations are demonstrated in the pairplot: (1) the J_n-Q_I plot illustrates that when electron flux starts to increase to a significant value, the trap densities are fully occupied, which indicates that the barrier height is low, as shown by the Barrier height-Q_I plot; (2) The Stress-Q_I demonstrates again that when compressive stress increases, the amount of the trap charges increase along with; (3) Voltage-Barrier height plot describes that increasing the voltage the barrier height tends to decrease; (4) corresponding to the last term, Voltage-Q_I describes that increasing the voltage results in an increase of the trap charge; (5) the barrier height-J_n plot indicates directly that a lower barrier height facilitates the electron flux.

The stresses applied in the FEM are from -250 MPa to 0 MPa, which have an interval of 25 MPa and the implemented voltages are ranging from 0 V to 2.5 V with an interval of 0.01 V. Therefore, the number of the total datasets should be 2761. Due to the lousy convergence at some implemented conditions, we have valid 2468 datasets. The valid datasets are divided that the 80% are the training set, and the rest are the test set, where the training set is the data that is used to train the model and test set are used to test if the model can predict well.

As Fig. 7.4 illustrates, the model has been trained until the automatic stopping function finds that there is no improvement in the validation MSE (also is frequently referred to as "validation loss"). In this process, 1500 epochs are set to be trained, while the model automatically stops at 1000 epochs. The train MSE ('loss') reduces dramatically in the first 200 epochs and saturate after 400 epochs. At 800 epoch, both training and validation errors are small. The small errors

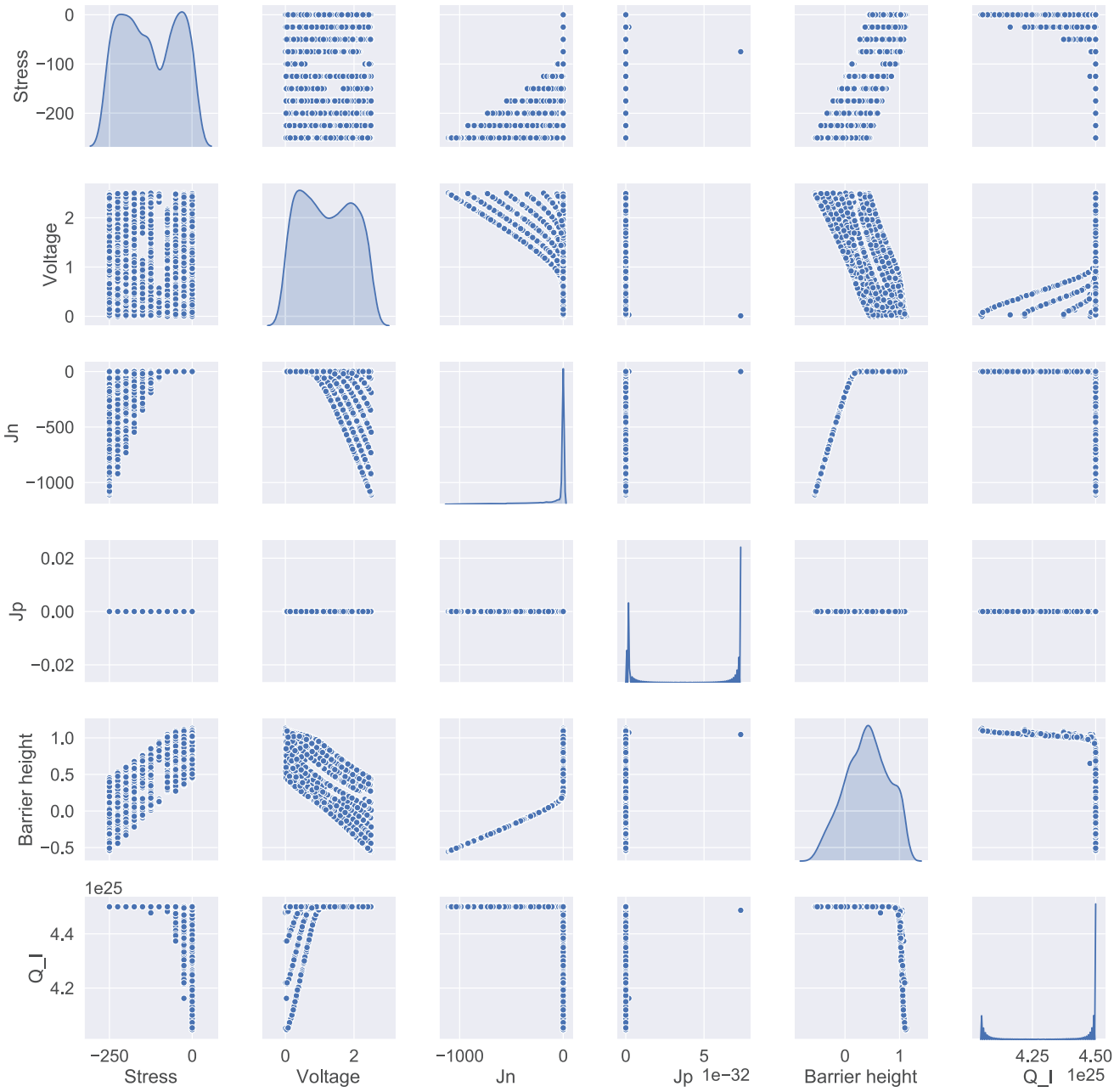

Figure 7.3: Pair plot of the quantities in machine learning. The diagonal plots which has the same x and y axes has the actual meaning that the y axis is counts.

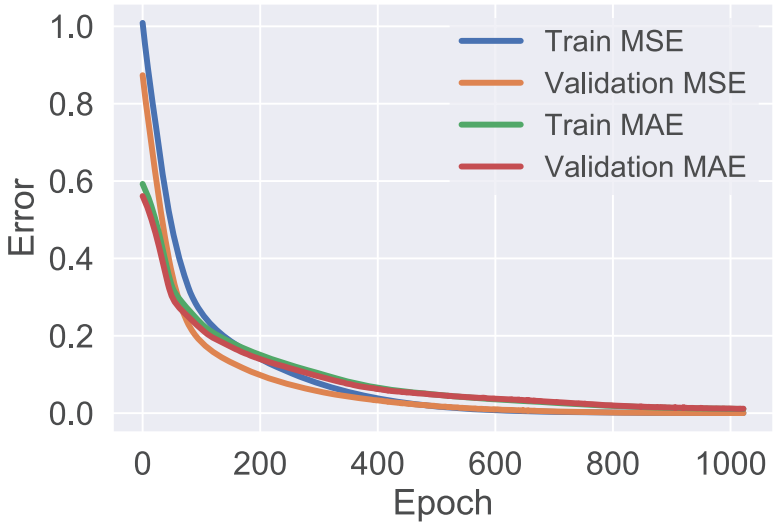

Figure 7.4: The MAE and MSE for both training and validation. The MSE and MAE cross each other at around 400 epochs, indicating that the predictions are tuned much closer to the true values.

demonstrate that the model has been trained well based on the training set, and the validation set confirms it.

Similar to MSE, the MAE drops abruptly at the beginning and has a mild decrease after around 200 epochs. One can notice from the comparison of MSE and MAE that in the early epochs, the MSE is much higher than MAE, while after 400 epochs, it is lower than MAE. This switch indicates that at the beginning of the epochs, the predictions far away from true values are tuned heavily. After 400 epochs, the predictions are much closer to the true values.

The test dataset is as the training set. Both contain inputs and true values of outputs. We use the external electric and mechanical loading from the 494 test dataset as input for the trained model. The predicted barrier height is calculated and compared with the barrier height from the test dataset (true values). The scattered points are created that x values and the y values are the true and predicted barrier heights, respectively, describing in Fig. 7.5. The scattered points lie around the line $y = x$, indicating that the model can well predict the barrier height. We calculate the prediction error by:

$$prediction\ error = prediction - true\ value \tag{7.3.1}$$

The histogram is plotted for the barrier height relative error, as shown in Fig 7.6 and shows nearly a Gaussian distribution, which is as expected since the error obeys Central Limit Theorem.

The small electron flux comparison for the predictive and true values is illustrated in Fig. 7.7a. It shows that with some external mechanical and electrical loadings, the sample tends to have zero electron flux due to the varistor effect. However, it can be observed that the true value of

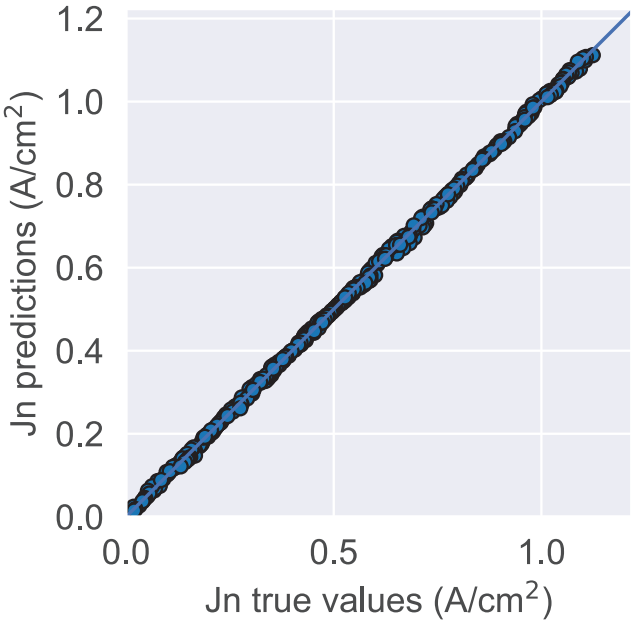

Figure 7.5: Using the test dataset to verify if the model can predict the barrier height well. With the same external electrical and mechanical loadings, the prediction and true values are almost the same, resulting in that the scatter points lying on the line $y = x$.

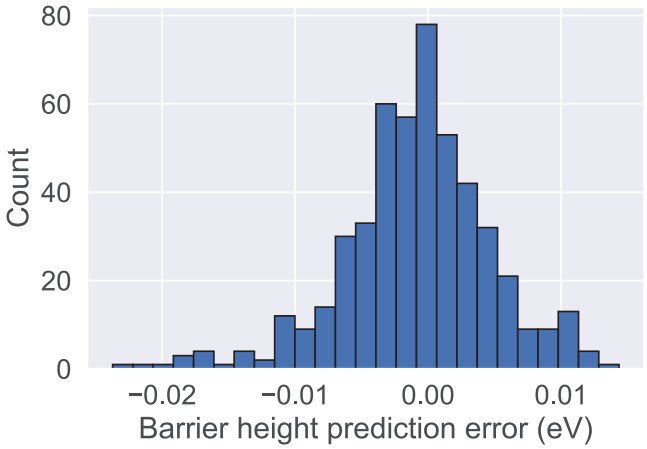

Figure 7.6: The histogram of the barrier height prediction error distribution.

zero is not well predicted. The reason for the worse prediction is assumed that the electron flux spans a too large range from -1100 A/cm^2 to 0 A/cm^2 and its high nonlinearity.

However, on a larger scale, the electron flux predictions and the true values match each other very well, indicating that the model has good performance when the electron flux is large, as shown in Fig. 7.7b.

The histogram of the electron flux prediction error demonstrates a Gaussian distribution as shown in Fig. 7.8. The model has the prediction error within 12, indicating on the large scale, the

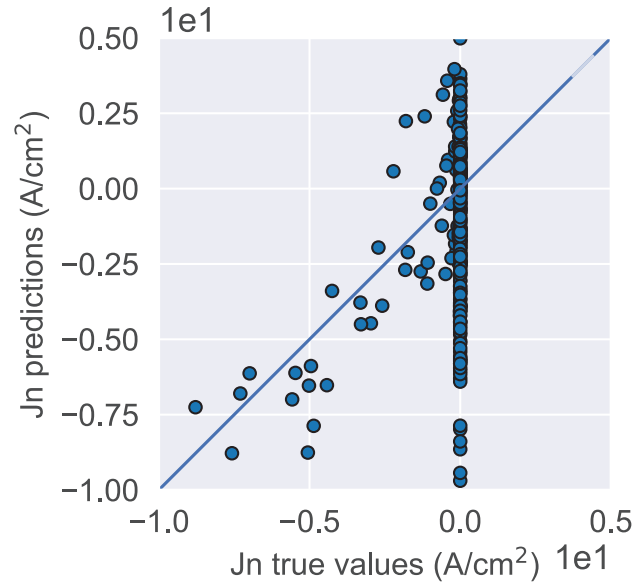

(a) Prediction and true value comparison for small electron flux.

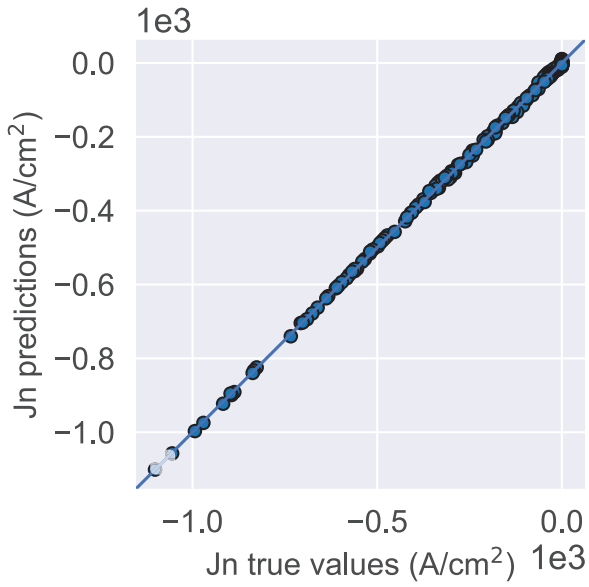

(b) Prediction and true value comparison for whole scale electron flux.

Figure 7.7: Accuracy of the electron flux prediction.

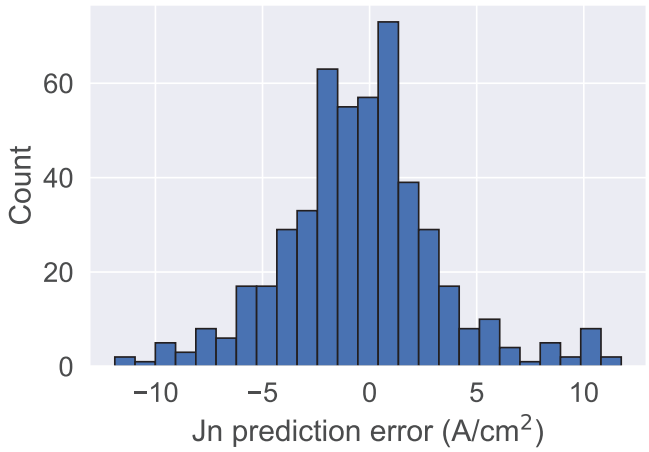

Figure 7.8: The histogram of the electron flux prediction error distribution.

model performs quite well.

Fig. 7.9 shows the prediction and true value comparison for trap charge. Unlike the electron flux density, although trap charge has large value, the numbers are in the same magnitude.

The histogram of the error of the trap charge prediction is shown in Fig. 7.10. Still, the errors have an Gaussian distribution. Fig. 7.10 illustrates that the prediction errors are among 1×10^{23}, which is within 1% of the magnitude of trap charges (1×10^{25}).

A comparison of the model performance on trap charges with different numbers of hidden layers and neurons is made in Fig. 7.11. Since the MSE for $32|32$ does not reach zero, the predictions do

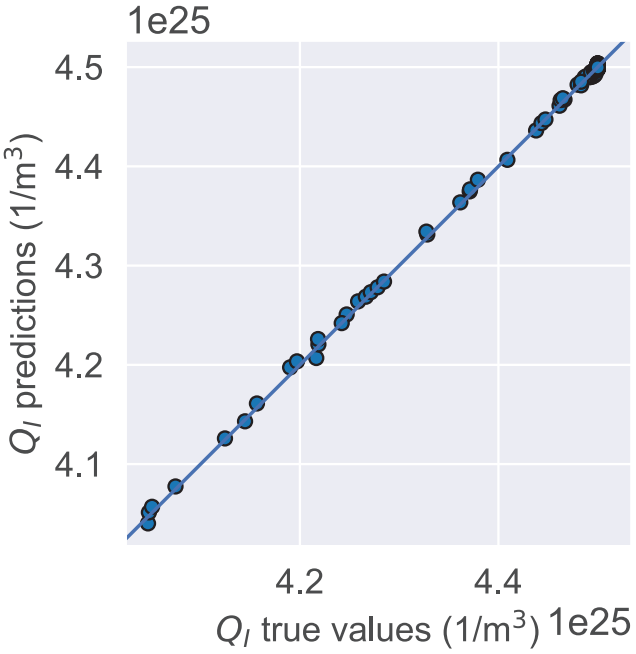

Figure 7.9: Prediction and true value comparison for trap charge densities.

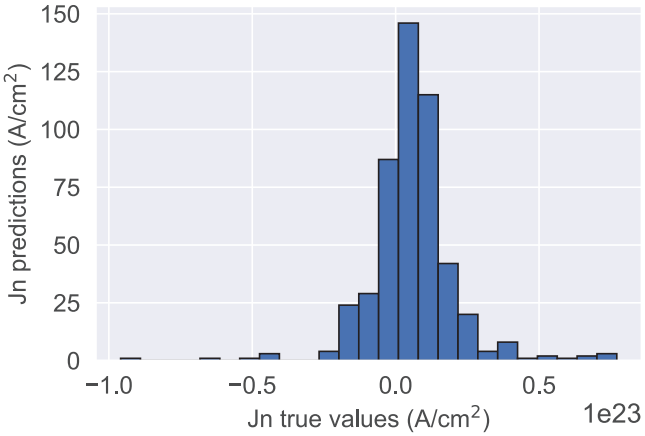

Figure 7.10: The histogram of the trap charge prediction error distribution.

not match true values precisely. The comparison of Fig. 7.11 (a) and (b) suggests that with the same epochs, increasing layers can increase the accuracy. Fig. 7.11 (b) and (c) demonstrate that increasing the neurons can improve accuracy. Fig. (c) and (d) exhibit that even the MSE of both $32|64|32$ and $32|64|64|32$ reduces to an early stop, the model with layer structure $32|64|64|32$ is more accurate than $32|64|32$, especially at large trap charge values. In fact, the MSE of $32|64|64|32$ and $32|64|32$ could be reduced to the lowest value of 0.00042003 and 0.000672407 respectively, suggesting that the number of layers and neurons is critical for the precision of the models.

The python code which builds the neural network model can be found in Appendix 9.4

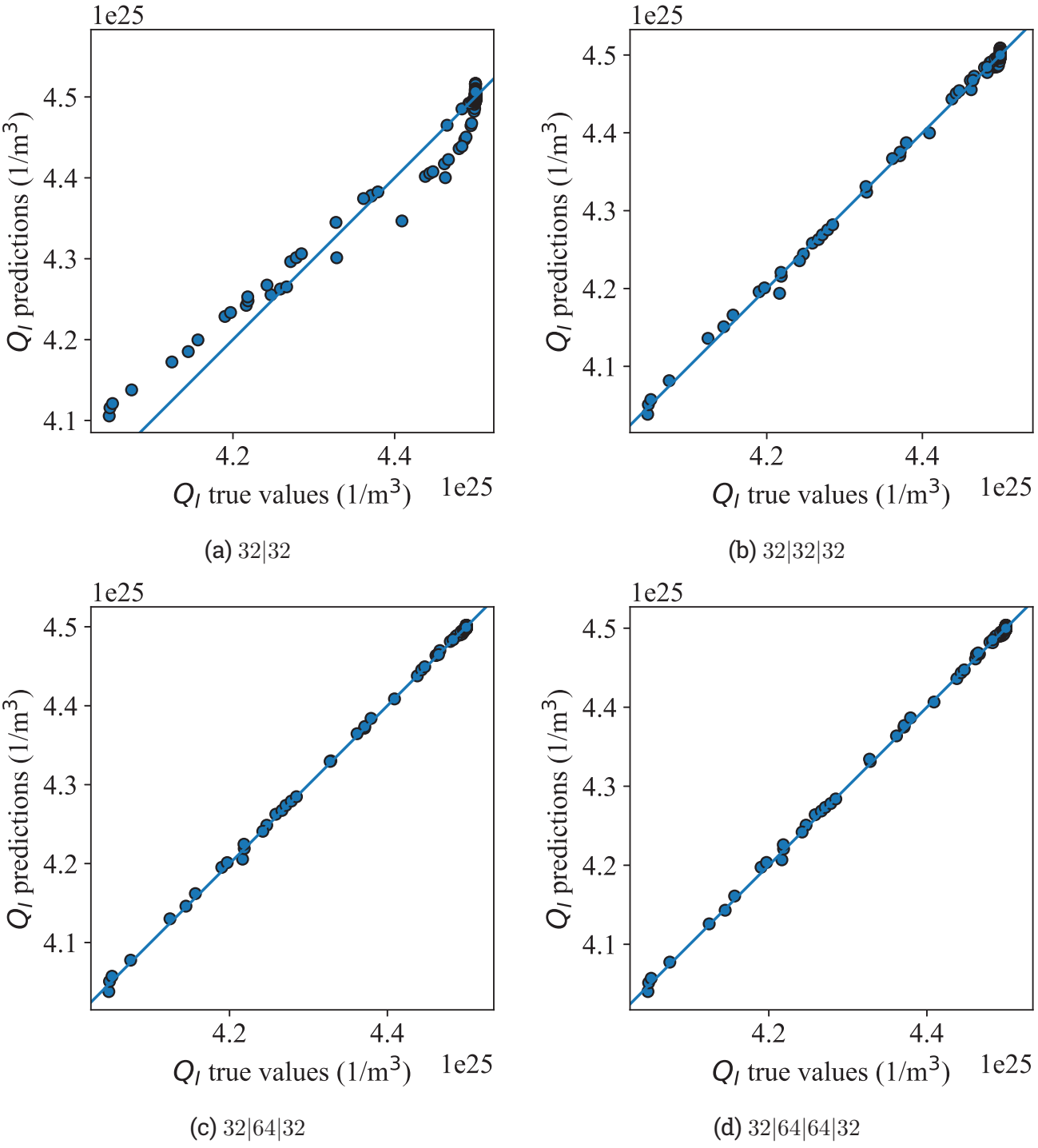

(a) 32|32 (b) 32|32|32

(c) 32|64|32 (d) 32|64|64|32

Figure 7.11: Comparison of the accuracy of the trap charge predictions from different models

8 Concluding remarks and outlook

One achievement in this work is to consider the internal electric field in the phenomenological model. This field brings two effects; one is that it alters the piezoelectric charge at GB; the other is that it creates space piezoelectric charge in the depletion region. Due to the large electric field at the GB and its high gradient in the depletion region, the internal field reduces the barrier height depending on the dimensionless coefficient of f. If $f = 0$, the MPM can reduce to PM. In this work, according to the parameters given in Table 5.1, the barrier height is reduced for 12.8% for ZnO. The consequences of this effect also include that: firstly, the barrier height becomes less sensitive to mechanical stress and applied voltage; secondly, the breakdown happens at lower stress (head-to-head configuration) and bias voltage state.

The PM is widely used to fit the experimental data of barrier heights to estimate parameters on grain boundary charge densities. If the MPM is applied to fit the same experimental data, the determined grain boundary trap charge densities are expected to be higher than those determined by the PM.

The second model developed in this work is FEM, which automatically takes the inverse piezoelectric effect of the internal electric field on the barrier height into account. The results of FEM and PM do not match exactly with each other. The reasons stem from three main points. Firstly, at $T = 300$ K, the ionized donor states from FEM results show a trapezoidal shape rather than a box shape as assumed in the MPM at $T = 0$ K. Secondly, in the FEM, there are no additional assumptions for the potential at the edge of the depletion region. Thirdly, the width of the GB for the FEM is 1 nm rather than 0 nm assumed by the MPM. For these reasons, the FEM is physically more meaningful. The FEM demonstrates that when considering not perfect z-axis aligned bicrystal, the full rotation of the parameter tensors needs to be considered. The corrections for the MPM concerning such crystal rotation is proposed.

The FEM built in this work uses quasi-Fermi energy rather than charge densities as degrees of freedom, which is more convenient for the calculation and physically more fundamental. The flux comparison of MPM, PM and FEM demonstrates that considering the internal electric field for the phenomenological model is necessary and has a considerable influence in calculating the flux. Unlike the MPM, in FEM, the barrier height can reach below 0 eV, and the flux breakdown is not relevant to the sudden drop of the barrier height. On the other hand, breakdown of the

flux is controlled by the gradient of the band structure, and it happens always accompanied by a minimal barrier height.

For future development, several interesting studies could be continued.

For the FE model, the metal-semiconductor interfaces could be added on both sides of the bicrystal. In this way, the model for the bicrystal piezotronic FET can be completed. It has to be noticed that the single Schottky barrier is mainly aroused from the difference from the Fermi levels between metal and semiconductors. From this model, one can study between the double and single Schottky barriers, which one at which external electrical and mechanical loading dominants the charge carrier transportation. This model can thus guide the selection of the contact model to optimize the ON/OFF ratio.

Another research possibility is to extend the FE calculation to multigrain. It can validate if the current prefer some low resistance channels. This study needs large computational resources, and the DOS at the GBs needs to be carefully selected.

The reverse flexoelectric effect can also be considered. It is aroused by the high gradient of the electric field in the depletion region. Though according to the research done by Zhang et al.[101], this effect might have very little influence comparing to the piezoelectric effect.

Temperature study is also an interesting topic since the temperature can increase when the current goes through the devices. Though the phenomenological model done by Baraki [20] suggested that the sensitivity of the resistivity to the external stress is decreased by increasing the temperature. It is still worth to explore the band energy profile with the FE method.

Further studies can even be extended to optoelectronics by adjusting the generation rate at the GB. In this way, new applications can be open for this FE model.

Lastly, the inverse piezoelectric effect can have a general impact on the III-V or II-VI semiconductor junction devices, e.g. the thin GaN films, AlGaN/AlN/GaN diodes, since they are also piezoelectric materials. Therefore, more investigations could be made on those junction devices.

9 Appendix

9.1 DERIVATION OF THE ROTATION MATRIX FOR POLARIZATION

A Voigt notation is a way to reduce the order of a symmetric tensors. For instance the subscript of the second order tensor σ_{ij} is denoted as

$$11 \to 1 \quad 22 \to 2 \quad 33 \to 3 \quad 23 \to 4 \quad 31 \to 5 \quad 12 \to 6 \tag{9.1.1}$$

where i and j varies between 1 and 3. Therefore, following the Voigt notation, the stress matrix can be expressed as $\boldsymbol{\sigma}_0 = [\sigma_1, \sigma_2, \sigma_3, \sigma_4, \sigma_5, \sigma_6]^{\mathrm{T}}$.

Consider the matrix form of Eq. 4.2.5:

$$\mathbf{P}_d = \mathbf{e}\mathbf{C}^{-1}\boldsymbol{\sigma}_0 + \mathbf{e}\mathbf{C}^{-1}\mathbf{e}^{\mathrm{T}}\mathbf{E} \tag{9.1.2}$$

Using the traditional rotation matrix $\mathbf{Q}$, the rotated polarization $\mathbf{P}'_d$ is,

$$\mathbf{P}'_d = \mathbf{Q}\mathbf{P}_d = \mathbf{Q}\mathbf{e}\mathbf{C}^{-1}\boldsymbol{\sigma}_0 + \mathbf{Q}\mathbf{e}\mathbf{C}^{-1}\mathbf{e}^{\mathrm{T}}\mathbf{E} \tag{9.1.3}$$

We denote the rotated $\boldsymbol{\sigma}_0$ and $\mathbf{E}$ as $\boldsymbol{\sigma}'_0$ and $\mathbf{E}'$, then,

$$\boldsymbol{\sigma}'_0 = \mathbf{A}\boldsymbol{\sigma}_0 \tag{9.1.4}$$

$$\mathbf{E}' = \mathbf{Q}\mathbf{E} \tag{9.1.5}$$

where A is the rotation matrix specifically for the Voigt noted second order tensor (e.g. σ_{ij}). Therefore, Eq. 9.1.3 is rewritten as:

$$M \tag{9.1.6}$$

If one need to compute $\mathbf{P}'_d$ with full anisotropy with $\boldsymbol{\sigma}'_0$ and $\mathbf{E}'$, the matrix $\mathbf{Q}\mathbf{e}\mathbf{C}^{-1}\boldsymbol{A}^{-1}$ and $\mathbf{Q}\mathbf{e}\mathbf{C}^{-1}\mathbf{e}^{\mathrm{T}}\boldsymbol{Q}^{-1}$ need to be considered.

9.2 DERIVATION OF THE ROTATION MATRIX FOR THE VOIGT STRESS TENSOR

A rotation matrix is a matrix that performs rotation for a quantity in space. In 3D space, it contains three basic matrices which take care of the rotation performance anticlockwise along the x-, y- and z-axis:

$$R_x(\theta_x) = \begin{bmatrix} 1 & 0 & 0 \\ 0 & \cos\theta_x & -\sin\theta_x \\ 0 & \sin\theta_x & \cos\theta_x \end{bmatrix}, \tag{9.2.1}$$

$$R_y(\theta_y) = \begin{bmatrix} \cos\theta_y & 0 & \sin\theta_y \\ 0 & 1 & 0 \\ -\sin\theta_y & 0 & \cos\theta_y \end{bmatrix}, \tag{9.2.2}$$

$$R_z(\theta_z) = \begin{bmatrix} \cos\theta_z & -\sin\theta_z & 0 \\ \sin\theta_z & \cos\theta_z & 0 \\ 0 & 0 & 1 \end{bmatrix}, \tag{9.2.3}$$

in which the θ_x, θ_y and θ_z are the angles that the quantity rotate along the 3 axes. The superimposed rotation is then

$$R = R_x(\theta_x)R_y(\theta_y)R_z(\theta_z). \tag{9.2.4}$$

If the rotated stress tensor is denoted as σ'_{mn} and the original one as σ_{ij}, the relationship between σ'_{mn} and σ_{ij} is expressed as:

$$\sigma'_{mn} = R_{mi}R_{nj}\sigma_{ij}, \tag{9.2.5}$$

where R_{mi} and R_{nj} are the rotation matrices for the tensor component i and j. Considering the Voigt notation from Eq. 9.1.1, the σ'_{mn} becomes σ'_p and σ_{ij} becomes σ_q. We have now:

$$\sigma'_p = A_{pq}\sigma_q. \tag{9.2.6}$$

If we fix q=1, then $i = 1$ and $j = 1$. The matrix A is A_{p1} and R_{mi} and R_{nj} becomes R_{m1} and R_{n1}. The Voigt version of $R_{m1}R_{n1}$ is then exactly the 1st column of A_{pq}, in which the $mn \to p$ following or the order from Eq. 9.1.1. Consequently, the 2nd and 3rd column are composed of $R_{m2}R_{n2}$ and

$R_{m3}R_{n3}$ respectively.

When $q = 4$, the $i = 2 \quad j = 3$ or $i = 3 \quad j = 2$, then the 4th column of A_{pq} is $R_{m2}R_{n3} + R_{m3}R_{n2}$. Following the same manner, the 5th and 6th column are consist of $R_{m1}R_{n3} + R_{m3}R_{n1}$ and $R_{m2}R_{n1} + R_{m1}R_{n2}$. Therefore, the full A_{qp} is:

$$\begin{bmatrix} R_{11}^2 & R_{12}^2 & R_{13}^2 & 2R_{12}R_{13} & 2R_{11}R_{13} & 2R_{11}R_{12} \\ R_{21}^2 & R_{22}^2 & R_{23}^2 & 2R_{22}R_{23} & 2R_{21}R_{23} & 2R_{21}R_{22} \\ R_{31}^2 & R_{32}^2 & R_{33}^2 & 2R_{33}R_{32} & 2R_{31}R_{33} & 2R_{31}R_{32} \\ R_{11}R_{21} & R_{12}R_{22} & R_{13}R_{23} & R_{12}R_{23} + R_{13}R_{22} & R_{11}R_{23} + R_{13}R_{21} & R_{11}R_{22} + R_{12}R_{21} \\ R_{21}R_{31} & R_{22}R_{32} & R_{23}R_{33} & R_{22}R_{33} + R_{23}R_{32} & R_{21}R_{33} + R_{23}R_{31} & R_{21}R_{32} + R_{22}R_{31} \\ R_{31}R_{11} & R_{32}R_{12} & R_{33}R_{13} & R_{32}R_{13} + R_{33}R_{12} & R_{31}R_{13} + R_{33}R_{11} & R_{31}R_{12} + R_{32}R_{11} \end{bmatrix} \tag{9.2.7}$$

9.3 NORMALIZATION

Displacement	$x^* = \frac{x}{L}$
Gradient	$\nabla^* = \frac{\partial}{\partial x^*} = L\frac{\partial}{\partial x} = L\nabla$
Stress	$\sigma^* = \frac{\sigma}{\sigma^0} \quad (\sigma^0 = qV_{th}N)$
Stress	$\sigma^* = \mathbf{C}^* \, \mathbf{S}^* - \mathbf{e}^{\mathbf{T}^*}\mathbf{E}^* = \mathbf{C}^* \, \mathbf{S}^* + \mathbf{e}^{T^*}\nabla^*\phi^*$
Force balance	$\nabla^*\sigma^* = \frac{\partial\sigma^*}{\partial x^*} = \frac{\partial\frac{\sigma}{\sigma^0}}{\partial\frac{x}{L}} = \frac{L}{\sigma^0}\nabla\sigma$
Strain	$S^* = S$
Elasticity constant	$C^* = \frac{C}{\sigma^0}$
Piezoelectric constant	$e^* = \frac{1}{LqN}e$
Potential/Voltage	$\phi^* = \frac{\phi}{V_{th}}$
Electric field	$E^* = -\nabla^*\phi^* = -\frac{L}{V_{th}}\nabla\phi = \frac{L}{V_{th}}E$
Electric displacement	$D^* = \frac{D}{D^0} \; (D^0 = qLN)$
Gauss's law in a dielectric	$\nabla^* \cdot D^* = \frac{L}{D^0}\nabla \cdot D \quad (D^0 = qLN)$
Charge density	$\rho^* = \frac{\rho}{qN}$
Electron density	$n^* = \frac{n}{N}$
Hole density	$p^* = \frac{p}{N}$
Time derivative of electrons	$\dot{n}^* = \frac{\partial n^*}{\partial t^*} = \frac{t^0}{N}\dot{n}$
Time derivative of electrons	$\dot{n}^* = \frac{1}{q^*}\nabla^* \cdot J_n^* - U_{np}^* = 0$
Electron flux	$J_n^* = \frac{t^0}{LeN}J_n$
Electron flux	$J_n^* = \mu_n^* n^* \nabla^* \mathscr{E}_{Fn}^*$
Time derivative of holes	$\dot{p}^* = \frac{\partial p^*}{\partial t^*} = \frac{t^0}{N}\dot{p}$
Time derivative of holes	$\dot{p}^* = \frac{1}{q^*}\nabla^* \cdot J_p^* - U_{np}^* = 0$
Hole flux	$J_p^* = \frac{t^0}{LeN}J_p$
Hole flux	$J_p^* = \mu_p^* p^* \nabla^* \mathscr{E}_{Fp}^*$

Generation and recombination rate	$U_{np}^* = \frac{p^* n^* - n_i^{*2}}{\tau_p^*(n^* + n_i^*) + \tau_n^*(p^* + p_i^*)}$
Generation and recombination rate	$U_{np}^* = \frac{t^0}{N} U_{np}$
Electron carrier life time	$\tau_n^* = \frac{\tau_n}{t^0}$
Hole carrier life time	$\tau_p^* = \frac{\tau_p}{t^0}$
Electron mobility	$\mu_n^* = \frac{t^0 kT}{eL^2} \mu_n$
Hole mobility	$\mu_p^* = \frac{t^0 kT}{eL^2} \mu_p$
Electron quasi Fermi energy	$\mathscr{E}_{Fn}^* = \frac{\mathscr{E}_{Fn}}{k_B T}$
Hole quasi Fermi energy	$\mathscr{E}_{Fp}^* = \frac{\mathscr{E}_{Fp}}{k_B T}$

9.4 Python code for neural networks

```
# -*- coding: utf-8 -*-
"""
Created on Wed Oct 16 11:18:17 2019

@author: wiseh
"""

from __future__ import absolute_import, division, print_function, unicode_literals
import pathlib
import numpy as np
import matplotlib.pyplot as plt
import matplotlib
import pandas as pd
import seaborn as sns
import tensorflow as tf
from tensorflow import keras
from tensorflow.keras import layers
from matplotlib.ticker import FormatStrFormatter

plt.rcParams["font.family"] = "Times New Roman"
matplotlib.rcParams.update({'font.size': 15})
#------------------color configuration----------------------#
# These are the "Tableau 20" colors as RGB.
tableau20 = [(31, 119, 180), (174, 199, 232), (255, 127, 14), (255, 187, 120),
             (44, 160, 44), (152, 223, 138), (214, 39, 40), (255, 152, 150),
             (148, 103, 189), (197, 176, 213), (140, 86, 75), (196, 156, 148),
             (227, 119, 194), (247, 182, 210), (127, 127, 127), (199, 199, 199),
             (188, 189, 34), (219, 219, 141), (23, 190, 207), (158, 218, 229)]

```

```
# Scale the RGB values to the [0, 1] range, which is the format matplotlib accepts.
for i in range(len(tableau20)):
    r, g, b = tableau20[i]
    tableau20[i] = (r / 255., g / 255., b / 255.)
#------------------color configuration---------------------#
column_names = ['Stress','Voltage','Jn','Jp','Barrier height','Q_I']
raw_dataset = pd.read_excel('RawData_Machine.xlsx', names=column_names,sheet_name='Sheet1')

FEM_failed = pd.read_excel('FEM_failed_data.xlsx', names=['Stress','Voltage'], sheet_name='Sheet1')

dataset = raw_dataset.copy()

#print(dataset.tail())
train_dataset = dataset.sample(frac=0.8,random_state=1)
test_dataset = dataset.drop(train_dataset.index)
#----------plot the pair plot-----------#
plt.figure()
axes = plt.gca()
sns.set(font_scale=1.5)
sns.pairplot(train_dataset[['Stress','Voltage','Jn','Jp','Barrier height','Q_I']], diag_kind='kde')
#axes.plot(label='big')
plt.savefig('pairplot.pdf',transparent=False,bbox_inches='tight')
plt.show()
#----------plot the pair plot-----------#
train_stats = train_dataset.describe()
train_stats.pop("Jn")
train_stats.pop("Jp")
train_stats.pop("Barrier height")
train_stats.pop("Q_I")
train_stats = train_stats.transpose()
train_labels_Jn = train_dataset.pop('Jn')
test_labels_Jn = test_dataset.pop('Jn')
train_labels_Jp = train_dataset.pop('Jp')
test_labels_Jp = test_dataset.pop('Jp')
train_labels_PhiB = train_dataset.pop('Barrier height')
test_labels_PhiB = test_dataset.pop('Barrier height')
train_labels_TrapChar = train_dataset.pop('Q_I')
test_labels_TrapChar = test_dataset.pop('Q_I')
#train_labels=pd.concat([train_labels_PhiB,train_labels_Jn,train_labels_Jp,train_labels_TrapChar],axis=1)
```

```
#test_labels=pd.concat([test_labels_PhiB,test_labels_Jn,test_labels_Jp,
    test_labels_TrapChar],axis=1)
train_labels=pd.concat([train_labels_PhiB,train_labels_Jn,train_labels_TrapChar],
    axis=1)
test_labels=pd.concat([test_labels_PhiB,test_labels_Jn,test_labels_TrapChar],axis
    =1)

FEM_failed_stats = FEM_failed.describe()
FEM_failed_stats = FEM_failed_stats.transpose()
train_labels_stats=train_labels.describe()
train_labels_stats=train_labels_stats.transpose()
test_labels_stats=test_labels.describe()
test_labels_stats=test_labels_stats.transpose()
#%%

def norm(x,stats):
  return (x - stats['mean']) / stats['std']
def anti_norm(x_norm,stats):
  return (x_norm * stats['std'] + stats['mean'])
normed_train_data = norm(train_dataset,train_stats)
normed_test_data = norm(test_dataset,train_stats)
normed_FEM_failed= norm(FEM_failed,train_stats)                    # norm   norm
normed_test_labels = norm(test_labels,train_labels_stats)
normed_train_labels = norm(train_labels,train_labels_stats)

aaaaaaaa=normed_train_labels.describe()

def build_model():
  model = keras.Sequential([
    layers.Dense(32, activation=tf.nn.relu, input_shape=[len(train_dataset.keys())
    ]),
    layers.Dense(64, activation=tf.nn.relu),
    layers.Dense(64, activation=tf.nn.relu),
    layers.Dense(32, activation=tf.nn.relu),
    layers.Dense(3)
  ])

  optimizer = tf.keras.optimizers.RMSprop(0.00001)

  model.compile(loss='mean_squared_error',
                optimizer=optimizer,
                metrics=['mean_absolute_error', 'mean_squared_error'])
  return model

model = build_model()
```

```
model.summary()

example_batch = normed_train_data[:10]
example_result = model.predict(example_batch)

# Display training progress by printing a single dot for each completed epoch
class PrintDot(keras.callbacks.Callback):
  def on_epoch_end(self, epoch, logs):
    if epoch % 100 == 0: print('')
    print('.', end='')

EPOCHS = 2000

def plot_history(history):
  hist = pd.DataFrame(history.history)
  hist['epoch'] = history.epoch

  plt.figure()
  plt.xlabel('Epoch')
  plt.ylabel('MAE')
  plt.plot(hist['epoch'], hist['mean_absolute_error'],
           label='Train',linewidth=3.0)
  plt.plot(hist['epoch'], hist['val_mean_absolute_error'],
           label = 'Validation',linewidth=3.0)
#  plt.ylim([0,5])
  leg=plt.legend(prop={'size':15},loc=1)
  leg.get_frame().set_linewidth(0.0)
  plt.savefig('MeanAbsError.pdf',transparent=False,bbox_inches='tight')
  plt.close()

  plt.figure()
  plt.xlabel('Epoch')
  plt.ylabel('MSE')
  plt.plot(hist['epoch'], hist['mean_squared_error'],
           label='Train',linewidth=3.0)
  plt.plot(hist['epoch'], hist['val_mean_squared_error'],
           label = 'Validation',linewidth=3.0)
#  plt.ylim([0,20])
  leg=plt.legend(prop={'size':15},loc=1)
  leg.get_frame().set_linewidth(0.0)
  plt.savefig('MeanSquareError.pdf',transparent=False,bbox_inches='tight')
  plt.close()

  plt.figure()
  plt.xlabel('Epoch')
```

```
  plt.ylabel('Error')
  plt.plot(hist['epoch'], hist['mean_squared_error'],
           label='Train MSE',linewidth=3.0)
  plt.plot(hist['epoch'], hist['val_mean_squared_error'],
           label = 'Validation MSE',linewidth=3.0)
  plt.plot(hist['epoch'], hist['mean_absolute_error'],
           label='Train MAE',linewidth=3.0)
  plt.plot(hist['epoch'], hist['val_mean_absolute_error'],
           label = 'Validation MAE',linewidth=3.0)
#  plt.ylim([0,20])
  leg=plt.legend(prop={'size':15},loc=1)
  leg.get_frame().set_linewidth(0.0)
  plt.savefig('MSE_MAE.pdf',transparent=False,bbox_inches='tight')
  plt.show()
  plt.close()

#-------------load the model--------------#
model = keras.models.load_model('32_64_64_32.h5')

#----------activate the model begin--------------#
#model = build_model()
## The patience parameter is the amount of epochs to check for improvement
## train the model
#early_stop = keras.callbacks.EarlyStopping(monitor='val_loss', patience=10)
#history = model.fit(normed_train_data,normed_train_labels, epochs=EPOCHS,
#                    validation_split = 0.2, verbose=0, callbacks=[early_stop,
    PrintDot()])
#model.save('my_model.h5')
#plot_history(history)
#hist = pd.DataFrame(history.history)
#hist['epoch'] = history.epoch
#hist.tail()
#----------activate the model end--------------#

loss, mae, mse = model.evaluate(normed_test_data, normed_test_labels, verbose=0)

print("Testing set Mean Abs Error: {:5.2f} Barrier height".format(mae))


normed_test_predictions = model.predict(normed_test_data)
#.flatten()
normed_prediction = model.predict(normed_FEM_failed)
#.flatten()
normed_test_predictions = pd.DataFrame(normed_test_predictions,index=
    normed_test_data.index.values,columns=['Barrier height','Jn','Q_I'])
```

```
normed_prediction = pd.DataFrame(normed_prediction,index=normed_FEM_failed.index.
    values,columns=['Barrier height','Jn','Q_I'])
test_predictions=anti_norm(normed_test_predictions,train_labels_stats)
prediction=anti_norm(normed_prediction,train_labels_stats)


#print (normed_prediction[:,0])
#print (normed_prediction[1])
##print (normed_test_labels['Barrier height'])
#
plt.figure()
plt.scatter(test_labels['Barrier height'], test_predictions['Barrier height'],
    linewidths=1,edgecolors='black',c=tableau20[0])
plt.xlabel('Barrier height true values (eV)')
plt.ylabel('Barrier height predictions (eV)')
plt.axis('equal')
plt.axis('square')
plt.xlim([0,plt.xlim()[1]])
plt.ylim([0,plt.ylim()[1]])
_ = plt.plot([-100, 100], [-100, 100])
ax = plt.axes()
plt.xlabel(r'Jn true values (A/cm$^2$)',fontsize=15)
plt.ylabel(r'Jn predictions (A/cm$^2$)',fontsize=15)
ax.tick_params(axis='both', which='major', labelsize=15)
plt.savefig('DoesItMatch_BH.pdf',transparent=False,bbox_inches='tight')
plt.close()

plt.figure()
axes = plt.gca()
#axes.set_xlim([-0.05,0.05])
error = test_predictions['Barrier height'] - test_labels['Barrier height']
plt.hist(error, bins = 25, edgecolor='black', linewidth=1)
plt.xlabel("Barrier height prediction error (eV)")
_ = plt.ylabel("Count")
plt.savefig('Histgram_BH.pdf',transparent=False,bbox_inches='tight')
plt.close()

plt.figure()
plt.scatter(test_labels['Jn'], test_predictions['Jn'],linewidths=1,edgecolors='
    black',c=tableau20[0])
plt.axis('equal')
plt.axis('square')
plt.ticklabel_format(style='sci', scilimits=(0,00))
ax = plt.axes()
plt.xlabel(r'Jn true values (A/cm$^2$)',fontsize=15)
```

```
plt.ylabel(r'Jn predictions (A/cm$^2$)',fontsize=15)
ax.tick_params(axis='both', which='major', labelsize=15)
x = np.linspace(plt.xlim()[0], plt.xlim()[1], 10000)
ax.plot(x,x)
#plt.xlim([0,plt.xlim()[1]])
#plt.ylim([0,plt.ylim()[1]])
#print (plt.xlim()[0])
#print (plt.xlim()[1])
#print (plt.ylim()[0])
#print (plt.ylim()[1])
#_ = plt.plot([-100, 100], [-100, 100])
leg=plt.legend(prop={'size':15},loc=3)
leg.get_frame().set_linewidth(0.0)
plt.savefig('DoesItMatch_Jn.pdf',transparent=False,bbox_inches='tight')
plt.close()

plt.figure()
plt.scatter(test_labels['Jn'], test_predictions['Jn'],linewidths=1,edgecolors='
    black',c=tableau20[0])
plt.axis('equal')
plt.axis('square')
ax = plt.axes()
x = np.linspace(plt.xlim()[0], plt.xlim()[1], 10000)
ax.plot(x,x)
plt.xlim([-10,5])
plt.ylim([-10,5])
#ax.xaxis.set_major_formatter(FormatStrFormatter('%.1f'))
#ax.yaxis.set_major_formatter(FormatStrFormatter('%.1f'))
plt.xlabel(r'Jn true values (A/cm$^2$)',fontsize=15)
plt.ylabel(r'Jn predictions (A/cm$^2$)',fontsize=15)
ax.tick_params(axis='both', which='major', labelsize=15)
plt.ticklabel_format(style='sci', scilimits=(0,00))
#_ = plt.plot([-100, 100], [-100, 100])
leg=plt.legend(prop={'size':15},loc=1)
leg.get_frame().set_linewidth(0.0)
plt.savefig('DoesItMatch_Jn_small_scale.pdf',transparent=False,bbox_inches='tight'
    )
plt.close()

plt.figure()
axes = plt.gca()
#plt.xlim([-100,100])
#axes.set_xlim([-0.05,0.05])
error = test_predictions['Jn'] - test_labels['Jn']
plt.hist(error, bins = 25, edgecolor='black', linewidth=1)
```

```
plt.xlabel(r"Jn prediction error (A/cm$^2$)")
_ = plt.ylabel("Count")
plt.savefig('Histgram_Jn.pdf',transparent=False,bbox_inches='tight')
plt.close()

plt.figure()
plt.scatter(test_labels['Q_I'], test_predictions['Q_I'],linewidths=1,edgecolors='
    black',c=tableau20[0])
plt.xlabel(r'$Q_I$ true values (1/m$^3$)',fontsize=15)
plt.ylabel(r'$Q_I$ predictions (1/m$^3$)',fontsize=15)
plt.axis('equal')
plt.axis('square')
ax = plt.axes()
x = np.linspace(plt.xlim()[0], plt.xlim()[1], 10000)
ax.plot(x,x);
#plt.xlim([0,plt.xlim()[1]])
#plt.ylim([0,plt.ylim()[1]])
#_ = plt.plot([-100, 100], [-100, 100])
ax.tick_params(axis='both', which='major', labelsize=15)
plt.savefig('DoesItMatch_TrapChar.pdf',transparent=False,bbox_inches='tight')
plt.close()

plt.figure()
#plt.grid(b=False)
#plt.style.use('classic')
axes=plt.gca()
axes.get_yaxis()
axes.get_xaxis()
#plt.tick_params(top='off',right='off')
error = test_predictions['Q_I'] - test_labels['Q_I']
plt.hist(error, bins = 25, edgecolor='black', linewidth=1)
plt.xlabel(r"$Q_I$ prediction error (1/m$^3$)")
plt.ylabel("Count")
ax = plt.axes()
plt.xlabel(r'Jn true values (A/cm$^2$)',fontsize=15)
plt.ylabel(r'Jn predictions (A/cm$^2$)',fontsize=15)
ax.tick_params(axis='both', which='major', labelsize=15)
plt.savefig('Histgram_TrapChar.pdf',transparent=False,bbox_inches='tight')
plt.close()
```

Curriculum vitae

Personal details

Name	Ziqi Zhou
Date of birth	21.05.1989
Place of birth	Xianyang China
Nationality	Chinese

Education

10/2016-05/2020

Fachbereich Material und Geowissenschaften, Technische Universität Darmstadt, Germany
Doctoral student

03/2013-07/2016

Fachbereich Material und Geowissenschaften, Technische Universität Darmstadt, Germany
Master of Science

07/2008-06/2012

School of Materials Science and Engineering, Southeast university, China
Bachelor of Science

Work experience

05/2015-10/2015 Fraunhofer IWM, Germany, research assistant

Publications

Xu B X, Zhou Z Q, Keil P, et al. An extended grain boundary barrier height model including the impact of internal electric field[J]. AIP Advances, 2018, 8(11): 115126.

Zhou Z Q, Taylor K, Gjonaj E, et al. Finite element simulations on piezoelectric modulation of ZnO grain boundary barrier height[J]. Journal of Applied Physics, 2019, 126(20): 205101.

Taylor K A, Gjonaj E, Zhou Z, et al. Mesoscopic modeling of the mechanically tunable electrical conductivity of ZnO varistors[J]. Journal of Applied Physics, 2020, 127(15): 155104.

Bibliography

[1] Zhong Lin Wang. Nanopiezotronics. Advanced Materials, 19(6):889–892, 2007.

[2] Zhong Lin Wang, Rusen Yang, Jun Zhou, Yong Qin, Chen Xu, Youfan Hu, and Sheng Xu. Lateral nanowire/nanobelt based nanogenerators, piezotronics and piezo-phototronics. Materials Science and Engineering: R: Reports, 70(3-6):320–329, nov 2010.

[3] Zhong Lin Wang. From nanogenerators to piezotronics—A decade-long study of ZnO nanostructures. MRS Bulletin, 37(9):814–827, sep 2012.

[4] Chang Shi Lao, Qin Kuang, Zhong L. Wang, Myung-Chul Park, and Yulin Deng. Polymer functionalized piezoelectric-FET as humidity/chemical nanosensors. Applied Physics Letters, 90(26):262107, jun 2007.

[5] Jun Zhou, Yudong Gu, Peng Fei, Wenjie Mai, Yifan Gao, Rusen Yang, Gang Bao, and Zhong Lin Wang. Flexible Piezotronic Strain Sensor. Nano Letters, 8(9):3035–3040, sep 2008.

[6] Jyh Ming Wu, Cheng-Ying Chen, Yan Zhang, Kuan-Hsueh Chen, Ya Yang, Youfan Hu, Jr-Hau He, and Zhong Lin Wang. Ultrahigh Sensitive Piezotronic Strain Sensors Based on a ZnSnO 3 Nanowire/Microwire. ACS Nano, 6(5):4369–4374, may 2012.

[7] Ying Liu, Yan Zhang, Qing Yang, Simiao Niu, and Zhong Lin Wang. Fundamental theories of piezotronics and piezo-phototronics. Nano Energy, 14:257–275, may 2015.

[8] Ang Wei, Liuhua Pan, and Wei Huang. Recent progress in the ZnO nanostructure-based sensors. Materials Science and Engineering: B, 176(18):1409–1421, nov 2011.

[9] C W Bunn. The lattice-dimensions of zinc oxide. Proceedings of the Physical Society, 47(5):835–842, sep 1935.

[10] T. C. Damen, S. P. S. Porto, and B. Tell. Raman Effect in Zinc Oxide. Physical Review, 142(2):570–574, feb 1966.

[11] Masaru Ohnishi, Michio Yoshizawa, and Sumiaki Ibuki. A New Method for the Preparation of ZnO Flms. Japanese Journal of Applied Physics, 9(8):1017C–1017C, aug 1970.

[12] Leonard J. Brillson and Yicheng Lu. ZnO Schottky barriers and Ohmic contacts. Journal of Applied Physics, 109(12), 2011.

[13] C.A. Mead. Metal-semiconductor surface barriers. Solid-State Electronics, 9(11-12):1023–1033, nov 1966.

[14] Zhong Lin Wang. Piezoelectric Nanogenerators Based on Zinc Oxide Nanowire Arrays. Science, 312(5771):242–246, apr 2006.

[15] Xudong Wang, Jun Zhou, Jinhui Song, Jin Liu, Ningsheng Xu, and Zhong L Wang. Piezoelectric Field Effect Transistor and Nanoforce Sensor Based on a Single ZnO Nanowire. Nano Letters, 6(12):2768–2772, dec 2006.

[16] J. Wong and F. P. Bundy. Pressure effects on metal oxide varistors. Applied Physics Letters, 29(1):49–50, 1976.

[17] P. R. Emtage. The physics of zinc oxide varistors. Journal of Applied Physics, 48(10):4372–4384, 1977.

[18] Till Frömling, Roumeng Yu, Mona Mintken, Rainer Adelung, and Jürgen Rödel. Piezotronic sensors. MRS Bulletin, 43(12):941–945, dec 2018.

[19] Raschid Baraki, Nikola Novak, Till Frömling, T. Granzow, and Jürgen Rödel. Bulk ZnO as piezotronic pressure sensor. Applied Physics Letters, 105(11):111604, sep 2014.

[20] Raschid Baraki, Nikola Novak, Michael Hofstätter, Peter Supancic, Jürgen Rödel, and Till Frömling. Varistor piezotronics: Mechanically tuned conductivity in varistors. Journal of Applied Physics, 118(8):085703, aug 2015.

[21] Peter Keil, Maximilian Gehringer, Till Frömling, Nikola Novak, and Jürgen Rödel. ZnO-based single crystal-polycrystal structures for piezotronic applications. 2018.

[22] R. Baraki, N. Novak, T. Frömling, T. Granzow, and J. Rödel. Bulk ZnO as piezotronic pressure sensor. Applied Physics Letters, 105(11):10–14, 2014.

[23] Nadine Raidl, Peter Supancic, Robert Danzer, and Michael Hofstätter. Piezotronically Modified Double Schottky Barriers in ZnO Varistors. Advanced Materials, 27(12):2031–2035, mar 2015.

[24] Peter Keil, Raschid Baraki, Nikola Novak, Jürgen Rödel, and Till Frömling. Gauge factors for piezotronic stress sensor in polycrystalline ZnO. Journal of Physics D: Applied Physics, 50(17):175106, may 2017.

[25] Peter Keil, Maximilian Trapp, Nikola Novak, Till Frömling, Hans-Joachim Joachim Kleebe, and Jürgen Rödel. Piezotronic Tuning of Potential Barriers in ZnO Bicrystals. Advanced Materials, 30(10):1–5, mar 2018.

[26] Yunxia Li, Zeming Zhang, Weihua Han, Changjun Jiang, and Erqing Xie. Analysis on the piezotronic effect in a strained piezo-Schottky junction with AC impedance spectroscopy. Nano Energy, 36:118–125, jun 2017.

[27] Zheng Zhang, Qingliang Liao, Xiaohui Zhang, Guangjie Zhang, Peifeng Li, Shengnan Lu, Shuo Liu, and Yue Zhang. Highly efficient piezotronic strain sensors with symmetrical Schottky contacts on the monopolar surface of ZnO nanobelts. Nanoscale, 7(5):1796–1801, 2015.

[28] Youfan Hu, Benjamin D B Klein, Yuanjie Su, Simiao Niu, Ying Liu, and Zhong Lin Wang. Temperature Dependence of the Piezotronic Effect in ZnO Nanowires. Nano Letters, 13(11):5026–5032, nov 2013.

[29] Kory Jenkins, Vu Nguyen, Ren Zhu, and Rusen Yang. Piezotronic Effect: An Emerging Mechanism for Sensing Applications. Sensors, 15(9):22914–22940, sep 2015.

[30] F Greuter and G Blatter. Electrical properties of grain boundaries in polycrystalline compound semiconductors. Semiconductor Science and Technology, 5(2):111–137, feb 1990.

[31] Harry L Tuller. ZnO Grain Boundaries: Electrical Activity and Diffusion. Journal of Electroceramics, 4(1suppl):33–40, 1999.

[32] T K Gupta and W G Carlson. A grain-boundary defect model for instability/stability of a ZnO varistor. JOURNAL OF MATERIALS SCIENCE, 20:3487–3500, 1985.

[33] Lionel M. Levinson and H. R. Philipp. The physics of metal oxide varistors. Journal of Applied Physics, 46(3):1332–1341, mar 1975.

[34] G Blatter and F Greuter. Carrier transport through grain boundaries in semiconductors. Physical Review B, 33(6):3952–3966, mar 1986.

[35] G. Blatter and F. Greuter. Electrical breakdown at semiconductor grain boundaries. Physical Review B, 34(12):8555–8572, dec 1986.

[36] G. E. Pike. Electronic Properties of ZnO Varistors: A New Model. MRS Proceedings, 5:369, feb 1981.

[37] P. M. Verghese and D. R. Clarke. Piezoelectric contributions to the electrical behavior of ZnO varistors. Journal of Applied Physics, 87(9):4430–4438, may 2000.

[38] Anderson Janotti, Chris Van, De, and Chris G Van de Walle. Fundamentals of zinc oxide as a semiconductor. Reports on Progress in Physics, 72(12):126501, dec 2009.

[39] Lionel Vayssieres. Growth of Arrayed Nanorods and Nanowires of ZnO from Aqueous Solutions. Advanced Materials, 15(5):464–466, mar 2003.

[40] Y. C. Kong, D. P. Yu, B. Zhang, W. Fang, and S. Q. Feng. Ultraviolet-emitting ZnO nanowires synthesized by a physical vapor deposition approach. Applied Physics Letters, 78(4):407–409, jan 2001.

[41] Y.R Ryu, S. Zhu, D.C Look, J.M Wrobel, H.M Jeong, and H.W White. Synthesis of p-type ZnO films. Journal of Crystal Growth, 216(1-4):330–334, jun 2000.

[42] Y.R. Ryu, W.J. Kim, and H.W. White. Fabrication of homostructural ZnO p–n junctions. Journal of Crystal Growth, 219(4):419–422, nov 2000.

[43] T. Ive, T. Ben-Yaacov, A. Murai, H. Asamizu, C. G. Van de Walle, U. Mishra, S. P. Den-Baars, and J. S. Speck. Metalorganic chemical vapor deposition of ZnO(0001) thin films on GaN(0001) templates and ZnO(0001) substrates. physica status solidi (c), 5(9):3091–3094, jul 2008.

[44] S. Heinze, A. Krtschil, J. Bläsing, T. Hempel, P. Veit, A. Dadgar, J. Christen, and A. Krost. Homoepitaxial growth of ZnO by metalorganic vapor phase epitaxy in two-dimensional growth mode. Journal of Crystal Growth, 308(1):170–175, oct 2007.

[45] T. Ive, T. Ben-Yaacov, C.G. Van de Walle, U.K. Mishra, S.P. DenBaars, and J.S. Speck. Step-flow growth of ZnO(0001) on GaN(0001) by metalorganic chemical vapor epitaxy. Journal of Crystal Growth, 310(15):3407–3412, jul 2008.

[46] Toru Aoki, Yoshinori Hatanaka, and David C. Look. ZnO diode fabricated by excimer-laser doping. Applied Physics Letters, 76(22):3257–3258, may 2000.

[47] Ü Özgür, Ya I. Alivov, C. Liu, A. Teke, M. A. Reshchikov, S. Doğan, V. Avrutin, S.-J. Cho, and H. Morkoç. A comprehensive review of ZnO materials and devices. Journal of Applied Physics, 98(4):041301, aug 2005.

[48] J. G. Lu, Z. Z. Ye, Y. Z. Zhang, Q. L. Liang, Sz. Fujita, and Z. L. Wang. Self-assembled ZnO quantum dots with tunable optical properties. Applied Physics Letters, 89(2):023122, jul 2006.

[49] Fredrik Boxberg, Niels Søndergaard, and H. Q. Xu. Elastic and Piezoelectric Properties of Zincblende and Wurtzite Crystalline Nanowire Heterostructures. Advanced Materials, 24(34):4692–4706, sep 2012.

[50] G. Heiland and H. Ibach. Pyroelectricity of zinc oxide. Solid State Communications, 4(7):353–356, jul 1966.

[51] Kenji Ueda, Hitoshi Tabata, and Tomoji Kawai. Magnetic and electric properties of transition-metal-doped ZnO films. Applied Physics Letters, 79(7):988–990, aug 2001.

[52] C. H. Park, S. B. Zhang, and Su Huai Wei. Origin of p-type doping difficulty in ZnO: The impurity perspective. Physical Review B - Condensed Matter and Materials Physics, 66(7):1–3, 2002.

[53] Michał A Borysiewicz. ZnO as a Functional Material , a Review. 2019.

[54] Chin Boon Ong, Law Yong Ng, and Abdul Wahab Mohammad. A review of ZnO nanoparticles as solar photocatalysts: Synthesis, mechanisms and applications. Renewable and Sustainable Energy Reviews, 81(August 2017):536–551, 2018.

[55] David R Clarke. Varistor Ceramics. Journal of the American Ceramic Society, 82:485–502, 1999.

[56] Lionel M. Levinson and Herbert R. Philipp. Zinc Oxide Varistors - a Review. American Ceramic Society Bulletin, 65(4):639–646, 1986.

[57] Lionel M. Levinson and Herbert R. Philipp. ZnO Varistors for Transient Protection. IEEE Transactions on Parts, Hybrids, and Packaging, 13(4):338–343, 1977.

[58] Qi Wang, Zhijian Peng, Changchun Lv, and Xiuli Fu. High-performance varistors prepared by hot-dipping tin oxide thin films in Sb 2 O 3 powder: Influence of temperature. Journal of the American Ceramic Society, 101(1):61–70, jan 2018.

[59] Shuaijun Yang and Dachuan Zhu. Effect of co-doping Y2O3–La2O3 on microstructure and electrical properties of ZnO-based varistor ceramics prepared from nanosize ZnO powder. Journal of Materials Science: Materials in Electronics, 29(4):3104–3109, feb 2018.

[60] Jeen Maria Mathews, Balanand Santhosh, Peer Mohamed Abdul Azeez, and Ananthakumar Solaiappan. Design and fabrication of flexible poly(vinyl chloride) dielectric composite

reinforced with ZnO microvaristors. Journal of Applied Polymer Science, 135(12):46031, mar 2018.

[61] Y.Q. Fu, J.K. Luo, X.Y. Du, A.J. Flewitt, Y. Li, G.H. Markx, A.J. Walton, and W.I. Milne. Recent developments on ZnO films for acoustic wave based bio-sensing and microfluidic applications: a review. Sensors and Actuators B: Chemical, 143(2):606–619, jan 2010.

[62] Jr H. Jr H. He, Cheng L. Hsin, Jin Liu, Lih J. Chen, and Zhong L. Wang. Piezoelectric gated diode of a single ZnO nanowire. Advanced Materials, 19(6):781–784, mar 2007.

[63] Guang Zhu, Rusen Yang, Sihong Wang, and Zhong Lin Wang. Flexible High-Output Nanogenerator Based on Lateral ZnO Nanowire Array. Nano Letters, 10(8):3151–3155, aug 2010.

[64] X. Wang, J. Song, J. Liu, and Z. L. Wang. Direct-Current Nanogenerator Driven by Ultrasonic Waves. Science, 316(5821):102–105, apr 2007.

[65] Qing Yang, Wenhui Wang, Sheng Xu, and Zhong Lin Wang. Enhancing Light Emission of ZnO Microwire-Based Diodes by Piezo-Phototronic Effect. Nano Letters, 11(9):4012–4017, sep 2011.

[66] Qing Yang, Xin Guo, Wenhui Wang, Yan Zhang, Sheng Xu, Der Hsien Lien, and Zhong Lin Wang. Enhancing Sensitivity of a Single ZnO Micro-/Nanowire Photodetector by Piezo-phototronic Effect. ACS Nano, 4(10):6285–6291, oct 2010.

[67] D. C. Look, D. C. Reynolds, J. W. Hemsky, R. L. Jones, and J. R. Sizelove. Production and annealing of electron irradiation damage in ZnO. Applied Physics Letters, 75(6):811–813, aug 1999.

[68] Charles Kittel. Introduction to Solid State Physics, 8th edition, 2004.

[69] J. M. Ziman. Principles of the Theory of Solids. Cambridge University Press, jul 1972.

[70] S.M. M Sze and Kwok K. Ng. Physics of Semiconductor Devices. John Wiley & Sons, Inc., Hoboken, NJ, USA, oct 2006.

[71] Chih-tang Sah, Robert Noyce, and William Shockley. Carrier Generation and Recombination in P-N Junctions and P-N Junction Characteristics. Proceedings of the IRE, 45(9):1228–1243, sep 1957.

[72] R. N. Hall. Electron-Hole Recombination in Germanium. Physical Review, 87(2):387–387, jul 1952.

[73] W. Shockley and W. T. Read. Statistics of the Recombinations of Holes and Electrons. Physical Review, 87(5):835–842, sep 1952.

[74] William Shockley and E. M. Field. Electrons and Holes in Semiconductors. Physics Today, 5(12):18–19, dec 1952.

[75] Fritz Scholz. Interfaces in crystalline materials (1996) A. P. Sutton, R. W. Balluffi. Journal of Solid State Electrochemistry, 1(1):117–118, jul 1997.

[76] G. H. Bishop and B. Chalmers. Dislocation structure and contrast in high angle grain boundaries. Philosophical Magazine, 24(189):515–526, sep 1971.

[77] Siqian Li, Jun Chen, and Pierre Ruterana. The [10-10] edge dislocation in the wurtzite structure: A high-resolution transmission electron microscopy investigation of [0001] tilt grain boundaries in GaN and ZnO. Acta Materialia, 175:457–465, 2019.

[78] Johan M. Carlsson, Helder S. Domingos, Paul D. Bristowe, and Bo Hellsing. An interfacial complex in zno and its influence on charge transport. Physical Review Letters, 91(16):2–5, 2003.

[79] Yukio Sato, James P. Buban, Teruyasu Mizoguchi, Naoya Shibata, Masatada Yodogawa, Takahisa Yamamoto, and Yuichi Ikuhara. Role of Pr segregation in acceptor-state formation at ZnO grain boundaries. Physical Review Letters, 97(10):1–4, 2006.

[80] Eric W. Weisstein. Heaviside Step Function.

[81] P. M. Verghese and D. R. Clarke. Piezoelectric contributions to the electrical behavior of ZnO varistors. Journal of Applied Physics, 87(9):4430–4438, 2000.

[82] K. A. Taylor, E. Gjonaj, Z. Zhou, and B. Xu. Mesoscopic modeling of the mechanically tunable electrical conductivity of ZnO varistors. Journal of Applied Physics, 127(15):155104, apr 2020.

[83] Masahiko Kusaka Okazaki, Masaaki Kanakura, Susumu, Masaaki Kanakura, and Susumu. Interface Properties and Schottky Barrier on the Polar Surfaces of CdS and GaP Crystals. Japanese Journal of Applied Physics, 13:437, 1974.

[84] J. Lagowski and H. C. Gatos. Photomechanical Effect in Noncentrosymmetric Semiconductors-CdS. Applied Physics Letters, 20(1):14–16, jan 1972.

[85] Yonatan Calahorra and Sohini Kar-Narayan. Piezoelectricity in non-nitride III–V nanowires: Challenges and opportunities. Journal of Materials Research, 33(06):611–624, mar 2018.

[86] Hadis Morko and Mit Zgr. Zinc Oxide. Wiley-VCH Verlag GmbH & Co. KGaA, Weinheim, Germany, jan 2009.

[87] W Rieger, T Metzger, H Angerer, R Dimitrov, O Ambacher, and M Stutzmann. Influence of substrate-induced biaxial compressive stress on the optical properties of thin GaN films. Applied Physics Letters, 68(7):970–972, feb 1996.

[88] L Shen, S Heikman, B Moran, R Coffie, N.-Q. Zhang, D Buttari, I.P. P Smorchkova, S Keller, S.P. P DenBaars, and U.K. K Mishra. AlGaN/AlN/GaN high-power microwave HEMT. IEEE Electron Device Letters, 22(10):457–459, oct 2001.

[89] Raegan Lynn Johnson. Characterization of piesoelectric ZnO thin films and the fabrication of piezoelectric micro-cantilevers. Technical report, Ames Laboratory (AMES), Ames, IA (United States), jan 2005.

[90] Faruque M. Hossain, J. Nishii, S. Takagi, A. Ohtomo, T. Fukumura, H. Fujioka, H. Ohno, H. Koinuma, and M. Kawasaki. Modeling and simulation of polycrystalline ZnO thin-film transistors. Journal of Applied Physics, 94(12):7768, 2003.

[91] R.L. Taylor. FEAP - Finite Element Analysis Program, 2014.

[92] Derek R. Gaston, Cody J. Permann, John W. Peterson, Andrew E. Slaughter, David Andrš, Yaqi Wang, Michael P. Short, Danielle M. Perez, Michael R. Tonks, Javier Ortensi, Ling Zou, and Richard C. Martineau. Physics-based multiscale coupling for full core nuclear reactor simulation. Annals of Nuclear Energy, 84:45–54, oct 2015.

[93] Yan Zhang, Ying Liu, and Zhong Lin Wang. Fundamental Theory of Piezotronics. Advanced Materials, 23(27):3004–3013, jul 2011.

[94] Rodolfo Araneo, Fabiano Bini, Marialilia Pea, Andrea Notargiacomo, Antonio Rinaldi, Giampiero Lovat, and Salvatore Celozzi. Current–Voltage Characteristics of ZnO Nanowires Under Uniaxial Loading. IEEE Transactions on Nanotechnology, 13(4):724–735, jul 2014.

[95] Susan Athey. The Impact of Machine Learning on Economics. In The Economics of Artificial Intelligence, pages 507–552. University of Chicago Press, 2019.

[96] J.B. Heaton and Nick Polson. Deep Learning for Finance: Deep Portfolios. SSRN Electronic Journal, 2016.

[97] Mariofanna Milanova. Visual attention in deep learning: a review. International Robotics & Automation Journal, 4(3), may 2018.

[98] Seyed Majid Azimi, Dominik Britz, Michael Engstler, Mario Fritz, and Frank Mücklich. Advanced Steel Microstructural Classification by Deep Learning Methods. Scientific Reports, 8(1):2128, dec 2018.

[99] K. T. Schütt, H. E. Sauceda, P.-J. Kindermans, A. Tkatchenko, and K.-R. Müller. SchNet – A deep learning architecture for molecules and materials. The Journal of Chemical Physics, 148(24):241722, jun 2018.

[100] Raymond J. Mooney. Machine Learning, volume 1. Oxford University Press, sep 2012.

[101] Zhiqiang Zhang, Dalong Geng, and Xudong Wang. Calculation of the piezoelectric and flexoelectric effects in nanowires using a decoupled finite element analysis method. Journal of Applied Physics, 119(15):0–9, 2016.

List of Figures

List of Tables